NOVEL SELF-ASSEMBLY OF CRYSTALLINE $MgAl_2O_4$ NANOSTRUCTURES

Novel Self-assembly of Crystalline $MgAl_2O_4$ Nanostructures Promoted by Annealing a Gold Overlayer on a (111) $MgAl_2O_4$ Substrate

By

Tahereh Majdi, B.Eng.

A Thesis

Submitted to the School of Graduate Studies

in Partial Fulfilment of the Requirements for the Degree

Master of Applied Science

McMaster University

Master of Applied Science (2013) McMaster University

(Department of Engineering Physics) Hamilton, Ontario

TITLE: Novel Self-assembly of Crystalline $MgAl_2O_4$ Nanostructures Promoted by Annealing a Gold Overlayer on a (111) $MgAl_2O_4$ Substrate

AUTHOR: Tahereh Majdi, B.Eng. (McMaster University)

SUPERVISOR: Dr. John S. Preston

Abstract

The solid state dewetting characteristics of thin gold films sputtered onto (111) $MgAl_2O_4$ substrates were investigated. Prior research done on this system reported discovering the self-assembly of intricately shaped nanostructures, consisting of a faceted sphere lying above a truncated triangular pyramid, formed by applying a specific two stage heating profile [1]. The current work was done to provide deeper insight on the odd self-assembly observed in this system. The results indicate that the intricate structures are not purely gold self-assemblies, but in fact consist of three distinct materials: a single crystal or polycrystalline gold faceted sphere, separated by an interfacial boundary layer, from above a crystalline $MgAl_2O_4$ necking structure that spontaneously developed from the initially flat substrate. The boundary separating these two assemblies is confined within a thin, sharp region of a third material consisting of Au and O elements. The composition and crystalline nature of the individual nanostructures were studied using high angle annular dark-field imaging, energy dispersive X-ray spectroscopy, and electron energy loss spectroscopy employed by a high resolution transmission electron microscope. Two-dimensional X-ray diffraction texture analysis revealed that the gold nanoparticles are crystalline, with majority of the maximum intensity signal corresponding to the epitaxial alignment of the gold nanoparticles with the substrate. The $MgAl_2O_4$ necking structures were found to be sensitive to both the annealing profile, and the thickness of the gold film, which influenced the distinguishable presence, size, and footprint of the $MgAl_2O_4$ nanostructures. Atomic force microscopy and scanning electron microscopy results were consistent with the gold overlayer playing an essential role in the self-assembly of $MgAl_2O_4$ nanostructures. While the fundamental mechanisms that govern this phenomenon are not entirely clear, the presented results do provide insight into the role of interfaces in heteroepitaxial systems, especially the self-assembly of crystalline nanostructures from a previously stable substrate.

Acknowledgements

I would like to acknowledge and thank all those who made this work possible:

The National Science and Engineering Research Council of Canada Collaborative Research and Training Experience Program in Photovoltaics (CREATE PV) for funding and support of this project.

My supervisor, Dr. John Stuart Preston, for accepting me as a graduate student in his group. It has been a true pleasure working under his supervision. Despite his incredibly busy schedule, he provided constant feedback and encouragement, all while maintaining a positive attitude. I have learned much from my Master's degree and will be forever grateful for the opportunity.

Dr. Peter Mascher, for his participation as a co-supervisor, and for his kind and useful support and feedback.

Dr. Guozhen Zhu, a postdoctoral scholar working jointly between our group and Dr. Gianluigi Botton, for TEM measurements and analysis. Her motivation and drive has shined much light on this project. Without her, this work would have taken an entirely different direction.

Dr. Kristoffer Meinander and Dr. Jessica Carvalho, postdoctoral scholars of our group, for useful and long discussions associated with my project. Special thanks to Dr. Jessica Carvalho in addition for assisting in AFM measurements and training as well as for helping with the development of transferring the gold nanoparticles to an epoxy carrier. Mr. Gabriel Devenyi, a Ph.D. candidate of our group, for thin film deposition and helpful feedback on various topics throughout my degree.

Dr. James F. Britten and Ms. Victoria Jarvis of the McMaster Analytical X-Ray Diffraction Facility (MAX), for assisting in instrument and software training, data collection, and engaging in many useful conversations. It has been a very pleasant experience working with them, and I have learned much from it.

Mr. Stephen J. Smith, Mr. Quentin Simms, and Ms. Judy Chen, summer students of our group, for their hard work on collecting size and density measurements from my SEM images.

Mr. Jim Garrett, of the Brockhouse Institute for Materials Research (BIMR), for assisting me with the furnace design and setup. He patiently trained me on various equipment and provided much appreciated feedback.

The staff of the Canadian Center for Electron Microscopy (CCEM): Mr. Chris Butcher, Mr. Steve Koprich, and Dr. Glynis de Silveira, for instrument training. Furthermore, Mr. Chris Butcher, engaged in many discussions regarding date analysis, which I truly appreciate. Mr. Travis Casagrande, for SEM imaging using the Magellan, and engaging in useful discussion. His patience and detail oriented attitude was very helpful. Mr. Andy Duft, and Mr. Wenhe, for patiently assisting in thin film deposition. Their help is truly appreciated. Ms. Juila Huang, also of the CCEM, for TEM sample preparation. Her hard work and attention to detail was of great value to this work.

Mrs. Doris V. Stevanovic, and Dr. Zhilin Peng, of the Centre for Emerging Device Technology (CEDT), and Joshua Rideout, a Ph.D. candidate of our group, for training on the sputtering system and e-beam metallization system.

Ms. S. Rida Zainab, an M.A.Sc. student of our group, for kindly accepting to edit this document.

My wonderful family; my parents, Dr. Abbas Majdi and Mrs. Mahin Majdi. Their kind support, encouraging words, positive attitude, and infinite patience, has made this all possible. After years of distance, they spent the last few months living with me, providing me with a warm house and wonderful meals, leaving me to work on my thesis without a care in the world. My sister, Fatima, my brother, Edris, my brother-in-law, Mansour, and my amazing niece Mila, for their immense support and consistent encouragement.

My better half, Stephen Jovanovic, not only for editing, and contributing towards modifying the denoted images in my thesis, but more importantly, for patiently supporting me, and never giving up on me. His persistent encouragement and understanding personality has made this all possible.

Tahereh Majdi

Listing of Contents

List of Figures

List of Tables

List of Acronyms

2D	two dimensional
ABF	annular bright field
AFM	atomic force microscopy
BSE	backscattered electrons
CVD	chemical vapor deposition
EBSD	electron backscattered diffraction
EDS	energy dispersive spectroscopy
HAADF	high angle annular dark field
HPLC	high purity liquid chromatography
LAADF	low angle annular dark field
NC	non-contact
PVD	physical vapor deposition
SE	secondary electrons
SEM	scanning electron microscopy
STEM	scanning transmission electron microscopy
TEM	transmission electron microscopy
VLS	vapor-liquid-solid
XEDS	X-ray energy dispersive spectroscopy
XRD	X-ray diffraction

List of Symbols

Symbol	Description
c	speed of light in a vacuum
d	lattice spacing
D_s	surface self-diffusivity
E_0	some energy value
g	standard gravitational acceleration
h	film thickness
h_0	initial film thickness
h_{eq}	equilibrium thickness
J	Joule
k	Boltzmann constant
m	relativistic mass
m_0	non-relativistic mass or rest mass
n	an integer, order of reflection
P_c	equilibrium vapor pressure of a curved particle
P	equilibrium vapor pressure of a flat surface
R	radius of a curved particle
T	temperature
v	velocity
V_r	radial velocity
X, Y, Z	translational axis defined in X-ray
Z	atomic number
α	convergence angle
β	inner collection angle of the annular detector employed in the TEM
γ	surface tension

γ_{lv}	liquid-vapor surface/interfacial tension
γ_{sl}	substrate-liquid surface/interfacial tension
γ_{sv}	substrate-vapor surface/interfacial tension
ΔE	change in energy
$\Delta\mu$	change in chemical potential between a curved and flat surface
θ	The scattering angle in the context of X-ray diffraction or the contact angle in the context of dewetting.
λ	Wavelength
λ_{cap}	capillary length
λ_s	spinodal wavelength
ρ	density
τ	incubation time for dewetting
Φ	effective interface potential
Ω	atomic volume
ω, ψ, φ	Eulerian angles described in X-ray

Chapter 1 - Introduction

1.1 Overview

Gold clusters have fascinated people for centuries, providing red ruby color to windows, vases, pottery, and other ornaments [2]. The first known written account of gold ruby glass is from medieval ages, by Al Razi (865-925), a Persian scholar, philosopher, and alchemist, in his treatise *Secrets of Secrets* [3]. For centuries after that, the application of gold clusters remained limited to coloring glasses, evolving from ruby, to purple, rose, and pink. Up to the 18th century (al)chemists were obsessed with manufacturing metals for mystical reasons; they believed that the color of a metal inhibited its 'soul' and essence, so if the color was extracted it would possess the spirit of the metal and could perform alchemical transmutation.

In the past few decades, the study of gold particles on the nanoscale has taken a rather different path, leading to important discoveries; providing nucleation sites for the growth of nanowires [4], or carbon nanotubes [5], and in promoting charge transfer in various gases. In 1964 R. S. Wagner, proposed the vapor-liquid-solid (VLS) theory for the growth of nanowires that necessitates the presence of gold, nickel, or platinum nanostructured "impurities" to promote the growth of nanowires [6], [7]. Gold nanoparticles were found to have superior catalytic properties in the 1970's with reports from Bond et al. on hydrogenation over Au supported on SiO_2 nanoparticles, and other reports by Parravano et al. on oxygen and hydrogen transfer reactions using Au/MgO and Au/Al_2O_3 catalysts [8]. Other important applications discovered for gold nanoparticles are related to the enhanced surface plasmon resonance created by gold nanoparticles for biosensing applications.

The unique optical properties of gold particles on the micro and nano scale, their size dependent electrochemistry, and high chemical stability have made them the model system of choice for exploring a wide range of phenomena including self-assembly, biolabeling, catalysis, electron-transfer theories, phase transfer, DNA melting and assays, and crystal growth. It is this vast breadth of impact of gold nanoparticles that has made it a very active field in basic nanoscience research and application in recent decades [9].

Tailoring the self-assembly/nucleation and growth mechanisms of nanoparticles is important as it provides a means to design and fabricate more efficient functional devices. To date, many chemical and physical routes have been employed, including, sol-gel and impregnation, wet chemical methods, layer-by-layer self-assembly, ion beam-assisted techniques, ion implantation, combined thermal and physical vapor deposition (PVD) techniques, chemical vapor deposition (CVD), evaporation, and sputtering techniques [2]. Gold clusters can be synthesised as stand-alone structures or in combination with other elements. Among many support structures for gold nanoparticles, metal-oxides have received much attention due to their structural differences and chemical-physical characteristics. In particular, oxides such as SiO_2, TiO_2, and Al_2O_3 have been significantly studied owing to features such as optical transparency in the visible range, insulating nature, structural and thermal stability, and weak interaction with the host [2].

The work presented in this thesis is focused on the characteristics of gold nanoparticles that self-assemble on $MgAl_2O_4$ substrates; thin films of gold were sputtered on the substrate at room temperature and annealed in an argon atmosphere to promote dewetting and self-assembly of gold nanostructures. The method of growth and choice of substrate was selected due to the remarkable and novel dewetting characteristics reported in this system by Devenyi et al. in 2009 [1]. They reported an annealing profile that promoted gold films, with specific thicknesses on $MgAl_2O_4$ substrates, to self-assemble and form intricate nanostructures, composed of a faceted sphere atop a necking structure. More details will follow later in this chapter. The reported self-assembled nanostructures are different from commonly reported dewetted structures that have a spherical or hemispherical-like shape, with or without faceting. The theoretical hypothesis provided in this report did not fully justify the systems behaviour and thus, promoted the research presented in this thesis. The current work found that the structures reported by Devenyi et al. are not entirely gold, but are in fact $MgAl_2O_4$ necking structures that have self-assembled below a gold cap. Gold has been found to play a key role in promoting mass transport on the surface of $MgAl_2O_4$, causing the surface to reconstruct and form crystalline $MgAl_2O_4$ necking structures. The reasons for this are not clear, however, processes involving minimization of surface energy, or the catalytic activity of gold may be associated to this phenomenon, and are discussed in this chapter.

Section 1.2 of this chapter provides a brief overview on the basic theory of dewetting, first in liquids and subsequently in solid films. It also covers the experimental conditions that affect dewetting. Section 1.3 covers relevant and fundamental properties, and literature related to bulk $MgAl_2O_4$, as well as bulk and nanoscale properties of gold. It includes literature, and basic concepts regarding the instability of $MgAl_2O_4$ substrates at elevated temperatures, and the catalytic behaviour of gold. Finally, section 1.4 summarizes literature that explicitly study dewetting of metal films on oxide substrates, and includes the preceding work to this thesis.

1.2 Fundamental Concepts of Dewetting

Dewetting of thin films of gold deposited on $MgAl_2O_4$ films is an essential part of all the experiments conducted, and reported on in this thesis. For this reason, it is important to understand the basic fundamental principles of dewetting which are described in this section.

1.2.1 Dewetting of Liquid Films

Wetting refers to how a liquid deposited on a solid or liquid substrate spreads. An important parameter in determining the stability of a liquid film is its capillary length [10];

$$\lambda_{cap} = \sqrt{\gamma_{lv}/\rho g} \qquad \text{Equation 1}$$

where γ_{lv} is the liquid-vapor surface tension, ρ is the density of the liquid and g is the standard gravitational acceleration constant for earth. If a film is thicker than its capillary length, gravity will stabilize the film, whereas, for films thinner than this capillary length intermolecular forces can initiate “dewetting” in effort to minimize total surface energy. The competing factors involved that dictate wetting or dewetting behaviour of a liquid film are the substrate-liquid, γ_{sl}, liquid-vapor, γ_{lv}, and substrate-vapor, γ_{sv}, interfacial tensions, shown in Figure 1. Surface or interfacial tension is defined as the energy required to increase the surface area by one unit. It has units of J/m^2, and can also be viewed as a force per unit length. Dewetting is a dynamic process; it is initiated when a film is in a non-equilibrium, unstable state. The equilibrium wetting behaviour of a droplet is described by Young’s equation, equation 2. It provides a relation between the relevant interfacial tension forces at the three phase contact point, illustrated in Figure 1, for a droplet on a solid surface under equilibrium conditions [11];

$$cos(\theta) = \frac{\gamma_{sv} - \gamma_{sl}}{\gamma_{lv}} \qquad \text{Equation 2}$$

In this relation θ is defined as the contact angle, the angle measured between the substrate-island interface and the tangent on the droplet surface at the three phase contact point. A liquid film will completely wet the substrate when $\theta = 0$; the solid-vapor interfacial energy is equal to, or greater than, the sum of the solid-liquid, and liquid-vapor interfacial energy. That is, it is more energetically favorable to have the liquid film coat the substrate surface, than for the substrate surface to be exposed to the ambient vapor. Non-wetting where, $\theta = \pi$, is the opposite; the combined interfacial energy of the substrate and liquid, with ambient, is equal to the interfacial energy between the solid and liquid. In this case, it is energetically undesirable for the liquid and solid to be in contact with one another. For $0 < \theta < \pi$, the competing interfacial forces result in partial dewetting, so that the liquid forms a spherical cap.

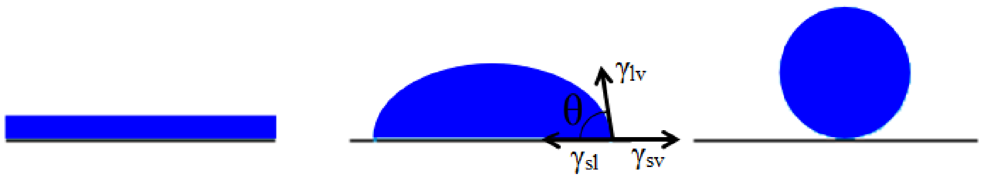

complete wetting **partial wetting** **nonwetting**

Figure 1: Schematic diagram of different dewetting behaviour by a liquid drop on a solid surface. The interfacial forces and contact angles used in Young's equation are also indicated. Complete wetting is characterized by $\theta = 0$, partial wetting by $0 < \theta < \pi$, and non-wetting by $\theta = \pi$. Modified from Jacobs et al., [11].

To understand the non-equilibrium behaviour of the film prior to achieving equilibrium, the interactions between the liquid-vapor and solid-liquid interfaces, across the liquid film, must also be considered. The effective interface potential, $\Phi(h)$, is suitable for this purpose. It comprises both short and long-range interactions. It is defined as the excess free energy per unit area that is required to bring two interfaces from infinity to a certain distance, h, with one another. In this function, h indicates the film thickness.

Figure 2 shows typical curves depicting the effective interface potential for a stable, metastable, and unstable film. Line (1) indicates a stable film; infinite energy is required to thin the film and initiate dewetting. In line (3), $\Phi''(h) < 0$ when $h > h_{eq}$, such that the film is always unstable. Reducing the film thickness, will lower the effective interface potential, and is therefore energetically favorable. Films in this regime can break up in an undulatory fashion with a characteristic wavelength, λ_s. This is known as the spinodal wavelength. The amplitude of this wavelength grows fastest, and will therefore dominate the evolving dewetting pattern. Such dewetting, which arises from unstable films, is known as spinodal dewetting. Spinodal dewetting can only take place when $\Phi''(h_0) < 0$, where h_0 is the initial thickness of the homogeneous film. Therefore, regions of Line (2) corresponding to $\Phi''(h) < 0$, are unstable. If h_0 falls within this region, then spinodal dewetting will occur. When $\Phi''(h)$ is positive, the film is considered to be metastable. It is stable to small fluctuations in thickness, but sufficiently large variations will allow the film to enter the unstable regime where $\Phi''(h) < 0$. When h_0 lies is the metastable regime, spinodal dewetting can no longer explain the dewetting behaviour; it may be understood through heterogeneous nucleation. Dewetting is promoted by surface defects, impurities, or sufficiently large perturbations in film thickness, and thus exhibits random statistics. These sites promote nucleation of holes, leaving the film in an unstable regime which stimulates the growth of holes, and hole coalescence. The ribbons that separate two coalescing holes, break up to form droplets due to Rayleigh-Plateau instability. This type of instability explains why a cylinder may distort into drops in order to lower its surface energy, as seen when sufficiently reducing the flow of water through a faucet. Finally, Ostwald ripening causes large droplets to grow at the cost of small ones. This process of dewetting is described in more detail in the following section [11], [12].

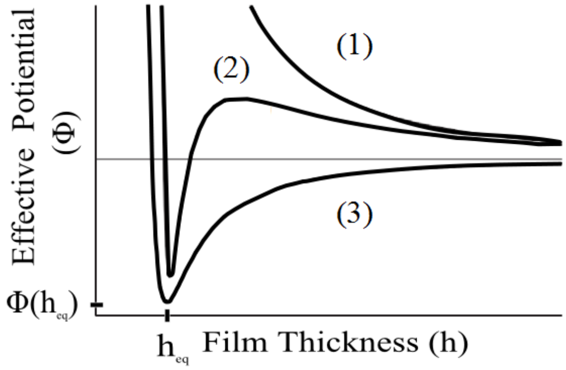

Figure 2: Effective interfacial potential as a function of film thickness. Line (1) indicates stable, (2) metastable, and (3) unstable films. Modified from Jacobs et al., [11].

1.2.2 Solid State Dewetting

Thin solid films are formed under conditions in which atomic mobility is limited, thus resulting in unstable or metastable films. That is why when heated sufficiently they dewet, otherwise called agglomerate, by solid state diffusion in an effort to minimize total surface energy. This can occur well below the film's melting temperature, while it remains in the solid state [13], [14].

The process of dewetting begins with hole formation. In polycrystalline materials grain boundaries, more specifically, triple junction grain boundaries serve as a precursor for hole growth. Where two grains coincide and meet the substrate surface, a force balance takes place, creating a groove. If the groove depth is greater than or equal to the film thickness, a hole will form and initiate dewetting. The probability of hole formation increases when the film thickness and film/vapor interfacial energy are small, and the grain boundary energy and grain radius are large. Increasing temperature enhances both surface self-diffusivity, and grain radius growth, therefore, the likelihood of hole formation. Therefore, dewetting of the film increases with increasing temperature.

Once a stable hole has formed, surface self-diffusion takes place to reduce the curvature at sharp corners and edges as illustrated in Figure 3 (a). This drives the retraction of the edges by mass transport from the interface to the upper lip, creating a rim around the hole with a height greater than its surroundings. The rim now has a higher local curvature than the flat surface surrounding it, thus, provoking diffusion toward the rim. Therefore, a valley is formed in the vicinity of the rim. Diffusion may continue until the valley contacts the substrate, creating a new hole, as well as a wire or strand from the now detached rim. This process is called pinch-off. It may continue until the entire film breaks up into strands. Figure 3 shows a schematic cross-sectional view of this process.

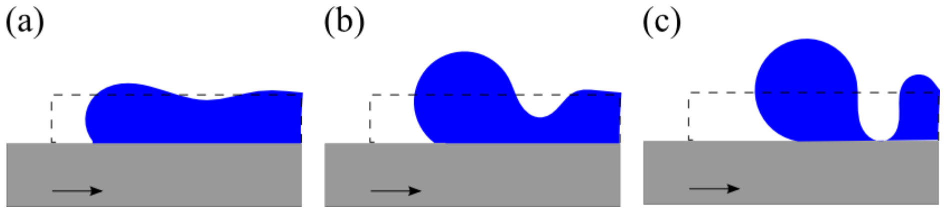

Figure 3: Schematic cross-sectional diagram of hole growth and propagation through pinch-off once a stable hole is created. The doted rectangle represents the original state of the film surrounding a newly formed hole (left side of dotted box). a) Sharp corners and edges surrounding a hole will promote surface self-diffusion and edge retraction, increasing the hole radius, and creating a rim around the hole. b) The newly formed rim will have a local higher curvature than the surrounding film, therefore, promoting surface self-diffusion to the rim. This causes a valley to form in the vicinity of the rim. c) The valley may continue to grow and ultimately contact the substrate; therefore, a new hole is created on the right side of the rim. Modified from C. V. Thompson, [13].

The strands created will have small perturbations across their length and therefore will break up into islands due to Rayleigh-Plateau-like instabilities.

The islands will not be of uniform size. Small perturbations in their curvature, will significantly affect their local vapor pressure. This effect is described by the Kelvin equation. Equation 4 corresponds to the Kelvin equation for the simplified case of a spherical particle having radius R and therefore a corresponding curvature of 2/R [7] ;

$$P_c = P_\infty \exp\left(\frac{2\gamma\Omega}{kRT}\right) \qquad \text{Equation 3}$$

where P_c is the equilibrium vapor pressure of the curved particle with radius R, P_∞ is the equilibrium vapor pressure of a flat surface, γ is the interfacial tension, Ω is the atomic volume, k is the Boltzmann constant, and T is temperature. The vapor pressure of the islands is related to chemical potential by;

$$\Delta\mu = kTln\left(\frac{P_c}{P_\infty}\right) \qquad \text{Equation 4}$$

where $\Delta\mu$ is the difference in chemical potential between the curved surface and flat surface. Thus, there exists a gradient in chemical potential between smaller and larger islands. It drives the evaporation of, or solid state diffusion from the small islands, having a larger vapor pressure and therefore a larger chemical potential, in favor of condensation and diffusion to the larger particles with a smaller chemical potential. This process is known as Ostwald ripening [7].

Liquids and amorphous solids have isotropic surface energy; therefore, their equilibrium structures are smooth. In this case reducing the surface energy is achieved by minimizing the surface area so that the equilibrium contact angle explained by Young’s equation is attained. This is not the case for solid crystalline particles; their equilibrium structures have surface facets.

In crystalline solids, the surface energy can depend strongly on the exposed orientation. As a result, when crystalline islands are formed, they can further reduce their surface energy by faceting. Faceting inevitably involves creating additional surface area, however, by reducing the exposure of facets with high surface energy, the total energy can be minimized. The surface energy of a facet depends on both the number and strength of bonds that are broken to create that surface. Bond strength is related to the coordination number; bonding to an atom with fewer neighbors is stronger than to an atom with many neighbors. Thus, surface energies exhibit similar trends to cohesive energies; they are lower for more closely packed surfaces, and greater for more open ones [15].

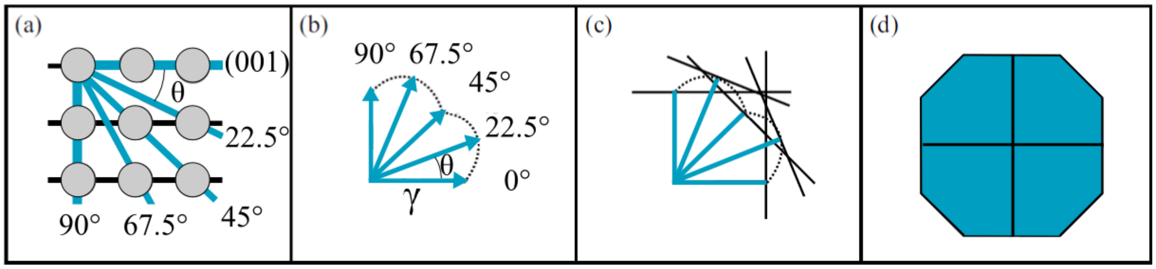

Figure 4: (a) Schematic diagram of a 2D cubic close packing crystal with various cleavage planes labeled by their corresponding angles, θ, with the (001) plane. (b) Polar surface tension plot corresponding to the cleavage planes illustrated in (a). Each vector has a magnitude proportional to the surface tension of the cleavage plane at that particular angle. (c) Sketching Wulff planes; planes at the end point, and perpendicular to, every surface tension vector. (d) Crystal equilibrium shape determined by Wulff theorem. It is constructed by considering only the inner envelope of the Wulff planes shown in (c). The image includes the equilibrium shape for all four equivalent quadrants. Modified and reprinted with permission from [15].

Knowledge of surface tension or energy can aid in determining a crystal's equilibrium shape. Consider the schematic cubic close-packed crystal shown in Figure 4. A surface can be created by making cuts along various planes similar to those shown in Figure 4 (a). They are labeled by the angle θ they make with the (001) plane. A polar surface energy plot can be configured by drawing radial vectors from the origin, with a magnitude proportional to the surface tension, for each value of θ. This is shown in Figure 4 (b). Now by applying the Wulff theorem, the equilibrium crystal structure can be determined; planes are constructed at the end of, and perpendicular to, every radial surface tension vector, as shown in Figure 4 (c). These planes are known as Wulff planes. The inner envelope of the Wulff planes yield the equilibrium crystal structure and is shown in Figure 4 (d) [15].

From this, one can infer that the distance of each facet to the center of the crystal is proportional to the surface energy of that facet. Applying the Wulff theorem in reverse, one can extract the relative surface energies of the different facets, given a particular crystal shape. It is important to note that the accuracy of the Wulff theorem becomes questionable as the volume of the crystal decreases to the nanometer scale, since the energetic contribution of edges and corners at the boundary become considerable [15]. Therefore, the cost of creating a new edge may be comparable to the energy saved by creating a new surface described by the Wulff construction.

1.2.2.1 Effect of Film Thickness on Dewetting Temperature

Assuming that all variables such as annealing rate and duration are kept constant then the temperature at which dewetting is first observed will depend on film thickness and will vary depending on the material that has undergone annealing. Figure 5 shows the temperature at which dewetting has led to island formation, such that the initial film is no longer continuous and electrically conductive, in other words, it has exceeded its percolation threshold [16].

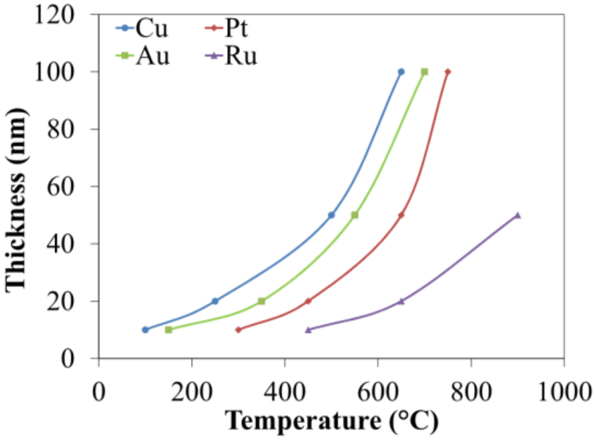

Figure 5: Effect of film thickness on the temperature at which dewetting leads to island formation, exceeding the percolation threshold. The metal films were deposited on SiO_2/Si substrates. Modified from P. R. Gadkar et al., [16].

1.2.2.2 Effect of Film Thickness on Particle Size

The average size of dewetted gold particles increases with increasing the initial film thickness. This trend holds regardless of the sample preparation and annealing method. Figure 6 (a) depicts such a trend for gold nanoparticles dewetted via electron beam induction [17], while the gold nanoparticles in Figure 6 (b) were prepared by nanosphere lithography [18]. This is a technique used to pattern thin films. Initially, a monolayer of closely packed monodisperse polymer spheres is deposited onto the substrate, and then a thin metal film is deposited over it. The spheres are then dissolved, leaving behind an array of metal nanoparticles on the substrate which are subsequently annealed. In both cases, a greater starting thickness of gold corresponds to larger particle sizes.

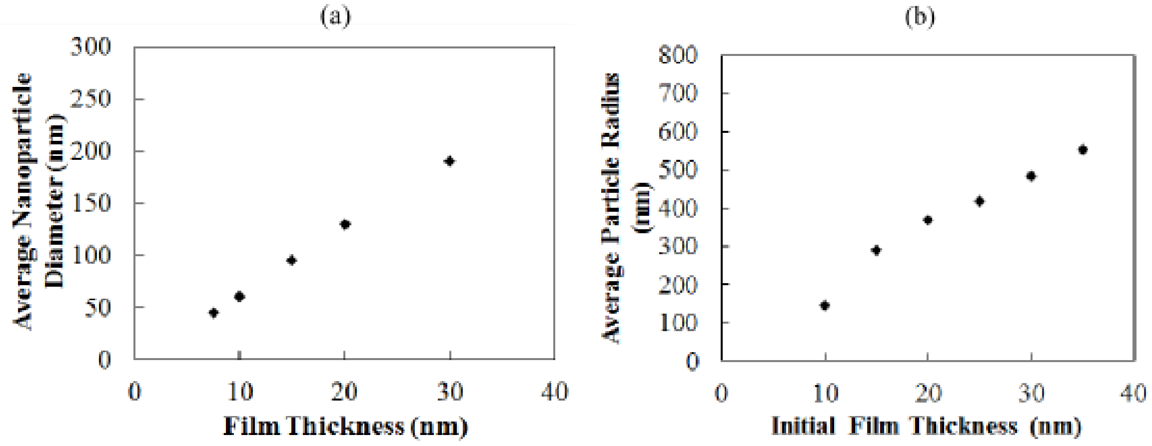

Figure 6: Dewetted gold nanoparticle size as a function of initial film thickness. (a) Gold films deposited on SiO_2/Si substrates, and annealed by electron beam induction. Modified from Kojima et al., [17]. (b) Gold films deposited on Si_3N_4/SiO_2/Si substrates, and prepared by nanosphere lithography. Modified from Müller et al., [18]. The same trend holds regardless of preparation method; as the initial film thickness increases, the average nanoparticles size becomes larger.

1.2.2.3 Influence of Annealing Pressure and Profile on Particle Size

A study done by G. Meng et. al. on Au nanoparticles [19], dewetted on single crystal MgO, $SrTiO_3$, and Al_2O_3 substrates, indicated that the size of Au nanoparticles are influenced by the annealing temperature and duration. More so, they found that the pressure of the gas that the Au nanoparticles were annealed in, highly influenced the Au nanoparticle size reduction rate. Their studies were done in an inert environment consisting of argon gas, at pressures of 10 Pa and 10^5 Pa. The effect of temperature was investigated over the range of 800 ºC - 950 ºC for varying annealing durations [19]. The result of their studies on MgO substrates are shown in Figure 7.

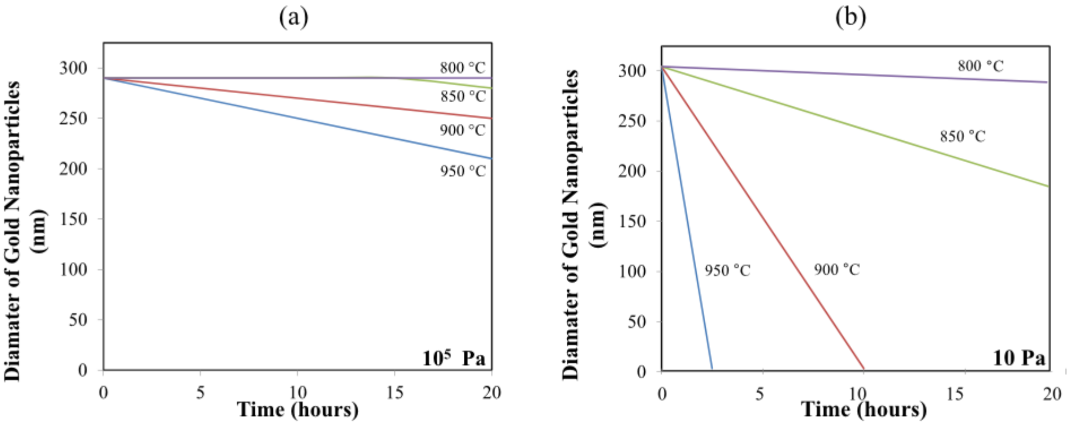

Figure 7: Trends pertaining to size reduction of Au nanoparticles dewetted on MgO substrates in an Ar atmosphere are shown. The influence of annealing temperature and duration, for an Ar pressure of 10^5 Pa is illustrated in (a) and for 10 Pa is shown in (b). Adapted from G. Meng et al., [19].

The two main processes that dominate thermal evaporation are mass transfer via evaporation, and diffusion from the nanoparticle surface to its surroundings. Diffusion is highly impacted by the surrounding pressure. It increases with decreasing pressure, thus, evaporation rates increase significantly by reducing the surrounding pressure [19].

As shown in Figure 7, the size reduction rate of gold particles also depends on annealing temperature. For a given argon pressure, gold particle sizes decrease more rapidly when increasing temperature. This can be explained through the influence of temperature on the saturated vapor pressure of gold. Increasing temperature will increase the saturated vapor pressure of gold, and thus promote evaporation from the surface of the gold nanoparticles [19].

1.2.2.4 Influence of Annealing Temperature on Crystallographic Alignment

Temperature not only influences nanoparticles sizes, but also has a significant role in dictating the crystallographic alignment of dewetted nanoparticles. S. Vasisht and J. Shirokoff [20] studied the preferred orientation of dewetted gold nanoparticles on Si(100) and Si(111) substrates, having native oxides of thickness 2 nm and 3.0-3.5 nm respectively. They used 75 nm thick gold films evaporated onto the substrate at 25 ºC. They investigated the texture of the gold films at three stages: no heat treatment, annealed to 530 ºC for 1 hr, and annealed to 920 ºC for 1 hr, with all annealing treatments taking place in an inert N_2 atmosphere. They found that sufficiently high heat treatments were required to instigate epitaxial alignment between the dewetted gold nanoparticles and the substrate. They observed in-plane texture of the gold nanoparticles at stage 3, on the single crystal Si substrates, where they heated the samples to 920 ºC for 1 hr.

1.3 Au and $MgAl_2O_4$: Fundamental Properties and Relevant Literature

This section includes the relevant properties of Au and $MgAl_2O_4$. Other than their bulk properties, basic concepts and literature related to the nanoscale properties of gold, and surface characteristics of $MgAl_2O_4$, are also reviewed, as they are relevant and important in understanding the system under study.

1.3.1 Gold - Au

Gold is a transition metal with atomic number 79 and has an electron configuration of [Xe] $4f^{14}$ $5d^{10}$ $6s^1$. It is a face-centered cubic crystal with a lattice constant of 4.0786 Å, belonging to the $Fm_{-}3m$(225) space group [21]. As explained in the previous section, various planes/facets of a crystal have different surface energies. The lowest energy surfaces of gold, are (111), (100) and (110) with energies of 1.28 J/m^2, 1.63 J/m^2 and 1.70

J/m^2, respectively. These low energy planes are shown in Figure 8. Note that these values vary within two decimals among various references but the trends remain the same [22].

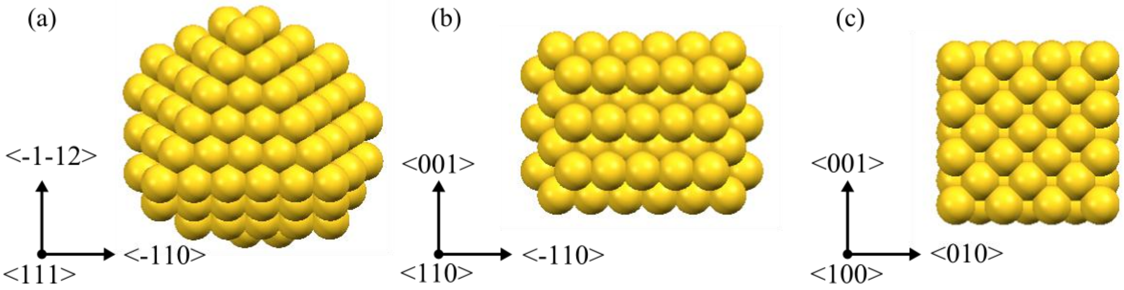

Figure 8: Spacefill model of gold's crystal structure. The three low index terminations corresponding to the lowest energy surfaces of gold are presented; (a) Corresponds to a <111> surface directed out of the page, (b) shows the <110> surface and (c) the <100> surface.

1.3.1.1 Melting Temperature

The melting temperature of bulk gold is 1337.6 K (1064.5 ºC) [23]. Experimental and theoretical studies done by Buffat and Boral indicate that the melting temperature of gold decreases for nanoparticles with diameters in the nanoscale regime [24]. The effect of size becomes significant when the diameter of the nanoparticles approaches 2 nm. Figure 9 illustrates theoretical results that correspond to this behaviour [24].

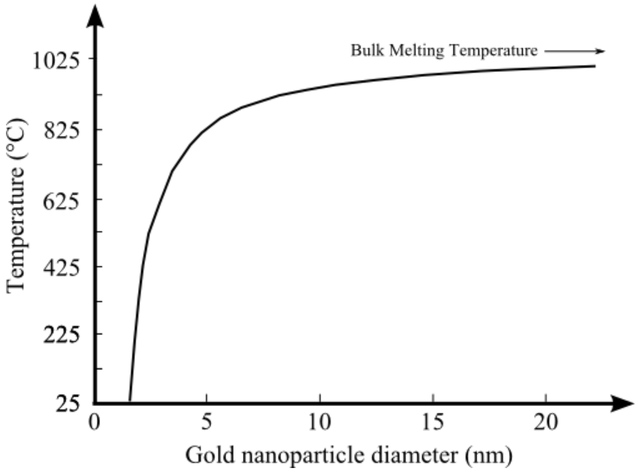

Figure 9: Theoretical values showing the size dependence of the melting temperature of gold nanoparticles. Adapted from P. Buffat and J. Borel, [24].

1.3.1.2 Vapor Pressure

Increasing temperature results in an increase in vapor pressure. Figure 10 illustrates an Arrhenius relationship between temperature and vapor pressure, experimentally measured for bulk gold [25]. Note that the experiments reported in this document are within a temperature range of 20 ºC to 1310 ºC where the vapor pressure of gold varies between approximately 5 mTorr at about 1310 ºC, to virtually zero (3×10^{-49} Torr) at 20 ºC. These numbers are calculated using the best-fit line, suggested by Geiger et al [25].

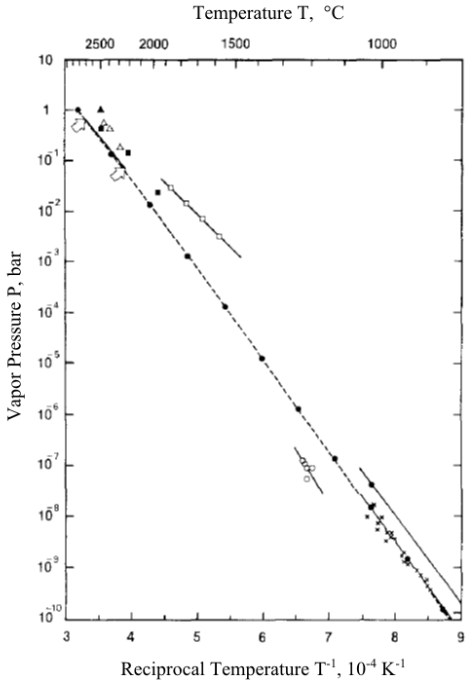

Figure 10: Various experimental measurements pertaining to the vapor pressure of bulk gold as a function of temperature. Reprinted with permission from [25], F. Geiger et al.

Asides from temperature, vapor pressure varies with particle size, as it is a function of the particle's radius. This relationship can be understood through the Kelvin equation presented in Equation 4. It suggests that as curvature increases, vapor pressure will exponentially grow.

1.3.1.3 Relativistic Effects

Bulk gold is chemically inert and is considered to be inactive [7], however, at the nanoscale this is not the case. Relativistic effects provide a theoretical explanation for the observed reactivity of gold nanoparticles [7], [26], [27]. Relativistic effects become considerable for objects having a velocity that approaches the speed of light, *c*. As a consequence, the mass of the object will expand and approach infinity. This can be understood through the mathematical expression below;

$$\lim_{v\to c} m = \lim_{v\to c} \frac{m_0}{\sqrt{\left[1-\left(\frac{v}{c}\right)^2\right]}} = \infty \qquad \text{Equation 5}$$

where m is the relativistic mass, m_0 the non-relativistic mass also known as the rest mass, and v is velocity of the object. For a given atom, the average radial velocity of the 1*s* electrons is $V_r = Z$ [atomic units], where Z is the atomic number. To calculate v/c, c should be converted to atomic units, so $c = 2.998 \times 10^8\ m/s = 137$ atomic units. Therefore, the 1*s* electrons in gold, with an atomic number of 79, have a radial velocity that is (79/137) × 100 = 58% of the speed of light. Therefore, the mass of the electron will increase considerably. Since the Bohr radius of an electron orbiting the nucleus is inversely proportional to the electron mass, relativistic effects will cause the 1*s* electrons to contract. This also applies to the other *s* and *p* orbitals which causes contraction of these orbitals, and increases their electron ionization energy. Figure 11 illustrates the pronounced influence of relativistic contraction on the 6*s* orbitals of Au compared to its neighboring atoms [26].

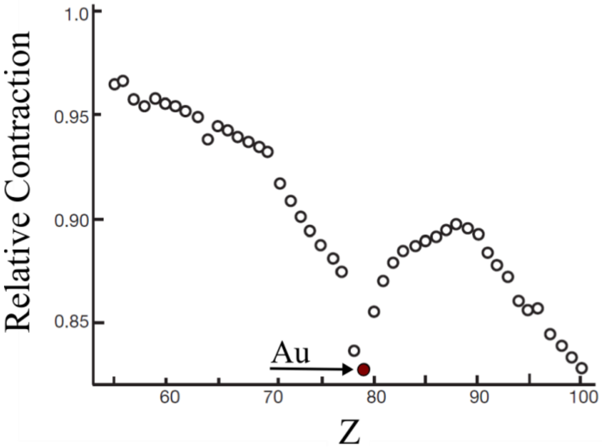

Figure 11: Relativistic contraction, $\langle r \rangle_{rel.}/\langle r \rangle_{non\text{-}rel}$. for the 6*s* orbitals of heavy elements. Pt, Au and Hg are notably influenced, but gold shows the most dominant impact. Modified and reprinted permission from [26], D. Gorin and F. Toste.

A further consequence of the relativistic effect is that the electrons in the *d* and *f* orbitals of gold are better shielded from the nucleus by the contracted electrons in the *s* and *p* orbitals, thus they feel a weaker attraction force to the nucleus and have high reactivity. Surface tension or surface free energy of gold is also larger than what it would have been if relativistic effects were not present [22]. Figure 12 (a) shows the surface energy of the low index surfaces of Cu, Ag and Au with relativistic considerations and (b) shows the difference between surface energy, when relativistic effects are ignored. Au shows the most appreciable influence, when this effect is ignored.

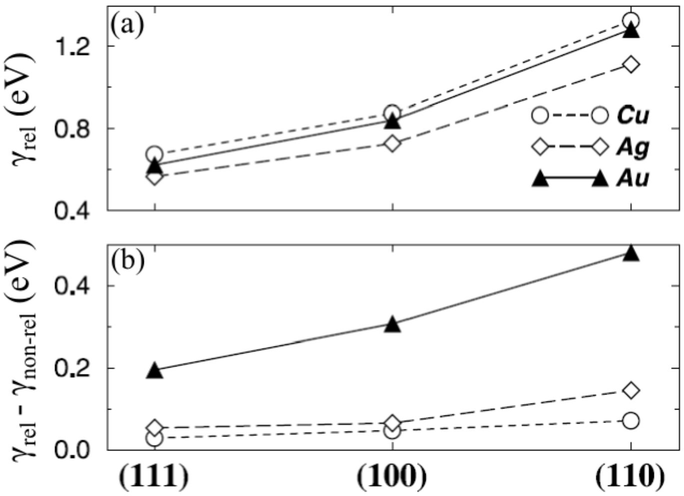

Figure 12: (a) The low index surface energy, in eV/atom, calculated considering relativistic effects. (b) Shows the difference between surface energy calculations with and without relativistic considerations. Of all three noble metals, Au is most affected. Modified and reprinted with permission from [22], Galanakis et al.

Much of gold's unique properties can be explained by the relativistic effect. Of those, the catalytic behaviour of gold at the nanoscale, which is understood by the relativistic effect, is highly relevant to this work. Therefore, it is discussed in more detail in the next section.

1.3.1.4 Catalytic Activity

A catalyst is a material that lowers the activation barrier of a reaction, and hence increases the reaction rate, without being consumed. Catalysts may participate in multiple chemical reactions, but are regenerated at the end of the reaction. The reduced activation energy and enhanced rate of a reaction can be used to identify the presence of a catalyst. In the past few decades, the application of gold as a catalyst has appeared in two rather different contexts; in the first context gold nanoparticles on a reactive support promote charge transfer in various gases, and in the second context gold nanoparticles create preferential nucleation sites for the growth of nanowires or carbon nanotubes.

1.3.1.4.1 Gold as a Catalyst for Charge Exchange in Gases

In this context, gold's catalytic behaviour has been found to be prominent when particles are sufficiently small, below 10 nm [8], and when they are in contact with a reactive support such as TiO_2 and Fe_2O_3. When gold nanoparticles are sufficiently small, the fraction of surface atoms increases and the band structure weakens, making surface atoms behave more like individual atoms and significantly enhancing their reactivity [7], [28]. The superior reactivity of gold nanoparticles is understood through relativistic effects in gold.

Gold nanoparticles have been found to be very active in many reactions such as CO oxidation and propylene epoxidation. Catalytic metals are limited to 12 elements; Fe, Co, Ni, Cu, Rh, Pd, Ag, Pt, Ru, Ir, Os, and Au [8]. The superiority of gold as a catalyst was not established until 1973 when Bond et al. reported on hydrogenation over Au supported on SiO_2 substrates, at temperatures as low as 383 K - 401 K, and by Parravano and his coworkers in 1970 [29] and 1978 [30], for oxygen transfer between CO and CO_2, and reduction of NO by hydrogen transfer reactions over Au/MgO and Au/Al_2O_3 catalysts. In 1983, Haruta et al. found that Au hemispherical nanoparticles deposited on selected metal oxides, show stunningly high catalytic activity in oxidation of CO at temperatures as low as 200 K. These findings increased interest and research in the catalytic nature of Au nanoparticles [8].

In the process of charge exchange over support-based Au nanoparticles, at least one reactant is adsorbed on the edges and corners of Au nanoparticles, for example CO, and the counter reactant, such as O_2, is activated at the perimeter of the gold nanoparticles, where it interfaces the support structures. Au promotes charge transfer between them, converting CO and O_2 into CO_2 [31].

The method in which the gold nanoparticles are synthesized and deposited on the substrate are of extreme importance as they dictate both the size of the gold nanoparticles and their interaction with supports, which both have a crucial role in the catalytic activity of the Au/support system. A combination of small particle size and high Au-support adhesion improves the reactivity of the system. Sample preparation methods can be classified in two main categories; the first is based on preparation of well-mixed precursors, and the second relies on the deposition or adsorption of Au compounds [8]. Of the established methods for preparing catalytic Au nanoparticles, those in the first category are dominantly used, but the second category, which include chemical vapor deposition, relate more closely to the method of sample preparation used in this thesis. Chemical vapor deposition has been effectively used to deposit Au on SiO_2 powder, Al_2O_3 powder and amorphous TiO_2 [32]. Note that these methods are still vastly different from those used in this work, but are still referred to as they may provide an explanation for the novel interaction of Au with $MgAl_2O_4$ that has been reported in this thesis. The specific combination of Au on a $MgAl_2O_4$ support has not been reported for catalytic activity, however, the use of $MgAl_2O_4$ as a support in combination with Ni, for dry reforming of methane to produce synthesis gas ($CO + H_2$), has been studied and prepared using co-precipitation methods. This combination was found to exhibit higher catalytic activity and better stability compared to $Ni/\gamma\text{-}Al_2O_3$ systems [33].

1.3.1.4.2 Gold as a Catalyst for the Growth of Nanowires

Gold nanoparticles used for nanowire growth are most commonly prepared using vapor deposition techniques, followed by heat treatments. Much of the earlier work on nanowire growth used Au as a seed particle, therefore, Au-assisted growth of nanowires is better understood compared to most other seed elements. However, since Au is a deep level trap for Si, it is considered to be a contaminant in semiconductor processing, therefore, much effort has taken place to replace this element in the growth process. To date, a wide range of material combinations and growth techniques has been reported for nanowire growth [34].

In simple terms, the one-dimensional growth of nanowires is caused by preferential growth in one dimension. There exist many models that describe seed assisted growth of nanowires; however, there is no cohesive model that describes nanowire growth which is applicable to all growth techniques and material combinations [34].

The earliest model describing the growth of nanowires was the vapor-liquid-solid (VLS) model proposed by Wagner et al. in 1964. The described system consisted of a vapor-phase precursor ($SiCl_4$), an alloying liquid drop (AuSi), and a solid one-dimensional crystal that formed (Si) through the process. In 1970, Wagner et al. reported on the activation energy of Si nanowires grown with and without the presence of Au nanoparticles. They found the activation energy in both cases to be the same. This indicated that Au did not act as a catalyst in their system. They proposed an alternative role for gold in the system; gold and silicon form a liquid alloy at temperatures below the nanowire growth temperature. The liquid alloy, having a relatively high accommodation coefficient, provides a preferential deposition site for the precursor gases. Thus, the vapor is more likely to decompose at the droplet surface and get incorporated within it. If the precursor gas is continually provided, the droplet will ultimately become supersaturated with Si, therefore, it will precipitate and nucleate at the interface. This proposed growth model is of great importance, but it cannot explain the growth of nanowires in an MBE where the accommodation coefficient is considered to be unity everywhere in the system [34].

Givargizov extensively developed the VLS theory and published his findings in 1975. He suggested that the gold nanoparticles dissociate the precursor materials, at their surface. The decomposed material then diffuses in the gold particle and nucleates at the interface. This work specifically proposed that the growth of the nanowires were due to the catalytic decomposition of the supply gas, at the gold particle surface. Many articles published in literature claim that catalytic decomposition of precursor molecules at the Au, or Au alloy surfaces are responsible for nanowire growth. This remains a point of controversy, since nanowires grown in the MBE, without a precursor gas, also preferentially grow at the substrate-Au interface. Thus, a review article published in 2008 by K. A. Dick, concluded that in some systems, catalysis may play a role in the growth of nanowires, but it cannot be used as a general mechanism to describe the particle-assisted growth of nanowires [34].

Newer models have attempted to provide a more general description that explains the growth of nanowires in various systems. Though they have not yet succeeded in producing a universal model, the emphases of these groups have been the same; preferential nucleation of a material at the particle-substrate interface provides the main driving force for one-dimensional growth of nanowires. The nanowires are understood to preferentially nucleate at the three-line boundary between the vapor, particle, and substrate surfaces [34].

In conclusion, it is not clear if gold nanoparticles act as a catalyst to promote the growth of nanowires, whereas, the role of gold nanoparticles as a catalyst is quite prominent when they are synthesized on reactive supports with length scales less than 10 nm in application to charge exchange in gases. In both applications, the gold-support or gold-substrate boundary seems to play an important role in promoting the catalytic activity of gold nanoparticles.

1.3.2 Magnesium Aluminate Spinel – $MgAl_2O_4$

1.3.2.1 Bulk Properties

Magnesium aluminate spinel is part of a large group of ternary oxides, having a structure of $A^{II}B_2^{III}O_4$ [35]. It is a cubic crystal, with an approximate face-centered close packed structure [35], and belongs to the Fd-3m z(227) space group [36]. It has a lattice constant of 8.0831 Å [37].

The lowest energy surfaces of $MgAl_2O_4$ are (100), (110) and (111) with energies of 2.27 J/m^2, 2.85 J/m^2 and 3.07 J/m^2 respectively [38]. The substrates used in all experiments involved in this thesis, were (111) $MgAl_2O_4$. For (111) $MgAl_2O_4$, oxygen termination is reported to have the lowest energy state, when 42% of the oxygen atoms are removed from the oxygen plane to satisfy stabilization requirements [35], [39]. This is discussed in more detail in the following section. Figure 13 (a) uses a ball-and-stick atomic model to illustrate the stacking sequence of elements for (111) $MgAl_2O_4$ terminated by the lowest energy oxygen plane.

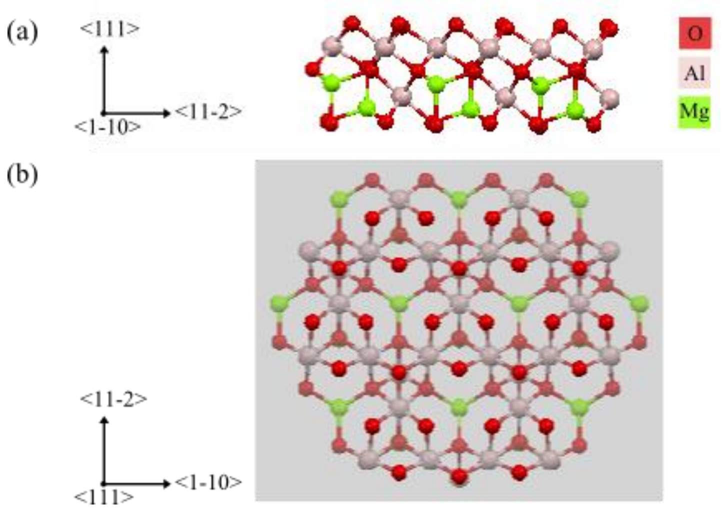

Figure 13: (a) Ball-and-stick atomic model showing the stacking sequence of elements in the <111> direction of $MgAl_2O_4$. (b) Oxygen terminated (111) $MgAl_2O_4$ following the same sequence presented in (a). The gray plane corresponds to the (111) oxygen plane of atoms.

1.3.2.2 Surface Properties

$MgAl_2O_4$, or more generally any material with a so-called spinel structure, is ionic. The repeat units in the normal direction to any low index surface consist of layers with alternating charge. Thus, the termination surface is nominally polar and unstable in the truncated-bulk form [35], [39]. Surface polarity may be compensated by mechanisms involving change of surface stoichiometry, adsorption of charge-compensating species from residual gas, and electron redistribution in the topmost layers of the crystal face [39]. As a result, surface features may vary from bulk. M. K. Rasmussen et. al. used non-contact atomic force microscopy (NC-AFM) in an ultrahigh vacuum with a base pressure of 7.5×10^{-11} Torr to study the (111) surface of $MgAl_2O_4$. The samples were purchased from MTI Corp.; the same provider of the samples studied in this thesis. They were prepared by argon sputtering followed by a heat treatment up to 1150 °C in an oxygen atmosphere of 7.5×10^{-8} Torr. This cleaning cycle was repeated several times until the X-ray photoelectron spectra identified the exclusive presence of Mg, Al and O elements. Since their samples were prepared in an oxygen atmosphere they assumed an oxygen terminated surface. Their experimental results indicated the presence of a hexagonal superstructure with a lattice parameter of 5.7 nm. The superstructure is made of large triangular regions each surrounded by six smaller structures with an apparent triangular outline which is illustrated in Figure 14.

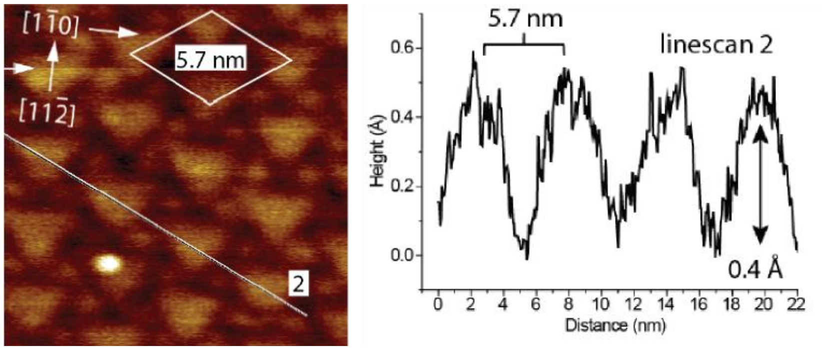

Figure 14: High resolution NC-AFM image of a (111) $MgAl_2O_4$ surface prepared by several cleaning cycles involving argon sputtering followed by annealing treatments to 1150 °C in an oxygen atmosphere. The right side image shows a line scan measurement. Reprinted with permission from [39], MN. Rasmussen et al.

In order to both balance surface charge and explain the structures measured in high-resolution NC-AFM, the authors showed that 42% of the surface O atoms need to be removed. The O atoms are mainly removed along low-density Al lines, which favors the formation of line vacancies instead of randomly distributed vacancies. The Al atoms form a Kagome lattice, so if O is removed along low density aluminum lines, the hexagonal symmetry and triangular structures will form.

M. K. Rasmussen et al.'s surface preparation method involved high temperature annealing, to 1150 °C, of their (111) $MgAl_2O_4$ substrates. Their results indicated that the surface reconstructs and forms triangular terraces. The temperature range they have used is very close to those used in this thesis. Surface reconstruction, under applied heat, has also been observed in the experiments pertaining to this thesis, and is discussed in

Chapter 3. What can generally be taken from this article is that the surface of spinel is not stable, and at temperatures near half its bulk melting point, 2135 °C [37], it reconstructs to form lower energy surfaces.

High temperatures have also been found to affect the surface of other oxide substrates well below their melting temperature. Single crystal sapphire, α-Al_2O_3, has a melting point of 2040 ºC. In a study reported by Yoshimoto et al. annealing at temperatures between 1000 ºC to 1400 ºC led to surface reconstruction in the form of terraces [40]. They investigated various heat treatments in order to gain control over surface smoothness, and found that heating to a relatively low temperature of 1000 ºC for 1 hr, resulted in flatter terraces, whereas annealing to 1400 ºC for 1 hr, led to the formation of terraces with a height of 12 nm.

Aside from $MgAl_2O_4$ surface reforming under high annealing temperatures, surface reconstruction has also been reported by applying a combination of an electric field and heat treatments reported by Y. Yu [41]. Thin films of aluminum, 270 nm - 300 nm thick, were deposited on $MgAl_2O_4$ by electron beam evaporation. When the samples were heated to 620 ºC, which is near the melting temperature of aluminum ~ 660 ºC, a -125 V electric field was applied, with the negative bias on the aluminum surface. High resolution transmission electron microscopy showed that this treatment resulted in $MgAl_2O_4$ surface reconstruction, causing the formation of $MgAl_2O_4$ pyramidal islands.

These results indicate surface instability and reconstruction of $MgAl_2O_4$ and similar oxides, at temperatures well below their melting point. Despite the methods involved being different from those presented in this thesis; i.e. Au-enhanced mass transport of $MgAl_2O_4$, they are all indicative of the vulnerability of the surface of an oxide to reconstruct under appropriate conditions.

1.4 Literature Related to Dewetting of Metals on Oxide Substrates

Since the system under investigation in this thesis involves Au nanoparticles on $MgAl_2O_4$ substrates, much literature was investigated with a focus on metal nanoparticles on oxide substrates. A great deal of this literature reported on mechanisms that enhance control over the size and distribution of the nanoparticles [18], [42], [43], [44], [45], [46], [47], while others studied dewetting phenomena initiated by less conventional methods, such as laser-interference [48], pulsed laser [49], [50], microwave plasma [51], and the electron beam in a scanning electron microscope [17]. These techniques allow for much higher control over heating time scales, and therefore provide more insight into the evolution of dewetted patterns. The literature included applications of oxide supported gold nanoparticles in areas such as improving surface enhanced Raman scattering efficiency [52] and creating negative index materials with potential application to superlenses [53]. It is worth clarifying that in application to negative index materials, lithographic techniques were used to pattern $Ti/Au/Ti/SiO_2/Ti/Au$ on SiO_2 substrates, no heat treatments were involved. In other applications, Ni nanoparticles dewetted on (1-102) r-plane sapphire substrates, were used to promote the growth of vertically aligned, triangular based GaN nanowires [54]. For application to growth of carbon nanotubes, single-wall carbon nanotubes have been grown at relatively low temperatures, using nanometer Fe and Al/Fe/Al multilayer catalyst on SiO_2/Si substrates [55].

Of all the literature that was investigated, only two of the studies corresponded to Au nanoparticles dewetted on $MgAl_2O_4$ substrates, references [1] and [45], while most of the others were on SiO_2. The latter article is focused on finding novel, cost-effective methods for controlling the size and distribution of gold nanoparticles, while the former article corresponds to the preceding work to this thesis; therefore, it is discussed in more detail in the following section.

1.4.1 Preceding Work

A report published by Devenyi et al. on dewetting of thin gold films on $MgAl_2O_4$ substrates showed that the dewetting process, under appropriate annealing conditions, leads to the self-assembly of uniquely shaped nanostructures, comprised of a faceted spherical structure atop of a faceted neck. Such structures were found to form on all (100), (110), and (111) magnesium aluminate spinel surfaces, with varying footprints that mimicked the four-fold, two-fold, and three-fold symmetry of their underlying substrates, respectively. The surface dependent variation in shape of the nanostructures is shown in Figure 15. The authors indicated that these newly identified structures were composed of gold. Since the film and substrate have a lattice mismatch of 0.89% the formation was explained to be dictated by the competing forces of epitaxy, and surface energy minimization. Simulations that were published were constrained to an assumed footprint shape, which was justified by epitaxy as the geometry of the footprint contained the underlying symmetry of the substrate [1].

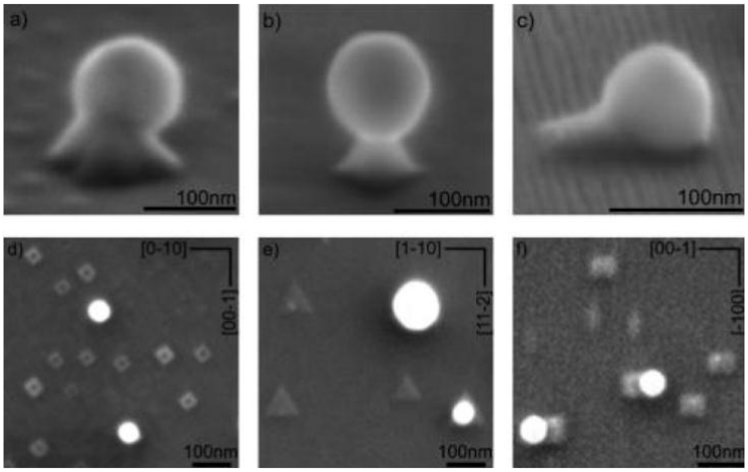

Figure 15: SEM images illustrating uniquely self-assembled structures on magnesium aluminate spinel surfaces, and its dependence on substrate orientation. (a) Corresponds to gold deposited on a (100) oriented substrate, (b) (111) orientated substrate, and (c) (110) oriented substrate. In-plane Miller indices are shown for each substrate orientation. Top row images are at 70° tilt, while the bottom row shows a top view. Reprinted with permission from [1], Devenyi et al. Copyright 2009 from American Chemical Society.

This study was instigated by the small lattice mismatch between the film and the substrate, and was mainly pursued to investigate epitaxial dewetting. As a result of this study, these uniquely shaped nanostructures were discovered, which were referred to as intricate nanostructures [1]. From here on, these uniquely shaped self-assemblies will often be referred to as *intricate* nanostructures to distinguish them from the otherwise expected spherical or hemispherical-like dewetted nanoparticles.

Chapter 2 - Equipment and Methodologies

The experimental procedures applied in this work can be divided into two main categories: (1) Sample preparation and (2) characterization. Sample preparation involved dicing and cleaning $MgAl_2O_4$ substrates, sputtering thin films of gold onto the substrate, and subsequently annealing them. The characterization systems used include scanning electron microscopy, transmission electron microscopy, two dimensional X-ray diffraction, and atomic force microscopy. This section introduces the relevant equipment and methodologies applied in various experiments. It also includes the method used to transfer gold nanoparticles to an epoxy support.

2.1 Substrate Preparation

Single crystal, one and two side polished, (111) $MgAl_2O_4$ substrates, with a quoted roughness of less than 5 Å, packaged in a 1000 class clean room, were purchased from MTI corporation. They were diced using a LoadPoint MicroAce 3 dicing saw, with a diamond impregnated resin blade, made by CISCO, G1A851 SDC320R13B01. The spindle speed was 15000 rpm, the feed rate was 2 mm/sec, and the lubricant used was water. The sample sizes varied based on the limitations of the various sample holders that were used in different processing or characterization steps. As an example, the original custom-built substrate holders used for coating substrates with a thin film of gold, were designed specifically for square samples, with a side length of 6 mm, 8 mm, or 10 mm, therefore, samples were cut to these dimensions. The process of dicing creates $MgAl_2O_4$ powder, which makes it necessary to re-clean the surface of every diced $MgAl_2O_4$ substrate, prior to thin film deposition.

The cleaning procedure involved three main steps; substrate wiping with lens paper (VWR Scientific Products), manual irrigation, and sonication. 2-propanol high purity liquid chromatography (HPLC), methanol HPLC, and/or acetone distilled in glass were used in all three steps. The details of this cleaning procedure are presented in Appendix A. Solvent residue and contaminants were found to affect the self-assembly of gold nanoparticles on the substrate. The applied cleaning procedure proved to be very effective in reducing the number of particulates on the substrate surface that were visible using low magnification light microscopy. Imaging was mainly done at 5 X – 10 X magnification with the Olympus BX-61 reflection microscope.

To specifically show that solvent residue affects the self-assembly of the gold nanostructures, acetone was dropped on a clean $MgAl_2O_4$ surface and was left there to evaporate. A thin film of gold was then deposited on the substrate, and subsequently annealed. Figure 16 shows the effect of solvent residue on the self-assembly of the gold nanoparticles; it significantly affects gold nanoparticle distribution and size. It may also lead to odd anomalies, such as those surrounding the gold nanoparticles shown in the inset of Figure 16. For this reason, every substrate was evaluated, post cleaning for solvent residue and other visible contaminations, using low magnification light microscopy. Samples were re-cleaned if contamination was evident and distributed over the entire substrate surface. If the contamination was localized, then its location and approximate size was recorded, and avoided in the characterization process.

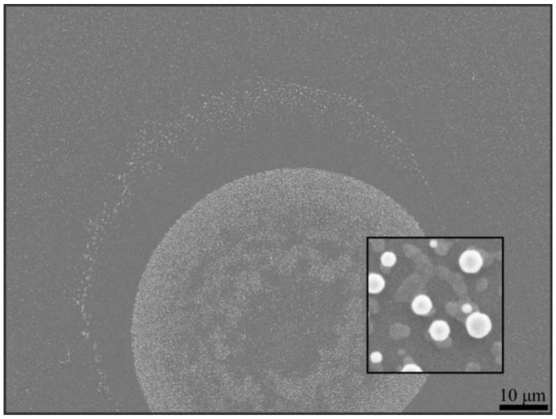

Figure 16: Effect of solvent residue on the self-assembly of gold nanoparticles; Solvent residue provides preferential sites for growth of nanoparticles creating regions of high density surrounding by empty space. The inset corresponds to a high magnification image of the nanoparticles. The nanostructures are surrounded by non-uniform, unidentified material deposits.

The substrate surface was also imaged, using atomic force microscopy, both prior to and post sample cleaning, to evaluate the effect of wiping on the surface. The only noticeable difference was in the number of particulates on the surface, which had decreased post substrate cleaning.

2.2 Deposition System

Thin films of gold were sputtered onto $MgAl_2O_4$ substrates, using a GATAN PECS Model 682 ion beam coating/etching system. This system has a wide scope of capabilities that allows slope cutting, sample etching, and/or high-resolution sputter coating. It is conventionally used to prepare samples for scanning electron microscopy, transmission electron microscopy, and optical microscopy [56]. In the current project it was used for two applications: (1) depositing thin films of gold on $MgAl_2O_4$ substrates for direct application to the results presented in this thesis and (2) coating the self-assembled gold nanoparticles as a prerequisite for scanning electron microscopy, since the substrate is non-conductive. The main reasons for selecting this deposition system is its high throughput combined with a reliable thickness measuring unit, a quartz crystal microbalance. A single substrate can be coated in less than 10 minutes meaning that within one hour several different samples can be prepared using distinct parameters. The limitations to this system are in the substrate size, which must be less than 30 mm, and in the substrate temperature, which cannot be controlled or changed. The substrates are left at ambient temperature through the deposition process.

The parameters used for depositing gold films were kept constant through all the samples that were prepared and reported in this thesis; they are listed in Table 1.

Table 1: Experimental settings used for sputtering thin films of gold onto (111) $MgAl_2O_4$ substrates.

Accelerating Voltage	5 keV
Left gun current	~150 µA
Right gun current	~150 µA
Deposition rate	0.9 Å/s
Sample rotation	60 RPM
Sample tilt	0º
Sample rocking	0º
Pressure	$\sim 5 \times 10^{-5}$ Torr

2.3 Annealing System and Heat Treatments

Dewetting and self-assembly of thin gold films sputtered onto $MgAl_2O_4$ substrates was induced by thermal treatments, mainly by using a Lindberg Hevi-Duty quartz tube furnace under an inert argon atmosphere. 99.9995% purity argon flows at 100 cubic centimeters per minute (ccm) from the gas cylinder (Air Liquide Medical), through the quartz tube, and exits after passing a two stage gas bubbler filled with high vacuum oil.

Electric heating elements provide the furnace heat, measured by a thermocouple, placed in the center of the top lid, and are controlled by a CN4800 temperature controller. All the temperature readings from the temperature controller were referenced to a bath of ice water, using a reference junction type R, Pt-13% Rh vs. Pt, thermocouple. To reference the temperatures that are measured and displayed by the temperature controller, the sensing junction of the thermocouple was placed at the center of the quartz tube, in line with the furnace's original thermocouple. The reference junctions of the thermocouple were then placed in a bath of ice and water so that they were at ~ 0 ºC, while the leads connecting to the reference junctions were attached across a voltmeter. The temperature controller was set to temperatures that were commonly used in the experiments of this thesis, and held at each temperature for 1 to 2 hours. This allowed the temperature to stabilize; then a voltage reading was made, and converted to temperature using an appropriate reference table.

Figure 17 shows the readings made directly from the furnace's temperature controller, referred to as the set temperature, versus the actual temperature, which was measured with reference to a bath of ice water. It is worth mentioning that in the rare case, where an alternative furnace was used, the same referencing process was applied to ensure that all temperatures indicated in this work are referenced to ~ 0 ºC. All the temperatures referred to in this script, are the actual temperatures, i.e. temperatures referenced to 0 ºC, and not the temperatures that were read out by the furnace's temperature controller.

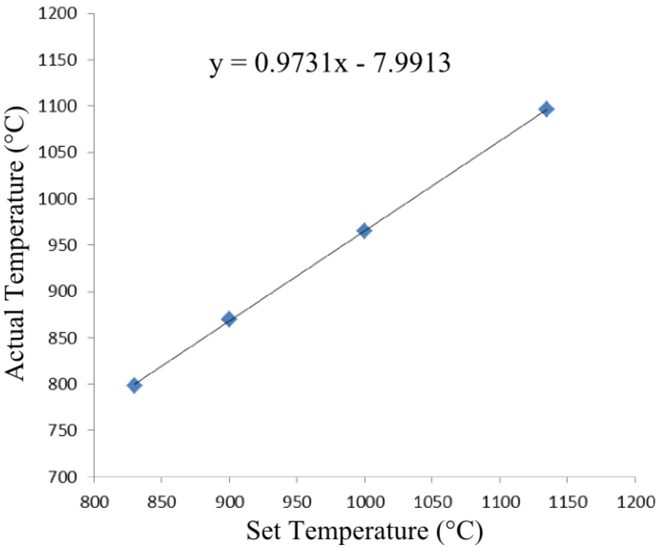

Figure 17: Referencing the furnace temperatures to a bath of ice water, ~ 0 ºC. Actual temperatures indicate the temperatures measured with an external type R reference junction thermocouple, with the reference junctions immersed in a bath of ice-water, and the sensing junction centered in the tube furnace. The set temperature refers to the temperatures programmed into the furnace's temperature controller.

Temperature profiles can vary in many ways; the number of applied heating stages, the heating and cooling rates at each stage, and the duration at which the furnace is kept at a specific temperature. Given the number of variables, a vast range of heat treatments can be programmed into the temperature controller. To limit the investigated parameter space to a manageable size, the temperature profiles investigated in this work mainly follow similar trends to those described by Devenyi et al. [1], however, heating profiles at intermediate temperatures were also investigated. The applied heat treatments can be categorized into five groups, and have the general trend of increasing annealing temperature and duration, starting from heat treatment 1 and ending at 5:

Heat treatment 1: samples are heated to 640 °C in 35 minutes and are then cooled to room temperature over a few hours.

Heat treatment 2: samples are heated to 940 °C in 60 minutes and are left to cool to room temperature over a few hours.

Heat treatment 3: samples are heated to 1060 °C in 80 minutes, and are held at this temperature for 25 minutes. They are then cooled to 965 °C in 0.5 hrs, and held there for 1 hr. After this, the samples are cooled to 30 °C over 14 hrs.

Heat treatment 4: samples are heated to 1110 °C in 1.5 hrs, and are held at that temperature for 1.5 hrs. They are then cooled to 965 °C in 0.5 hrs, and held there for 2 hrs. Subsequently, the samples are left to cool to 30 °C over 14 hrs.

Heat treatment 5: samples are heated to 1310 °C in 1.5 hrs and are held there for 1.5 hrs. They are then cooled to 1020 °C in 0.5 hrs and are kept there for 2 hrs. Then after, they are left to cool to 30 °C in less than 14 hrs.

2.4 Characterization Methods and Systems

2.4.1 Scanning Electron Microscopy

Scanning electron microscopy (SEM) allows for imaging and characterization of heterogeneous organic and inorganic materials on a nanometer and micrometer scale [57]. In this system, an electron beam is created under vacuum, by an electron gun which can be tungsten hairpin, lanthanum hexaboride, or field emission. They vary in spot size, stability of the electron beam, and lifetime. Field emission guns provide the smallest beam size, which allows for higher resolution imaging, and have the longest lifetime. To further reduce the beam spot size on the specimen surface, and therefore improve the imaging resolution, various electron lenses and apertures are employed. The apertures block part of the beam and reduce its diameter, whereas the electron lenses magnify the beam. Electromagnetic coils are also used to correct for stigmation, and raster the beam across the specimen, so that electron signals are gathered point by point and converted into a shade of gray correlated to the signal yield at each point. A variety of signals are created from the interaction of the electron beam with the specimen, including: secondary electrons (SE), backscattered electrons (BSE), X-rays, Auger electrons, and cathodoluminescence. Identification and analysis of each of these signals requires an appropriate detector. Figure 18 schematically illustrates the main components of a scanning electron microscope, as well as the various signals that may be emitted by the specimen.

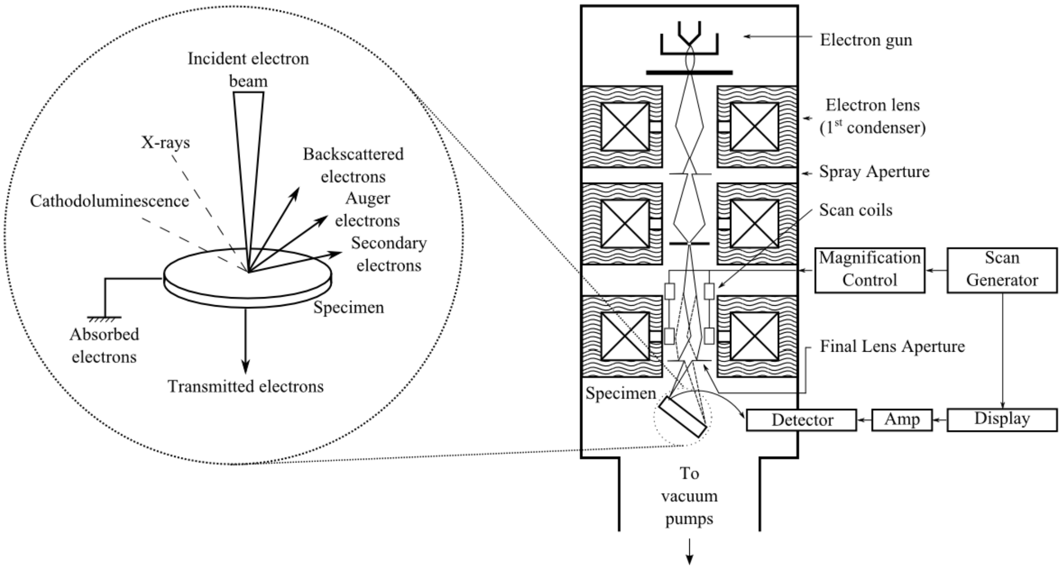

Figure 18: Schematic diagram of a scanning electron microscope showing the electron gun, lenses, scanning coils, detector and the various signals generated from the interaction of the electron beam with the specimen, modified from Goldstein et al., [57], and Tesker Corporation, [58].

Two types of microscopes were utilized for the work presented in this thesis; JEOL JSM-7000F and the FEI Magellan 400 at McMaster University's Canadian Center for Electron Microscopy. All BSE imaging, EDS and EBSD work presented in this thesis, were done by the JEOL JSM-7000F. All SE imaging, except for those that state otherwise, were also done using this system. The JEOL JSM-7000F is equipped with a Schottky field emission gun and an Everhart-Thornley detector for detecting secondary electrons. The FEI Magellan 400 microscope allows for imaging at much lower voltages, with a smaller beam size and current. It also has various detectors that can better detect and distinguish SEs from BSEs compared to the Everhart-Thornley detector. Therefore, the Magellan makes it possible to perform high resolution and high quality imaging of non-conductive samples, which is very useful, since $MgAl_2O_4$ is highly insulative. This instrument was not available for direct use by students, and thus was used only a limited number of times, where it was important to image the samples without applying a conductive coating.

All images taken with the JEOL JSM-7000F were coated with a thin film of carbon or platinum. Carbon was selected for the conductive coating layer when the samples had to be characterized by EDS, EBSD, or XRD post SE imaging. Otherwise, platinum was chosen for coating the samples, because of its faster deposition rate, and superior conductivity. The conductive coatings were applied using GATAN PECS Model 682 ion beam coating/etching system. Generally, a low accelerating voltage of 5 keV for platinum and 8 keV for carbon was used to prevent any damage to the gold nanoparticles caused by the incident sputtered material. A high sample rotation of 60 rpm, sample tilt of 40^{o} and a rocking rate of 40 degree/second were employed. This allowed for more conformal coating of the particles, which reduced imaging artifacts that are described further in this section.

All samples were scanned at two to five different locations, using different magnifications ranging between 8000 X - 110000 X. Scanning at different locations provided a survey across the sample, to ensure that features seen were not localized, while the different magnification sizes allowed imaging of features of different length scales.

2.4.1.1 Secondary Electron Imaging

Secondary electron imaging provides a means of obtaining topographic and morphological information from a specimen. Secondary electrons are produced as a result of inelastic scattering between the impinged beam and the electrons within the specimen. Sufficiently low energy electrons within the electron beam will lose their energy to the specimen, when interacting with it. The lost energy will be transferred to the valence electrons of the specimen, giving them enough energy to escape the atom. The escaped electrons are called secondary electrons and have very low energy. Thus, secondary electrons can only escape the specimen if they are within a depth of ~5 nm for metals and 75 nm for insulators [59]. Otherwise, they will lose their energy through consecutive inelastic scatterings within the specimen.

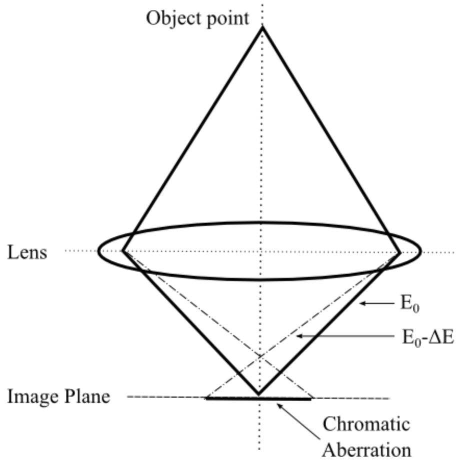

Figure 19: Schematic diagram showing the origin of chromatic aberrations. Electrons with different energies are focused to different points on the image plane by the electromagnetic lenses, creating a focused disc instead of an ideal point. Modified from Goldstein et al., [57].

Reducing the energy of the electron beam enhances the SE signal. However, it increases a specific type of aberration known as chromatic aberration. Electrons emitted from the source have slightly different energies of E_0, and $E_0 - \Delta E$, where the variation in energy, ΔE, depends on the type of electron source that is used. Electrons with different energies are focused at different points on the image plane. Thus, the focused beam forms a disk instead of an ideal point of focus. The diameter of this disk is proportional to $\Delta E/E_0$. Therefore, by reducing the energy of the electron beam, chromatic aberration increases [57]. Figure 19 schematically illustrates the origin of chromatic aberration.

Secondary electron yield increases with increasing tilt as shown in Figure 20. This property of secondary electrons in combination with the fact that they are only correlated to the top few nanometers of the structure being imaged, make SEs the tool of choice to study morphological and topographical features on a micrometer and nanometer scale. However, if higher energies are applied, then most of the information will be from BSEs or noise, thus, eliminating or reducing topographical features.

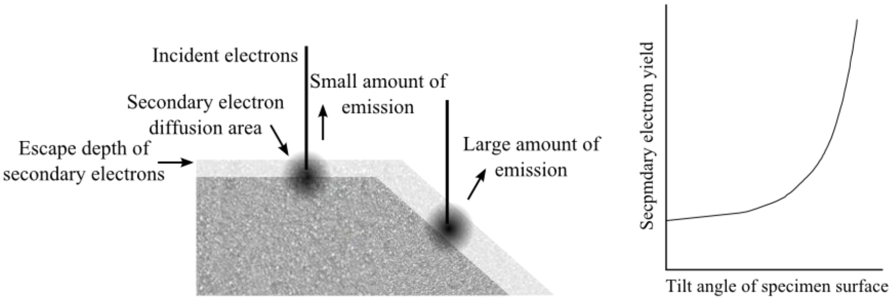

Figure 20: Secondary electron yield versus tilt angle with respect to surface normal. Left image modified from Tesker Corporation [58]. Right image modified with permission from Goldsteirn et al. [57].

A common artifact of imaging in the SE mode is known as the edge effect. The effect makes edges appear brighter in a SE image. This has been proposed to be related to the large path length of the electrons, within the escape depth, at the edge of the specimen [59].

2.4.1.2 Backscattered Electron Imaging

When high energy electrons from the beam impinge on the specimen, they interact elastically with the electric field of the nuclei within the specimen. Therefore, very little energy is transferred from the incident electron to those within the specimen. The incident electrons scatter within the specimen and are either absorbed, or escape from the surface. The escaped electrons are called backscattered electrons (BSE). Their interaction volume depends on the average atomic weight of the material they are incident upon. If the beam is incident on a material with a low average atomic weight, then it can penetrate further in before it begins to scatter, resulting in a teardrop-shaped interaction volume. Whereas, heavier elements, cause scattering at earlier stages. As a result, they have lesser penetration depths, creating a hemispherical interaction volume. These interaction volumes are shown in Figure 21.

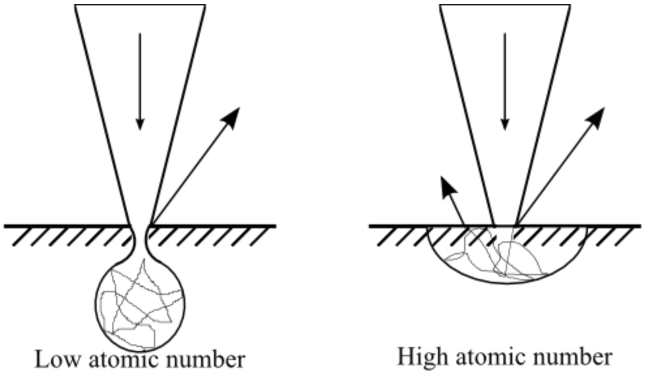

Figure 21: Variation of the interaction volume for low and high atomic numbers.

Backscattered electron yield depends on the average atomic weight of the atoms that lie within the beam-specimen interaction volume. A higher average atomic weight increases the yield of BSEs. Thus, BSE imaging provides compositional contrast information.

2.4.1.3 X-Ray Energy Dispersive Spectroscopy

X-ray energy dispersive spectroscopy (XEDS or EDS) can be used for identification, and semiquantitative analysis of elements present within the beam-specimen interaction volume. Inelastic scattering of the incident beam with the specimen generates X-rays. They can be categorized in two main groups; the bremsstrahlung continuum, and characteristic X-rays.

Beam electrons decelerate in the Columbic field of the specimen’s atoms and emit a photon. Since the interactions are random the electrons may decelerate and emit photons with any amount of energy from zero up to the original energy of the incident electron, and will have wavelengths characteristic to X-rays. Thus, they create a continuum of X-ray signals known as the Bremsstrahlung continuum shown in Figure 22 (a).

Characteristic X-rays are created when the electron beam interacts with the tightly bound inner shell electrons of the specimen’s atom, exciting them so that they can free themselves from the atom and create vacancies, see Figure 22 (b). Higher energy electrons may then relax to fill these vacant spots, and therefore emit X-ray photons with energies that are characteristic to that specific element. Based on atomic theory only transitions between certain subshells are allowed, thus, characteristic X-rays are limited to those allowed electron transitions. Such characteristic peaks, are sharp and strong in intensity, and correspond to electron transitions between atomic subshells.

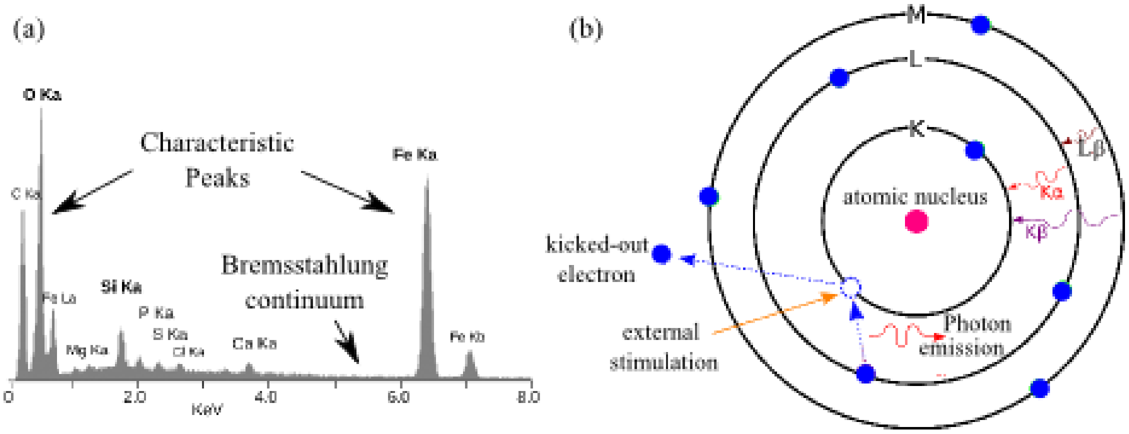

Figure 22: (a) X-ray spectrum of mineral crust showing the Bremsstrahlung continuum, K-series, and L-series peaks measured by EDS. Image from Corbari et al., reused under a CC BY-SA 3.0 [60]. (b) Schematic diagram of energy levels within an atom and electron transitions corresponding to L-series and K-series characteristic peaks. It also illustrates X-ray (photon) production. Modified from Muso [61].

Selecting the correct beam energy is very important because the peaks for every element must be identified unambiguously. This means that for every element more than one type of characteristic peak, i.e. both K-series and L-series should be identified and resolved. If the beam energy is not sufficient, it cannot excite high energy characteristic peaks of an element. In some cases, a range of energies must be experimented to obtain both a signal from high energy peaks, and to deconvolve overlapping peaks at lower energies.

2.4.2 Transmission Electron Microscopy

In scanning transmission electron microscopy (STEM) an atomic size electron beam is scanned over a thin specimen. The electrons that transmit through and are scattered by the specimen, may be detected, and are used to acquire structural and compositional information of the specimen [62].

Transmission electron microscopy (TEM) or STEM requires specimens to be sufficiently thin, allowing the incident electron beam to be transmitted through it. Such thicknesses are not readily available and require specific preparation techniques prior to imaging. In the present work, STEM samples were prepared in multiple stages, starting with the Focused Ion Beam (FIB), continued with a Nano Mill, and ended with gentle argon plasma cleaning.

The FIB was used to mill a region of interest, having a length of 10 µm and a width in the range of tens of nanometers, from the substrate. Samples were sputter coated with 5 nm - 7 nm of carbon, to prevent charge buildup when imaging the sample in the FIB. A Zeiss NVision 40 FIB was used to create a site-specific TEM thin-foil specimen. To start, the sample was imaged so that a line of about 10 µm in length, containing specific features of interest was selected. Then, a thick layer of carbon was deposited, to prevent damage to the specimen through the ion milling process. The deposition was done in two stages; first by electron-beam (e-beam), then by ion-beam decomposition of an organic gas near the region of interest on the specimen. E-beam decomposition is gentle and prevents damage to the gold nanoparticles, which is why it was selected as the first stage in specimen coating. However, since it is a slow deposition process, when the carbon layer is sufficiently thick, coating is continued with the Ga ion beam. After coating the sample with over 2 µm of carbon, micro-milling of the specimen begins. The sample is cut into a thin foil using a 30 kV gallium beam. When it is thin enough so that it becomes transparent to a 3 kV e-beam, it is cleaned for 1 minute with a 10 kV ion-beam, and 2 minutes by a 5 kV ion-beam. The specimen is then imaged by a conventional TEM (Philips CM12) to identify if it is sufficiently thin. Further thinning takes place using the Nano Mill (Model 1040), as it allows for more gentle removal of material. An argon beam of 500 eV to 900 eV with a current of 120 pA to 130 pA, was applied to each side of the sample, tilted to +/- 8º, for 10 to 30 minutes. When the specimen was sufficiently thin for high resolution TEM imaging, it was plasma cleaned in the Solarus Model 950 plasma cleaner, using the machine's $5H_2/O_2$ plasma recipe.

The prepared samples were then characterized using an aberration-corrected FEI Titan 80-300 Cubed scanning transmission electron microscope (STEM). High angle annular dark field and bright field imaging, electron energy loss spectroscopy, and energy dispersive X-ray spectroscopy were all done to acquire crystallographic, structural and compositional information of the specimen.

2.4.2.1 Bright and Dark Field Imaging

Bright and dark field imaging refers to STEM imaging techniques that employ certain detector settings so that only a select range of scattered electrons can be detected. High energy electrons incident on a TEM specimen may experience forward elastic scattering, meaning that the incident electron is transmitted through the specimen, with no energy transfer. The scattering profile of such electrons will depend on their incident energy, as well as, the atomic number/weight of the scattering atom. When considering the interaction of the beam with the specimen instead of an atom, other effects such as specimen thickness, tilt, density and crystallinity will also affect scattering events [62]. Annular detectors are used to collect scattered electrons within a defined angular range, which is then converted to an intensity signal corresponding to the coordinates of the location probed on the specimen. Since the scattering angle is sensitive to atomic number, the image created may provide compositional contrast information.

The angular collection range of the detector defines a few imaging techniques. High angle annular dark field (HAADF) imaging refers to the case where the inner collection angle of the detector, β, illustrated in Figure 23, is at least 2 to 3 times the convergence angle α. The collected signal is very sensitive to the atomic number and is approximately proportional to $Z^{1.7}$. Therefore, it provides chemical contrast and structural information of the specimen. Heavier elements appear brighter in such images. Low angle annular dark field (LAADF) images are formed by signals collected within a β range that is at most 2 to 3 times α. Annular bright field images (ABF) are correlated to signals detected within the illumination cone, but avoid the most intense central signals [62].

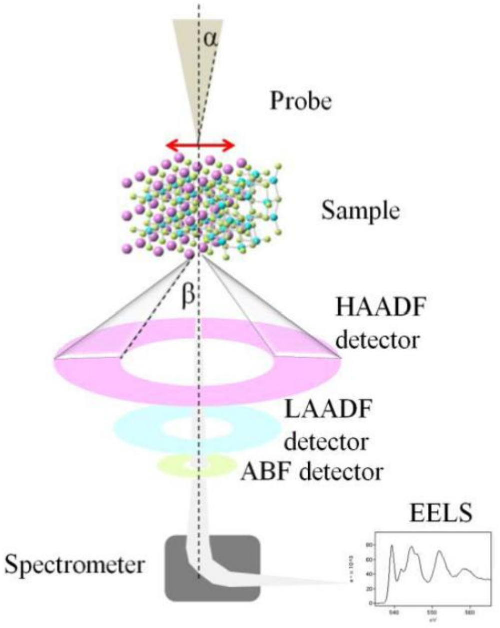

Figure 23: Schematic illustration of HAADF, LAADF, ABF and EELS detectors within a scanning electron microscope. Reprinted from [62], Image by G. Zhu, from the open access dissertations and thesis.

2.4.2.2 Electron Energy Loss Spectroscopy

Electrons with a narrow and known energy range are incident upon the specimen. A spectrometer is used to measure the energy loss spectrum of the incident electrons. Some electrons will undergo elastic scattering and therefore have no energy loss, contributing to a sharp and intense zero loss peak on the spectrum. The width of this peak is mainly dependent on the energy distribution of the electron source and related optics, and indicates the limit of the experimental energy resolution. Other electrons will undergo inelastic scattering and lose energy. This results in several low intensity peaks with energy > 50 eV that arise from core electron relaxation to empty states caused by inelastic scattering. These peaks are characteristic to the elements present within the probed region of the specimen and therefore can be used for elemental analysis. [62].

2.4.3 Two Dimensional X-ray Diffraction

Typical interatomic distances within a solid are on the order of 1 Å. Therefore, an electromagnetic probe of the atomic structure of a solid would need to have a wavelength of at least this distance. X-rays have such characteristic wavelengths [63]. X-ray diffraction (XRD) techniques can be employed for a wide range of applications and analysis methods including but not limited to phase composition analysis, unit cell lattice parameter identification, residual strain, crystal structure, epitaxy, texture, and crystalline size identification [64].

2.4.3.1 Experimental Setup

XRD measurements were performed using a Rigaku RU-200 Cu rotating anode X-ray generator (Rigaku MSc, The Woodlands, TX) with an average wavelength of 1.5418 Å .It is equipped with parallel-focusing monochromator optics, a 0.5 mm diameter pinhole collimator, a Bruker 3-circle D8 goniometer (Bruker AXS Inc., Madison, WI), and a two-dimensional Bruker Smart 6000 CCD detector (1024 × 1024). The detector was placed at a distance of 4.2 cm away from the center of the sample surface.

Data for texture analysis was collected using four different scans described by the standard Eulerian angles of ω, ψ, and φ shown in Figure 24. The Bruker APEX2 software was used for data collection. In all scans, ψ was fixed at 35.2°, or equivalently χ_g defined by 90° - ψ, was set to 54.8°, and 2θ, the angle between the incident beam and the detector, was set to - 60°. In scan 1, ω was kept fixed at 170°, while φ was scanned from 0° to

360° at 0.5° intervals. This type of scan where ω is kept fixed and φ varies, is referred to as a phi scan. In scans 2, 3 and 4, ω was scanned from 170° to 120°, with 2° intervals, with φ fixed at 0°, 120° and 240° respectively. These scans, having φ fixed and ω change, are called omega scans. The exposure time for each scan, or frame, was 10 s. The translation axes, X, Y and Z were set so that the surface of the sample was at the center of the diffractometer, and the parallel beam was incident on the region of interest. The collected data was then configured into stereographic projections (pole figures) of the (111), (200) and (220) reflections using GADDS (Bruker-AXS) software. In this thesis only the (111) reflections are presented, as the other reflections were only used to verify the preferred orientations identified using the (111) pole figure.

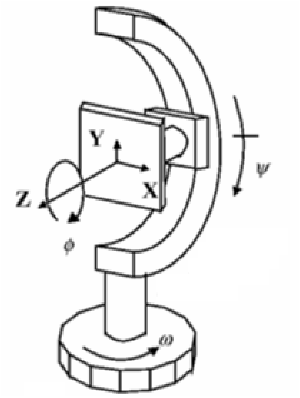

Figure 24: Schematic diagram of the X-ray goniometer, the translation axes (X, Y, Z), and the Eulerian angles (ω, ψ, φ). Modified with permission from [65], B. B. He.

2.4.3.2 Semi-Quantitative Analysis

Maximum pole intensities were obtained from pole figures using the box cursor option in GADDS. The cursor was used to center a box on each peak which would then output the maximum pixel intensity within the box. Of the peaks that corresponded to a specific preferred orientation, those that did not overlap with peaks from other orientations were selected to measure the maximum intensity contribution. If more than one peak for a given orientation was free from overlap, then the average of their maximum intensities was used to represent the specific contribution from that orientation. In the case of the

(111) peaks of gold, where all the peaks overlapped with the (222) reflections of spinel, a different approach was used. The ratio of (222)/(311) reflections of spinel were measured on a bare sample. When gold was present, the (311) reflections of spinel, which were all free from overlap, were measured. Knowing the ratio of the (222)/(311) reflections of spinel measured from a bare substrate, and having the intensity of the (311) reflections of spinel in samples with gold nanoparticles, the contribution of spinel's (222) reflections on the substrate with gold nanoparticles were identified and subtracted from where the (111) peaks of gold overlapped with the (222) peaks of spinel. Ultimately, for all preferred orientations, all overlaps were accounted for by either the first, or second approach, or a combination of the two approaches when necessary. It is important to note that for semi-quantitative analysis, the frames were integrated over a wide 2θ range spanning from 34º - 40º. This allowed for consistent coverage of most of the contribution from both (222) and (311) reflections of spinel, reducing the error caused from inferring the contribution of spinel's (222) reflections, based on the reference sample. Wide integration ranges are not ideal as all the data within the integration range are averaged, which increases the background noise contribution to the measurement. However, it was necessary for the semi-quantitative analysis. A narrower 2θ range from 38.0° to 38.6° was used to identify all the peaks, and to display the pole figures in this thesis.

2.4.3.3 Basic Principles

Some of the X-rays that interact with the sample will undergo elastic scattering. The distribution of the scattered reflected X-rays depends on the electron distribution, and therefore the atomic arrangement i.e. the crystalline nature and structure of the sample. Thus, the intensity and spatial distribution of the scattered X-rays form a pattern that is specific to the crystallographic properties of the material it interacts with. If atoms are arranged in a periodic array, with long-range order, as in polycrystalline or crystalline materials, then the scattered X-rays will interfere with one another and form diffraction patterns. The interference behaviour of reflected X-rays can be described in real space using Bragg's Law, or in reciprocal space using the Laue equations. Bragg's law states that a lattice spacing of d results in a path difference of *2dsinθ*, between reflected rays, and thus the condition for constructive interference is given by:

$$n\lambda = 2d\sin\theta \qquad \text{Equation 6}$$

where λ is the wavelength of the source, θ is the angle between the impinged beam with the reflected planes, and n is an integer number, known as the order of reflection. It means that for a given d-spacing, and θ angle, Bragg's diffraction condition can be satisfied for various X-ray wavelengths. The integer *n* is commonly considered to be 1 because higher order reflections can equivalently be considered as diffraction from lattice planes with a spacing of *d/n* [65]. Figure 25 illustrates the variables corresponding to the Bragg diffraction equation.

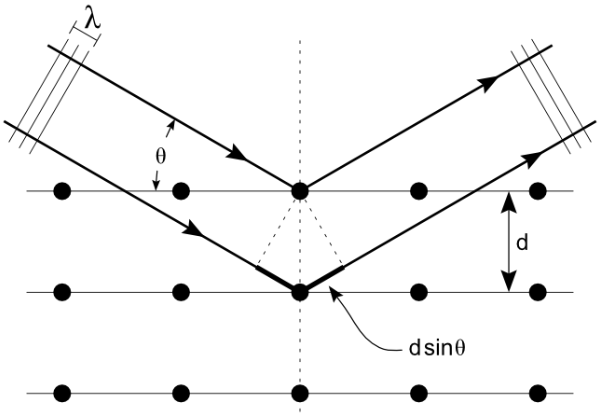

Figure 25: Schematic diagram showing constructive interference explained by Bragg diffraction, and all the variables employed in the corresponding equations. Modified and reprinted under a CC BY-SA 3.0 [66]. Original image by Hydragyrum.

In a given X-ray measurement, λ is constant and is determined by the X-ray source. The set of d-spacings are constant and material dependent, thus the θ angles, between the incident beam and the scattering planes is the variable dictating the condition for constructive interference. In practice, the incident beam is often kept fixed, so the condition for Bragg diffraction depends on how various planes within a specimen are aligned. That is why it is useful to have a goniometer head with three degrees of freedom.

It allows the angle θ to be varied during experimental data collection, so that Bragg's condition for diffraction can be satisfied for more *d*-spacings within the crystal. Now, if this single crystal material was ground into a fine powder, then every grain would be randomly oriented. Statistically, for all possible d-spacings of a given material, there would exist grains that are aligned with the beam such that the condition for Bragg diffraction is satisfied and therefore, a peak would appear on a diffraction intensity vs. 2θ plot. It is important to note that diffraction peaks that exist for a given material, when it is measured in powder form, are characteristic to every material. That is, materials having different crystal structures will have diffraction peaks at different 2θ values. This is because the *d*-spacing depends on crystallographic structure and lattice constant, which is material specific.

The von Laue formulation for constructive interference is equivalent to the Bragg condition, however the approach used is different; no assumption of specular reflection is made. A condition for constructive interference is found for all scattered X-rays off lattice sites in reciprocal space. As a result, the Laue condition states that constructive interference will occur if the change between the incident wave vector, and the scattered wave vector, $\boldsymbol{K} = \boldsymbol{k'} - \boldsymbol{k}$, is a vector of the reciprocal lattice, therefore, it provides a transformation from one lattice point to another. This can be visualized using the Ewald sphere. Consider a sphere in reciprocal-space, centered about the end of a wave vector $\boldsymbol{k}$, and having a radius of k. $\boldsymbol{k}$ is the wave vector of the incident beam in the direction $\boldsymbol{n}$ defined by $\boldsymbol{k} = 2\pi\boldsymbol{n}/\lambda$. To satisfy the Laue condition, there should exist a scattered X-ray with wave vector, $\boldsymbol{k'} = 2\pi\boldsymbol{m}/\lambda$, in direction $\boldsymbol{m}$, such that the reciprocal lattice point, lies on the surface of the sphere, and is distinct from the lattice point on the origin, O. In this case, a transformation can be made by $\boldsymbol{K}$, from one lattice point to another. [63] A 2D schematic diagram of the Ewald sphere is shown in Figure 26.

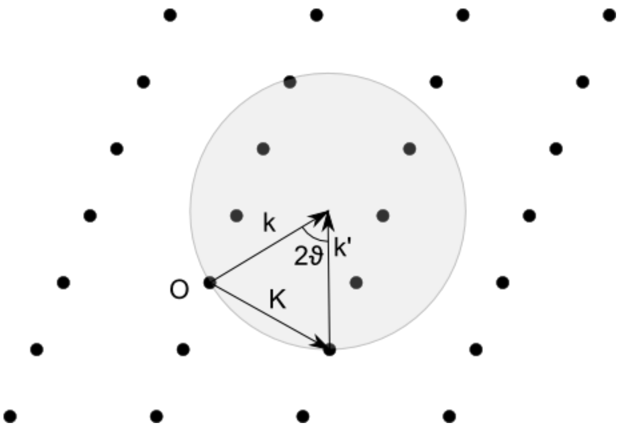

Figure 26: Two dimensional illustration of the Ewald construction. Modified and reprinted under a CC BY-SA 3.0 [67]. Original image by Wiso.

In practice, and in the measurements done in this work, the ***k***-vector, corresponding to the incident beam is kept constant; therefore, the Ewald sphere remains unchanged. Instead, the orientation of the crystal is varied by rotating the specimen about some fixed axis. As the crystal rotates, the reciprocal lattice also rotates, about the same axis, and the same amount. Thus, every reciprocal lattice point travels a circular path, and constructive interference occurs when this circle intersects the Ewald sphere at a lattice site. The diffraction peak is recorded by a detector and appears as a bright spot in its corresponding image frame. The rotation of the sample, and therefore the reciprocal lattice space is schematically shown in Figure 27 for a simple single crystal material. Using a 2D detector, the information collected from all frames, including phi and omega scans, accumulate to create a hemisphere in three-dimensional space and can then be stereographically projected to create a pole figure.

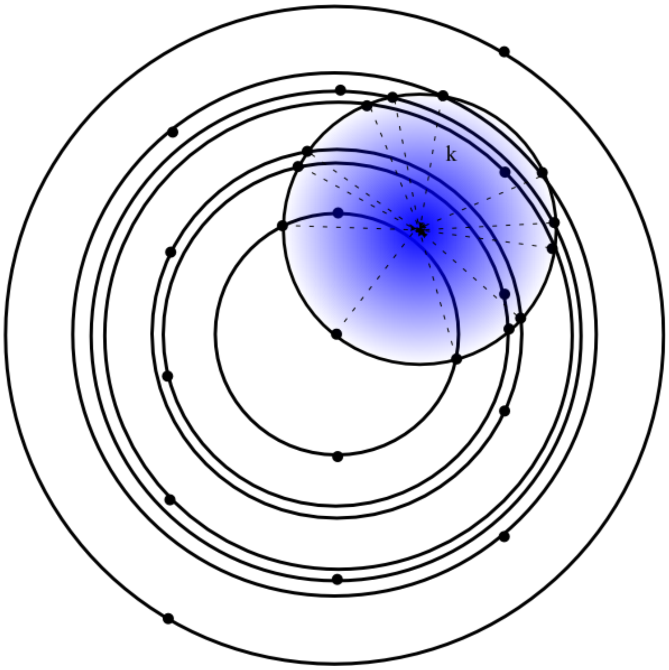

Figure 27: Schematic representation of the Ewald construction and a crystal lattice in reciprocal space, rotated about a fixed axis. Vectors of length |k| are indicated by dashed lines. The Ewald sphere remains unchanged through the rotation of the crystal. If the resolution of rotation is high enough, as the crystal rotates it will intersect the Ewald sphere at its lattice points, creating the required condition for Bragg diffraction. Modified from Ashcroft & Mermin, [63].

2.4.4 Atomic Force Microscopy

Atomic force microscopy (AFM) was used to obtain topographic information, when limited by the resolution of the SEM. A Caliber atomic force microscope by Veeco, operated in tapping mode was used for sample characterization. All samples were scanned at two to four different locations, with multiple scan sizes ranging between 3 µm to 25 µm, at each location. Scanning across a range of locations provided a survey over the sample surface, to ensure generality of the evident features, while the different magnifications resolved features of different sizes.

AFM is of the family of scanning probe microscopy (SPM), a family of microscopy where a sharp probe is scanned across a surface so that the probe-sample interaction can be monitored [68]. Figure 28 schematically illustrates the operation of an atomic force microscope.

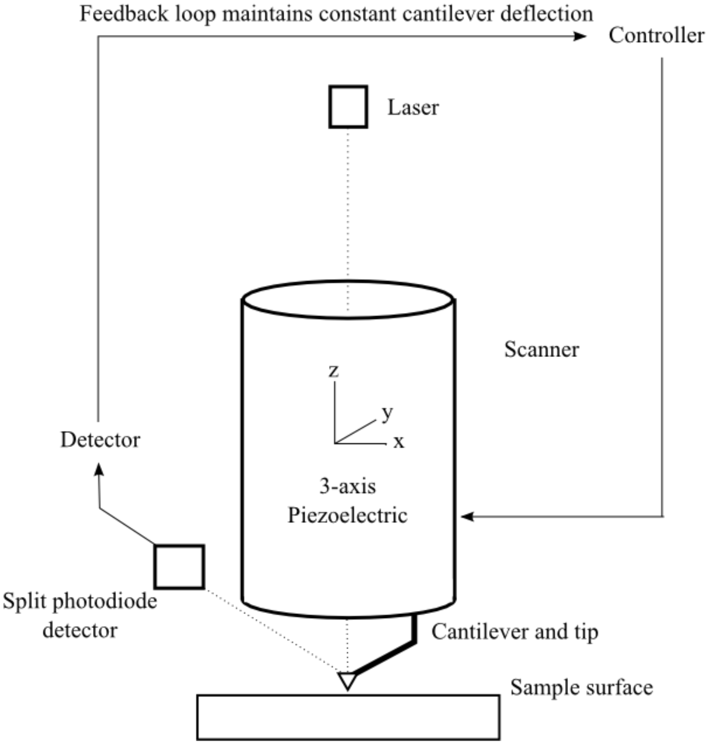

Figure 28: Schematic diagram of an atomic force microscope. Vertical and lateral piezoelectric scanners control the location and height of the cantilever. A laser beam is focused on the tip of the cantilever so that deflection and/or oscillations of the cantilever can be monitored by a split photodiode. The signal is put through a feedback loop. The piezoelectrics adjust themselves so that the interaction of the probe with the specimen remains constant. These adjustments are then used to create various forms of images. Modified from Veeco Instruments Inc., [68].

2.4.4.1 Contact Mode AFM

The cantilever deflection, measured by variations in reflection of a laser beam off the cantilever, is correlated to the distance of the cantilever from the surface. In contact-mode AFM the microscope feedback loop keeps the cantilever deflection constant by moving the piezoelectrics so that a constant distance is maintained between the specimen and the cantilever. Therefore the distance the piezoelectric moves vertically at every (x,y) point is recorded by a computer and is used to configure a topographic image of the surface [69].

The feedback loop of an AFM is not instantaneous, therefore the vertical deflection of the cantilever will not be constant during imaging. The AFM software can display the deflection signal as a line plot, and/or as an image, as the tip scans the surface of the specimen. The size of the deflection signal is a measure of how much the cantilever has deflected before the deflection is corrected by the feedback loop through the vertical piezo. That is why this signal is also known as the "error" signal, since in an ideal system the piezo would simultaneously adjust itself to maintain constant tip deflection. Rapid slope variations in topography promote deflection signals. Therefore, it is sometimes used to obtain qualitative information of surface topography. However, no height measurements can be made from a deflection image [69].

The third signal available in contact mode AFM is derived by the lateral twisting of the cantilever, and is commonly referred to as lateral deflection. The friction encountered by the tip, through the scanning process, causes lateral twisting of the cantilever. This twisting is detected and used to gain insight into the shape of the surface and its frictional properties. That is why this technique is sometimes called friction force microscopy and the signal is referred to as the friction signal.

Contact mode AFM has high scan speed and can provide atomic resolution however, lateral and normal forces reduce spatial resolution and may damage the sample or the tip.

2.4.4.2 Tapping Mode AFM

In tapping mode AFM the cantilever is oscillated, commonly by a piezoelectric element with a large amplitude in the range of 1 nm to 100 nm. As the cantilever approaches the specimen surface, the interaction between the probe and the surface, may dampen the oscillation frequency and its amplitude. These oscillations are monitored and the amplitude is put through a feedback loop, so that the z-adjust piezoelectric element can change its height and keep the amplitude fixed. Therefore, the vertical variations of the piezoelectric at every (x,y) point are used to map the topographic features of the specimen surface. Figure 29 shows the general principle for tapping mode AFM [69].

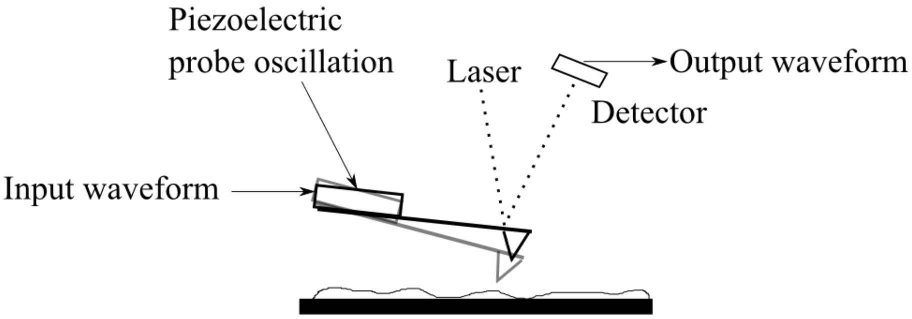

Figure 29: Schematic illustration of atomic force microscopy in tapping mode. The cantilever is oscillated by a piezoelectric element. As the cantilever scans the surface, the oscillations will be influenced by the interaction between the probe and the surface. These oscillations are monitored through the deflections of a laser beam focused on the probe, and it is analyzed with a split photodiode. Modified from Eaton & West, [69].

Ideally, the amplitude would remain constant however, rapid changes in slope will change the amplitude signal before the feedback loop can correct for the amplitude variation. Similar to the deflection signal in contact mode AFM, the amplitude variations are considered to be an error signal, but provide topographic contrast information. Height measurements cannot be made from amplitude images [69].

Phase images are the third type of images produced via tapping mode AFM. Phase images map the phase shift of the cantilever oscillation, as it scans the specimen's surface. The shift in phase will vary based on the energy dissipated between the tip and the sample, which depends on many properties of the surface under study, including viscoelasticity, adhesion and contact area. Since contact area varies with slope, the phase shift will also contain topographic contrast information. This image is commonly used for mechanical characterization of surfaces. To reduce ambiguity in the signal source, it is best to use flat samples, thereby eliminating phase shift from topographic contrast [69].

Tapping mode AFM has high lateral resolution. Virtually no lateral forces are present. Its scan rate is slightly slower than contact mode AFM, but overall it is the preferred mode of operation under atmospheric pressure and was used for measurements pertaining to this work. All three types of images: topography, amplitude and phase were created and saved, however, only topography images are presented, as they are best suited for displaying topographic variations, which was the reason for using this characterization technique.

2.5 Gold Nanoparticle Liftoff and Transfer to an Epoxy Carrier

The gold nanoparticles that self-assemble on a (111) $MgAl_2O_4$ substrate can be removed from the substrate and transferred to an epoxy host, while they mostly maintain their crystallographic orientation. The employed procedure was adapted from a patent by Jovanovic et al. concerning thin film liftoff, [70]. The process employed here involves application of an adhesive layer which bonds to the gold nanoparticles, followed by rapid cooling, so that the adhesive layer can be easily detached from the substrate, while having the gold nanoparticles embedded in it.

Prior to depositing the adhesive, Parafilm® M (Pechiney Plastic Packaging) was used to create a rim surrounding the substrate. A small piece of Parafilm was folded several times to create a 2 mm thick film. The film was then placed on top of one edge of the sample so that it covered roughly 1 mm of the edge of the specimen. It was then pressed down to diminish any gap between the substrate and the Parafilm. This was repeated on the other three edges of the specimen. One to two drops of optical paste (Norland optical adhesive 61) was applied to the substrate surface, in the region bound by the parafilm ledges. The ledges allowed the optical paste to spread within the bounds, leaving the optical paste surface flat. If the ledges were not there, the epoxy would form spherical cap, covering the substrate. The adhesive was exposed to UV light for one minute, and then placed on a hotplate for about 12 hr at 50 ºC. At this point, the optical paste was fully adhered. One corner of the Parafilm ledges was gently pulled on. This caused the Parafilm to thin and ultimately detach from the substrate. This was done to all four sides, so that no Parafilm was left on the specimen. Then the specimen was dipped in liquid N_2 for about 30 seconds. After extracting the specimen from liquid N_2 the optical paste detached from the substrate spontaneously, so no significant force or effort was required to detach it.

However, tweezers were used to separate the epoxy from the substrate immediately after removal from liquid N_2, to prevent re-bonding. At this point, gold nanoparticles were embedded in the epoxy at the surface at which the epoxy interfaced with the substrate. By visually inspecting the specimen, one could typically determine which areas had significant transfer of gold nanoparticles to the epoxy film, as those regions appeared clear on the substrate, whereas areas with low nanoparticle removal maintained their original color prior to lift off. The color depends on the initial film thickness of gold. The epoxy was flipped over so that the surface with the gold nanoparticles faced in the upright direction. Owing to the Parafilm rim that was created at the start, the backside of the epoxy remains smooth making it relatively easy to mount the epoxy film on another substrate or substrate holder for further characterization.

Chapter 3 - Results and Discussions

The solid state dewetting of thin films of gold on (111) $MgAl_2O_4$ substrates was investigated and the results are presented in this chapter. Solid state dewetting involves a large parameter space including but not limited to the following: substrate material, substrate orientation, substrate surface patterning, film material, film deposition method, film thickness, heating method, heating profile, ambient pressure, gas flow, and gas composition. The focus of this study was to investigate the role of the heating profile and film thickness on the formation of $MgAl_2O_4$ nanostructures. The discovery of the $MgAl_2O_4$ nanostructures is presented in section 3.1, with no detail provided regarding the temperature profiles, or corresponding thicknesses. These details and their influence are covered in sections 3.2, and 3.3. Sections 3.4 and 3.5 include an overall discussion, summarizing the results, and suggesting potential methods for the self-assembly of $MgAl_2O_4$ nanostructures. Section 3.6 investigates a means for transferring the gold nanoparticles, from the substrate to an epoxy carrier.

3.1 Discovery of the Self-assembled Crystalline $MgAl_2O_4$ Nanostructures

In pursuit of investigating the odd self-assemblies reported by Devenyi et al. [1], the intricate nanostructures were recreated. Figure 30 shows intricate nanostructures self-assembled by annealing a thin gold film deposited on a (111) $MgAl_2O_4$ substrate. These structures were prepared following a similar procedure proposed by Devenyi et al. [1] The base shape and orientation with respect to the substrate are consistent with their results.

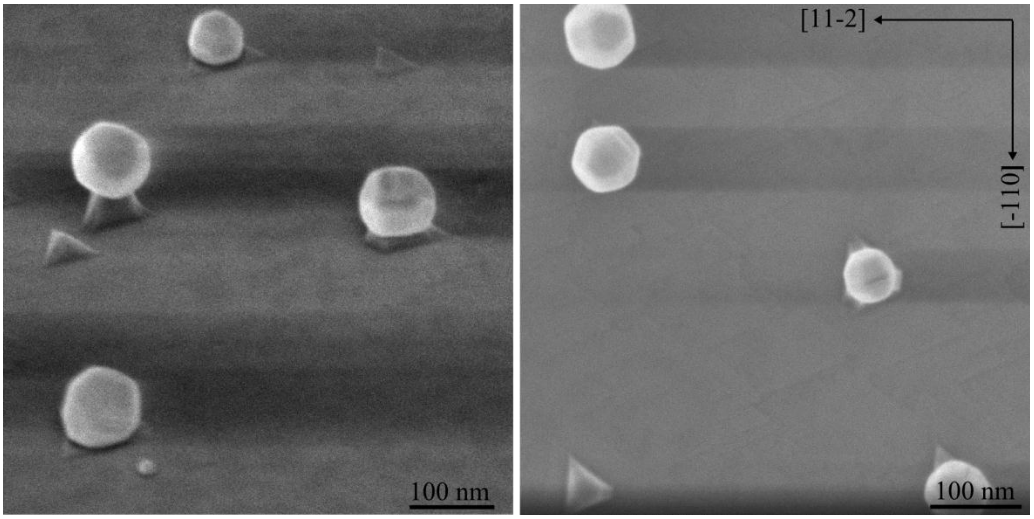

Figure 30: SEM images of intricate structures self-assembled by annealing a thin film of gold on a (111) $MgAl_2O_4$ substrate. The left image was taken with the sample at a 50º tilt, and the right image shows a top view. The streaks are related to charging effects caused by the interaction of the electron beam with the insulating substrate.

The imaging in Figure 30 was done using the FEI Magellan 400, and therefore did not require the application of a conductive coating layer prior to imaging. The high resolution images obtained from this system, illustrated surface modifications across the entire substrate surface. That is, the surface appeared to be covered with triangular structures of minute heights. When evaluating the bare surface of spinel using SEM or AFM imaging techniques, these features were not apparent. Therefore, the surface modifications were either related to the presence of gold, the annealing profile, or the combination of gold and annealing profile.

To investigate this matter further, a substrate was prepared and annealed following the same procedure that had led to intricate structure formation, except, the sample was not coated with gold and was kept bare. This sample was then compared to a clean bare substrate that had not been annealed. Since the features under investigation were very flat, AFM was found to be most suitable for inquiring topographic information. The results of the comparison were striking yet clear. The process of annealing the substrate resulted in the surface reconstruction of magnesium aluminate spinel as shown in Figure 31. The surface reconstructed to form triangular shaped flat terraces across the entire surface. The average surface roughness post annealing was measured to be 6 Å, with the tallest structure, which was an exceptional case, having a height of about 4 nm.

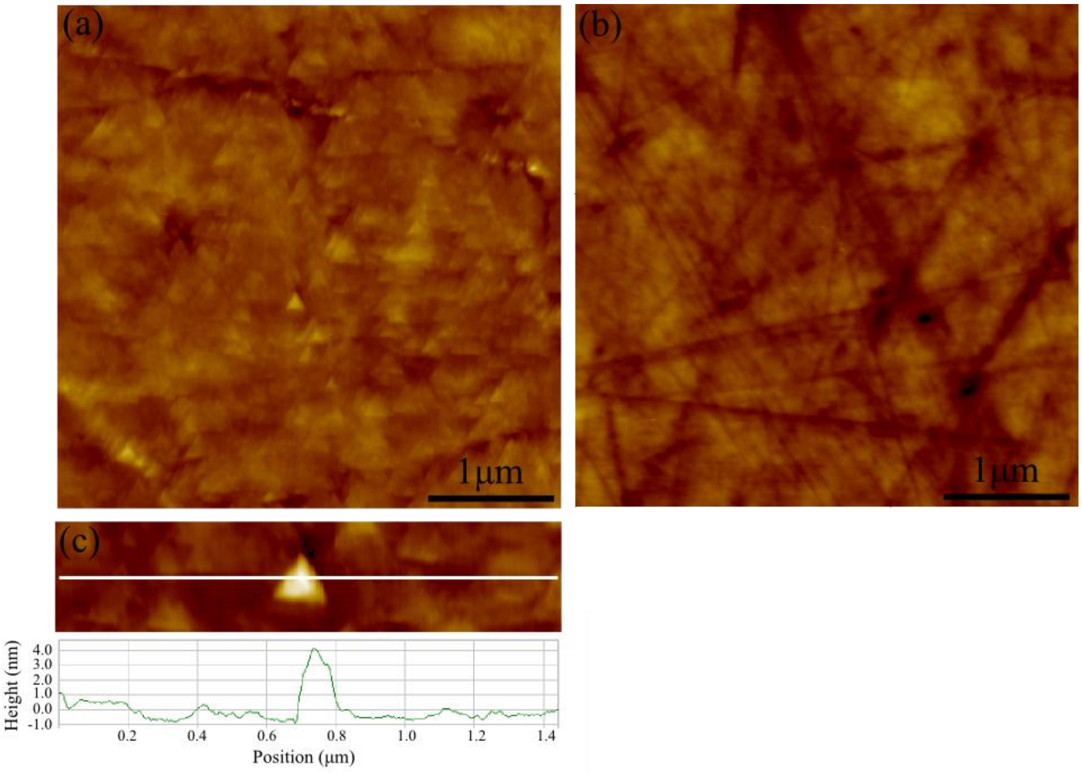

Figure 31: Topographic images acquired using tapping mode AFM. Scans were measured on (111) bare $MgAl_2O_4$ surfaces. (a) Bare substrate annealed following a profile that would have led to the formation of intricate structures if gold were present. (b) Unannealed bare substrate. (c) A line profile of the tallest triangular structure self-assembled through annealing the bare substrate.

Comparing these surface reconstructions to those reported by M. K. Rasmussen et al. [39], which was described in detail in Chapter 1, the following is found; in both cases, the (111) $MgAl_2O_4$ substrates were annealed to temperatures over 1000 °C, the surface reconstructs to form triangular terraces, the triangular terraces are uniformly aligned and have the same crystallographic orientation with respect to the substrate. The structures evident in the two systems differ in size by two orders of magnitude. These differences may be related to the variation in sample preparation method. These results strongly indicate that the surface of $MgAl_2O_4$ is unstable at elevated temperatures. It can reconstruct to form lower energy surfaces, well below its melting point. However, the surface reconstructions have very flat profiles, with an average height of less than 1 nm.

The fine surface reconstructions, covering the substrate surface, that were discussed earlier in connection to Figure 30 can now be correlated to the $MgAl_2O_4$ surface reconstruction at high temperatures. However, this still does not provide an explanation for the intricate self-assembly of nanostructures shown in that image. As described in Chapter 1, the sphere-and-neck nanostructures shown in Figure 30 had previously been exclusively regarded as gold nanoparticles. However, at this point it became questionable whether the necking structures were in any way related to the unstable surface of $MgAl_2O_4$ reconstructing at high temperatures. This was investigated through high resolution STEM of cross-sectional specimens containing individual intricate nanostructures. This technique provided insight into crystallographic orientation, defects, elemental composition, and compositional contrast, which all aided in understanding the specifics of the nanostructures.

STEM high-angle annular dark-field images shown in Figure 32 revealed that the necking structure carried the same lattice and compositional contrast as the $MgAl_2O_4$ substrate. As well, energy dispersive X-ray spectroscopy measurements on that region detected only signals from magnesium, aluminum and oxygen elements. The collected measurements, indicated that in contrast to what was previously published, the necking structures are not gold, but in fact $MgAl_2O_4$ that has self-assembled below the gold nanostructures through the process of high temperature annealing in an argon atmosphere.

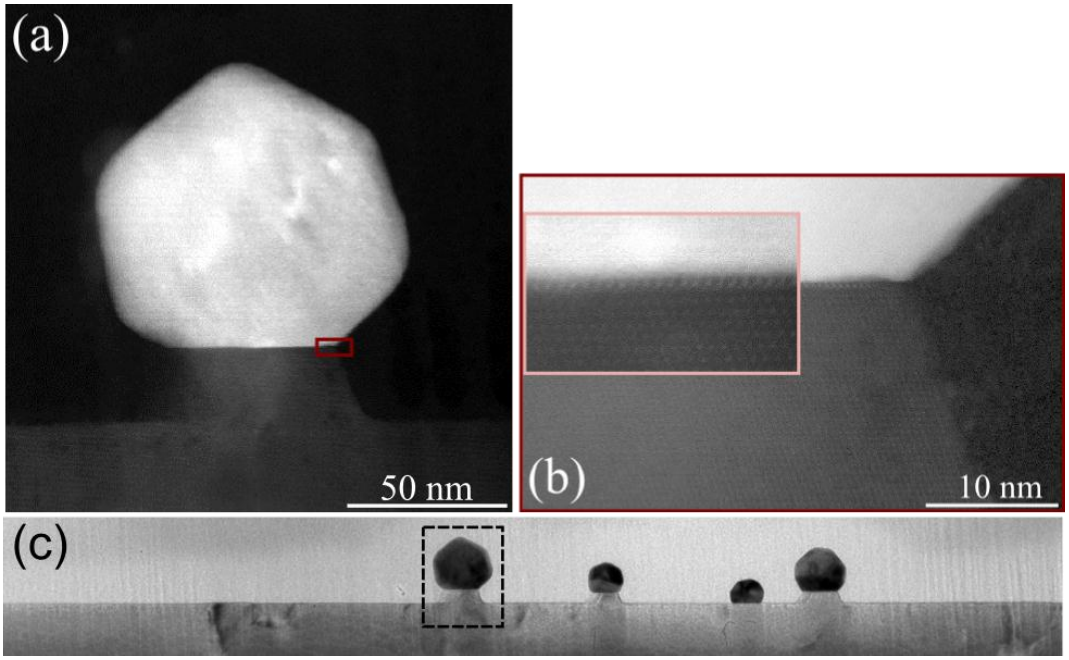

Figure 32: (a) STEM-HAADF image of an intricately shaped Au-$MgAl_2O_4$ nanostructure, self-assembled by dewetting gold on (111) $MgAl_2O_4$ substrate. (b) High resolution HAADF image of the selected region in (a). It illustrates a unique interfacial phase separating the faceted gold nanoparticle, from the self-assembled magnesium aluminate nanostructure. The substrate is in <1-10> projection. The gold component of the structure did not have the same zone axis as the substrate. (c) Shows a low magnification bright field TEM image of the specimen. The boxed particle corresponds to the magnified nanoparticles in images (a) and (b).

Depositing a gold film on the magnesium aluminate substrate prior to annealing, enabled the self-assembly of $MgAl_2O_4$ nanostructures, with heights in the range of tens of nanometers. For the bare substrate, the dominant structure heights were less than 1 nm. This is evidence that the presence of gold, is key to the development of $MgAl_2O_4$ nanostructures.

The high resolution inset in Figure 32 also revealed an interesting layer at the gold-spinel boundary. Analysis of the Au-$MgAl_2O_4$ interface unraveled the presence of a unique, interfacial phase, separating gold on one side and magnesium aluminate spinel on the other [71]. Using electron energy loss spectroscopy techniques, high resolution chemical information was obtained across the interface. Comparison of the EELS maps showed a chemically sharp boundary, where gold is separated from $MgAl_2O_4$, showing no signs of cross-diffusion [71].

In order to better identify the constituent atoms and their arrangement at the interface high-angular, medium-angular, and low-angular dark-field imaging was performed, which allowed for the distinction between elements of heavy and low atomic weight. The largest and smallest atomic numbers in the system of study correlate to Au with atomic number of 79, and O with an atomic numbers of 8. Since EELS did not identify elements other than Au, Mg, Al and O near the interface of this system, the brightest spots in HAADF images were assumed to be Au atoms, at and above the interface, and Al atoms beneath the interface. The brightest spots in LAADF images were assumed to be O atoms, and in the MAADF images, the brightest spots were evaluated as Mg contribution. Using this assumption, the HAADF image in Figure 33 shows the presence of Au atoms at the interface, since their contrast is similar to that of bulk gold, while the LAADF image shows the presence of oxygen at the interface. G. Zhu used this information to design an atomic model, which was inputted in STEM simulations, for comparison to experimental results [71]. From this it was found that an atomic model consisting of Mg, O, Al, Au-O, Au-O, Au-O, Au atomic layers building up from the $MgAl_2O_4$ lattice to the Au lattice, best agreed with experimental results. The insets in Figure 33 show the TEM simulations and the atomic models used, side by side.

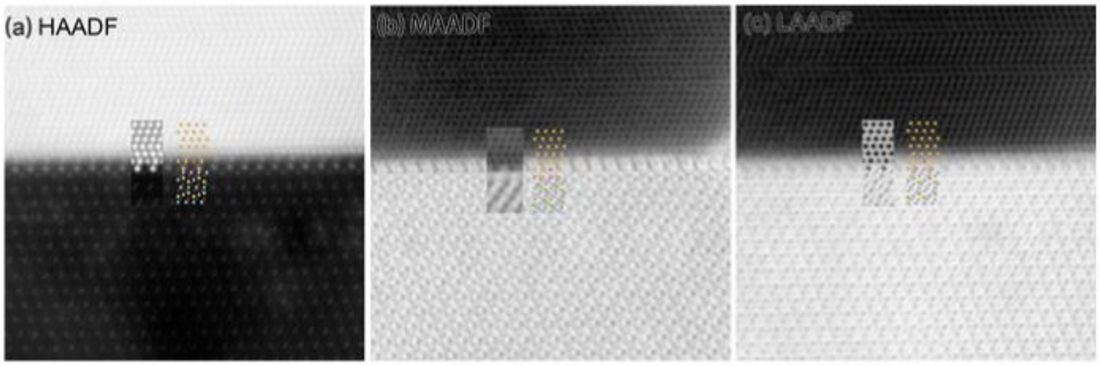

Figure 33: High resolution STEM images of the Au - $MgAl_2O_4$ interface. (a) HAADF: 65-200 mrad, (b) MAADF: 13-131 mrad, and (c) LAADF: 8-65 mrad. The insets in each image show the simulated STEM image on the left and the atomic models used on the right [71]. The color code applied in the atomic model follows; gold: yellow, oxygen: red, aluminum: blue, and magnesium: green.

Another important observation made from studying atomic resolution images of the Au-$MgAl_2O_4$ interface is that the gold atoms observed in this layer adopt the lattice spacing of the $MgAl_2O_4$ lattice. This can be seen in Figure 33 from the presence of an extra atomic column of gold, above the interface. This extra column can be traced down to a gap that lies between every second atomic column of gold sitting at the interface.

While high resolution transmission electron microscopy provided invaluable insight regarding the nature of the intricate Au-$MgAl_2O_4$ nanostructures, the measurements were localized and limited to very few particles. Two-dimensional x-ray diffraction provided a means of textures analysis over a relatively large area.

$MgAl_2O_4$ has a lattice constant of 8.083 Å, which is approximately twice as much of gold, 4.078 Å, resulting in a small mismatch of 0.89%; thus, the condition for Bragg Diffraction in gold lies very close to that of the substrate. Therefore, the pole figures compiled for the Au nanostructures, all have leak-through peaks from the $MgAl_2O_4$ substrate. To better visualize this, powder patterns of gold and magnesium aluminate spinel, which indicate all their allowed reflections, are overlapped and displayed in the intensity vs. 2θ plot in Figure 34. This figure illustrates the overlap of both (222) and (311) spinel reflections (pole figures), with gold's (111) pole figure.

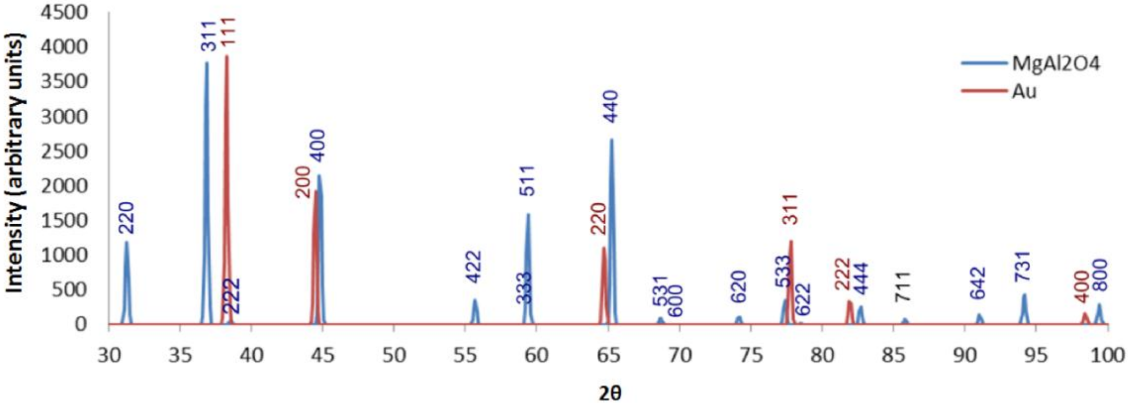

Figure 34: Overlapping powder patterns from $MgAl_2O_4$ and gold. All of gold's peaks overlap with magnesium aluminate spinel's peaks. The data for spinel and gold were obtained from references [36] and [72], through the ICSD data base for crystals, respectively.

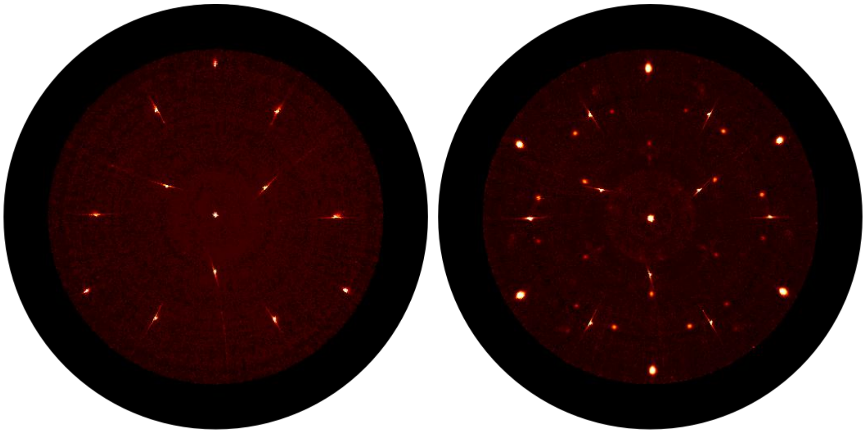

(a) **(b)**

Figure 35: Pole figures configured by integrating over a 2θ range of 38.0º to 38.6º, corresponding to the (111) pole figure of gold overlapping the (222) and (311) pole figures of spinel. These pole figures were configured from measurements done on (a) bare $MgAl_2O_4$ substrate, and (b) gold nanoparticles self-assembled above the $MgAl_2O_4$ necking structures. The substrate peaks shown in (a), also appear in (b).

Figure 35 illustrates pole figures corresponding to a bare $MgAl_2O_4$ substrate and a substrate having intricate Au-$MgAl_2O_4$ nanostructures self-assembled on it. These pole figures were both configured by integrating over a 2θ range of 38.0º to 38.6º, which corresponds to gold's (111) pole figure but overlaps magnesium aluminate's (222) and

(311) polefigures. Qualitative comparison of these two pole figures allows one to distinguish magnesium aluminate's leak-through peaks from those of gold, or identify where they overlap.

The preferred orientation of the gold nanoparticles were analyzed and confirmed by both the (111) and the (200) pole figures of gold, however, the (200) pole figures are not presented here. In order to visualize how the peaks in Figure 35 correspond to the various preferred orientations, the peaks are labeled in the model pole figure shown in Figure 36. To prevent clutter, only one in-plane orientation was selected from orientations that share a common plane parallel to the (111) surface of the substrate.

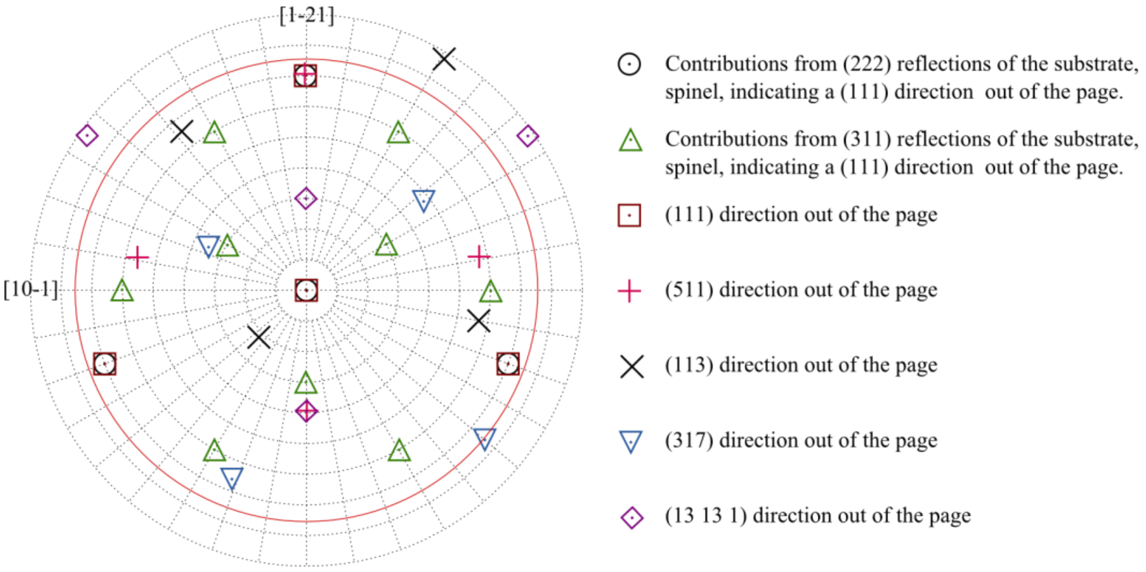

Figure 36: Labeling of the peaks present in a (111) pole figure corresponding to Au nanostructures self-assembled above the $MgAl_2O_4$ necking structures. The red solid line indicates the outer limit as to with data was collected. Beyond this line appears black in the pole figure.

The maximum intensity signals measured from the (111) pole figure in Figure 35 corresponds to the following orientations;

<111> Au || <111> $MgAl_2O_4$ with <10-1> Au || <10-1> $MgAl_2O_4$, and
<111> Au || <111> $MgAl_2O_4$ with <-101> Au || <10-1> $MgAl_2O_4$: 60° in-plane rotation.

The in-plane rotation is measured clockwise, with reference to the "12 O'Clock" position. The indicated orientations correspond to the six outer peaks, as well as the central peak, of the (111) pole figure of the gold nanoparticles shown in Figure 35 (b). By comparing the pole figure of the substrate to that of gold, one can see the existing overlap between them. As shown in Figure 36, the (222) reflections of $MgAl_2O_4$ overlap the (111) peaks of gold, illustrating the epitaxial alignment between the gold nanoparticles and the substrate. Here, the relative contributions of these peaks can be understood qualitatively, by comparing their brightness relative to other peaks of gold. The qualitative comparison shows that orientations corresponding to <111> Au || <111> $MgAl_2O_4$ are relatively brighter than all other peaks of gold. In section 3.3, these contributions are semi-quantitatively analyzed and the results verify that the indicated orientations do correspond to the maximum intensity peaks in the (111) pole figure of the gold nanoparticles. This may be best justified by the nominal lattice mismatch of 0.89% between Au and $MgAl_2O_4$. The small mismatch provides geometrical alignment between the lattice structure of gold and $MgAl_2O_4$, so that through the annealing process gold can re-organize and epitaxially self-assemble on the substrate. The well aligned lattice of gold with magnesium aluminate spinel, when <111> Au || <111> $MgAl_2O_4$ with <1-10> Au || <1-10> $MgAl_2O_4$, is shown in Figure 37. It is important to note, that this image is simply a schematic model to aid in visualizing the X-ray data and does not consider the presence of the interfacial layer that is created through the dewetting processes. The other orientations identified from the X-ray data may have other interpretations.

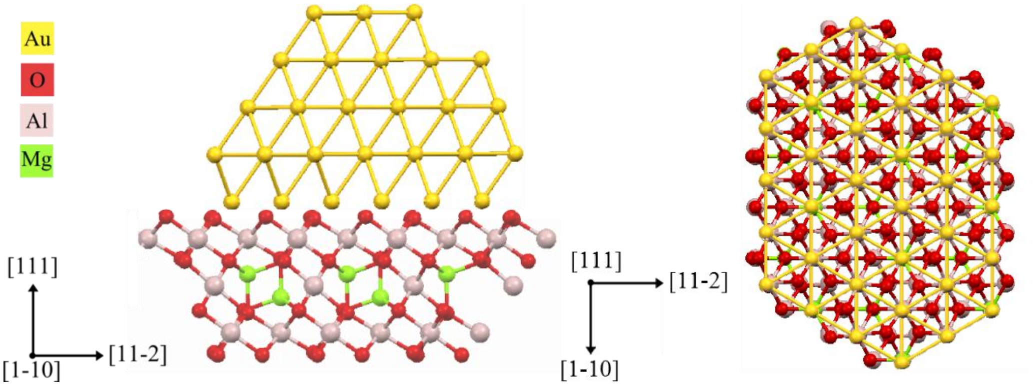

Figure 37: Visualization of <111> Au || <111> $MgAl_2O_4$. Note the the image to the right consists of only one monolayer of gold.

Other preferred orientations that contribute to the peaks seen in Figure 35 are:

<511> Au || <511> $MgAl_2O_4$, <0-11> Au || <10-1> $MgAl_2O_4$,
<511> Au || <511> $MgAl_2O_4$, <1-4-1> Au || <10-1> $MgAl_2O_4$: 60° in-plane rotation,
<511> Au || <511> $MgAl_2O_4$, <1-1-4> Au || <10-1> $MgAl_2O_4$: 120° in-plane rotation,
<511> Au || <511> $MgAl_2O_4$, <01-1> Au || <10-1> $MgAl_2O_4$: 180° in-plane rotation,
<511> Au || <511> $MgAl_2O_4$, <-141> Au || <10-1> $MgAl_2O_4$: 240° in-plane rotation,
<511> Au || <511> $MgAl_2O_4$, <-114> Au || <10-1> $MgAl_2O_4$: 300° in-plane rotation.

Minor contributions are also evident from:

<131> Au || < 111> $MgAl_2O_4$ at 45°, 165° and 285° in-plane rotations as well in-plane mirrored orientations at 75°, 95° and 315°.

<13 13 1> Au || <111> $MgAl_2O_4$ at 0°, 120° and 240° in-plane rotations and potential in-plane mirrored orientations at 60°, 180° and 300°.

<211> Au || <111> $MgAl_2O_4$ at 45°, 165° and 285° in-plane rotations and in-plane mirrored orientations at 75°, 95° and 315°.

<731> Au || <111> $MgAl_2O_4$ at 7.5°, 112.5°, 127.5°, 232.5°, 247.5°, 353.5° and 360° in-plane rotations.

The preferential crystallographic alignment of a crystalline film grown on a crystalline or amorphous substrate has been attributed to many phenomena including interface defects, interfacial energy, anisotropy in nucleation, and re-crystallization [20]. In the current system under study the identified preferred orientations, other than <111>Au || <111> $MgAl_2O_4$ with 0º in-plane rotation, can be interpreted as low energy twinning defects.

In the Au-$MgAl_2O_4$ system of study, the direct influence of both Au on $MgAl_2O_4$, and $MgAl_2O_4$ on Au is evident; the crystallographic structure of the substrate influences the self-assembly of the gold nanoparticles; they have specific preferred crystallographic orientations with respect to the substrate, while the presence of gold in the system leads to mass transport, and surface reconstruction of $MgAl_2O_4$. Small volumes of this noble metal significantly affect the $MgAl_2O_4$ surface, allowing it to reconstruct and form crystalline magnesium aluminate spinel necking structures, directly below the faceted gold nanoparticles. The formation of the intricately shaped Au-MgA_2O_4 nanostructures are sensitive to both annealing duration and annealing profile. The experimental conditions that were found to yield their self-assembly are summarized in Figure 38 .

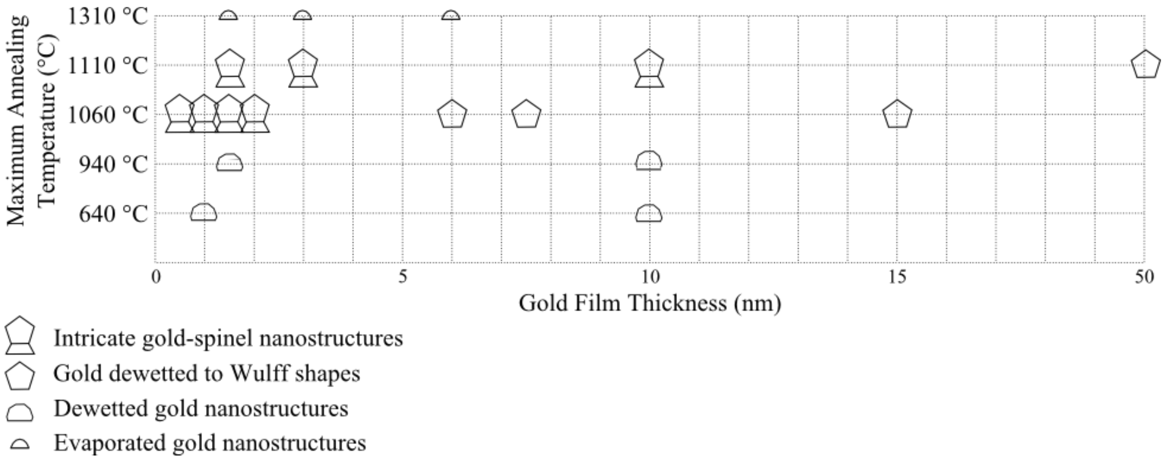

Figure 38: Experimental results summarizing the influence of annealing profile and gold film thickness on the self-assembly of the nanoparticles.

The experimental results corresponding to the investigation of annealing profile are provided in the following section.

3.2 Influence of the Annealing Profile

Varying the annealing profile in the system under study influences many features of the self-assembled structures. It affects the size, density, shape, and crystallographic orientation of the gold nanoparticles and it is correlated to the growth of the $MgAl_2O_4$ nanostructures. Higher annealing temperatures and increased annealing durations allow for the construction of prominent magnesium aluminate spinel nanostructures. However, exceeding temperatures and annealing times, ultimately result in drastic size reduction of the gold nanoparticles. Once again, in this case there is evidence of $MgAl_2O_4$ surface modification, however, instead of re-assembling to form tall necking structures below the gold particles, a flat pit forms in its vicinity.

The preceding work to this thesis, which sighted the self-assembly of intricate nanostructures on $MgAl_2O_4$ substrates, used gold films with an initial thickness of 5 Å, 10 Å, and 15 Å [1]. Therefore, these thicknesses were used as a starting point in continuing this study, with a focus on films of 15 Å since they contribute to larger particle sizes.

To investigate the influence of the heating profile, 15 Å of gold was deposited on $MgAl_2O_4$ substrates, and annealed following heat treatment 2 (940 °C), 3 (1060 °C) and 4 (1110 °C). Secondary electron images of these specimens are presented in Figure 39. It should be noted that since scanning electron microscopy was used as the dominant method for imaging the samples, and therefore the dominant method in dictating the presence of intricate Au-$MgAl_2O_4$ nanostructures, the conclusions made here are limited by the resolution of the particular system used for imaging, and the features hidden by the gold nanoparticles.

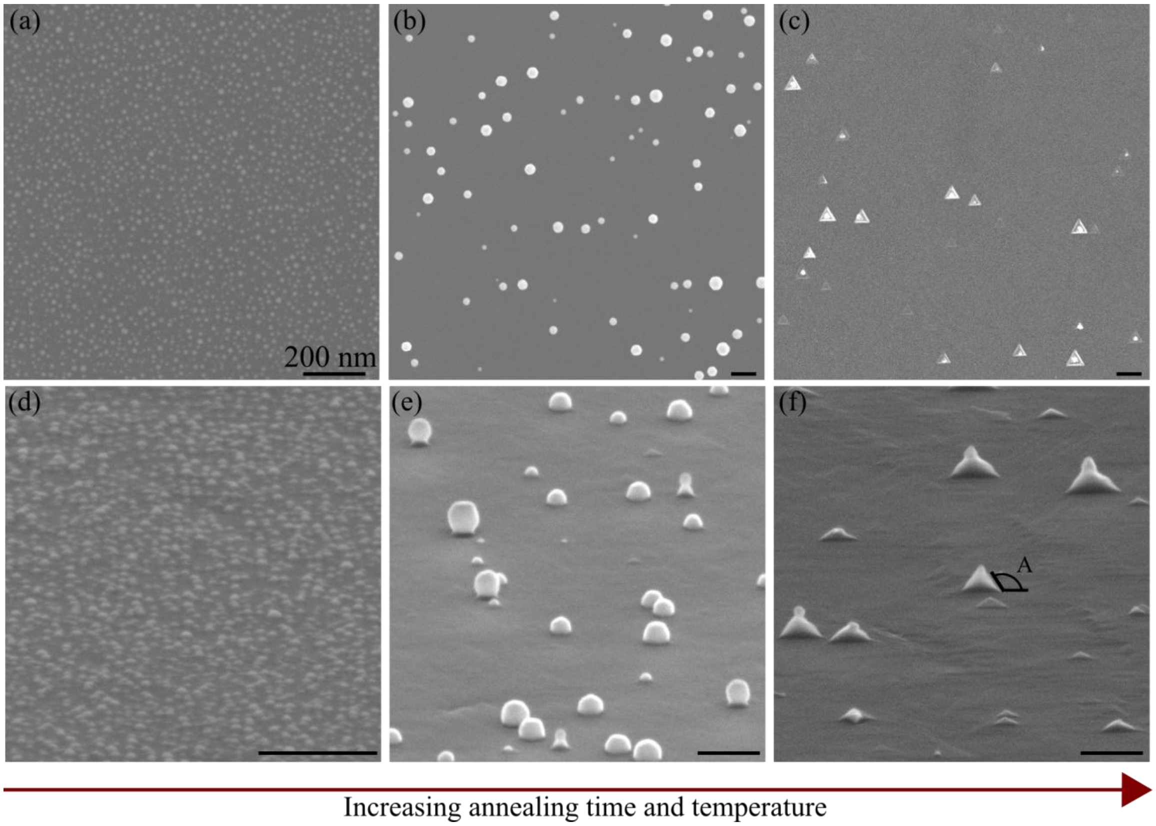

Figure 39: Scanning electron microscopy images of 15 Å of gold annealed following heat treatment 2, 940 °C, heat treatment 3, 1060 °C, and heat treatment 4, 1110 °C, shown in (a), (b) and (c) respectively. The top row corresponds to a projected top view, while the bottom row images were captured with the sample at 70° tilt. Scale bar is 200 nm.

The lower heat treatment, heat treatment 2 (940 °C in 1 hr), shows no distinct evidence of the presence of intricate Au-$MgAl_2O_4$ particles. Increasing the temperature to 1060 °C, heat treatment 3, for a prolonged duration, shows the development of the complex Au-$MgAl_2O_4$ nanostructures. Heat treatment 4, with even higher temperatures and soak times shows growth in both the base width and height of the $MgAl_2O_4$ nanostructures. Increasing heat temperatures and durations reduces the density of the gold nanoparticles, but not their size. The size of the gold nanoparticles initially increases with temperature, but then lessens. The initial increase in gold diameter may be attributed to Ostwald ripening or gold particle agglomeration. Whereas, the size reduction observed after prolonged exposure of the sample to high temperatures, may have been induced by evaporation of the particles, which causes mass-loss and therefore a reduction of their size. The gold nanoparticle density and size were measured in two to four different regions covering several micrometer squared surface areas, providing good statistics, which are presented in Table 2.

Table 2: Average gold nanoparticle density and size variation with annealing profile.

Heat Treatment	2: 940 °C for 0 hr	3: 1060 °C for 1.3 hr, 965 °C for 1 hr	4: 1110 °C for 1.5 hr, 965 °C for 2 hr
Average density (#/µm^2)	1511[a]	7[b]	3[c]
Au particle diameter (nm)[d]	14	80	28

Once $MgAl_2O_4$ self-assemblies develop, increasing temperature no longer appears to affect their structure, as in, they maintain their tetrahedron-like structure with a triangular footprint. In some cases, one or two corners may be faceted. The angle measured, counter clockwise, from the substrate to the necking structure, which is defined as angle A and is shown for one particle in Figure 39 (f), varied between 113^o to 150^o with an average value of 132^o. The lowest energy surfaces of $MgAl_2O_4$ are {100}, {110} and {111} with energies of 2.27 J/m^2, 2.85 J/m^2 and 3.07 J/m^2 respectively [38]. The corresponding angles between (-100), (-1-10) and (-1-11) planes with the (111) are 125.26°, 144.74°, and 109.47°. Comparing angles measured from SEM images to $MgAl_2O_4$ low energy surfaces, the {100} family of planes would best explain the surface planes of $MgAl_2O_4$ nanostructures. However, if instead, the contact angle measured from the TEM image, 110°, is chosen to represent the contact angle for all the $MgAl_2O_4$ nanostructures studied in this section, then, the {111} family of planes would best explain the surface planes of $MgAl_2O_4$ nanostructures. It may be possible that both {100} and {111} family of planes,

---

[a] Au nanoparticle density and diameter was measured in two different regions, covering a total area of 6

[b] Au nanoparticle density and diameter was measured in three different regions, covering a total area of 512 µm^2.

[c] Au nanoparticle density was measured in three different regions, covering a total area of 232 µm^2.

[d] In most cases this value was measured as the largest distance between two points of the projected particle image.

and perhaps even {110} family of planes, all participate in forming the surfaces of various $MgAl_2O_4$ nanostructures.

High resolution, low voltage scanning electron images obtained with the Magellan, Figure 30, suggest that once the intricate Au-$MgAl_2O_4$ structures appear, all other dewetted gold particles have some, however minute, necking structure beneath them. At the discussed thickness of 15 Å, heat treatment 3 seems to be on the border of requirements for where the Au-$MgAl_2O_4$ complex structures form, as this profile showed significant sensitivity to annealing temperature and profile, as well as, the necking structures are not as distinct and as clearly identified among many particles.

Using the same initial conditions, such as the thickness of the gold films, increasing annealing temperature and duration lead to greater amounts of $MgAl_2O_4$ mass transport, corresponding to larger self-assembled crystalline nanostructures beneath dewetted gold nanoparticles. In the meantime, at sufficiently high temperatures the volume of the gold nanoparticles decreases, which suggests their evaporation. This may be attributed to the correlation of saturated pressure to temperature; increasing temperature will increase the saturated vapor pressure of gold, and therefore promotes evaporation from the surface of the gold nanoparticles [20]. As the gold nanoparticles evaporate, their radius decreases, and therefore their vapor pressure heightens, which further promote evaporation. In fact, when increasing annealing temperature to 1310 °C, following heat treatment 5, which involves faster heating rates, and longer annealing durations, the gold nanoparticles drastically diminish in size, and there is no sign of $MgAl_2O_4$ nanostructures. However, there is distinct surface modification in the vicinity of the miniscule gold nanoparticles in the form of pseudo-flat pits. They are unlike any surface modification seen post annealing of magnesium aluminate spinel, with or without gold. The gold particles are indicated with red arrows in Figure 40 to help identify them and their surrounding pits.

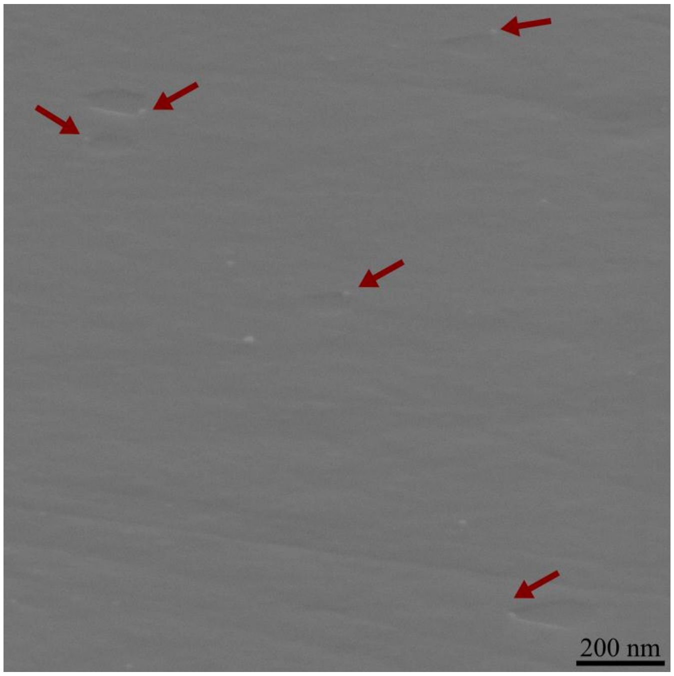

Figure 40: 15 Å of gold annealed following heat treatment 5 (1310 °C). The red arrows are directed towards gold nanoparticles with distinct surface modification in their vicinity.

A similar heat treatment investigation, consisting of treatments 1 (640 ºC), 2 (940 ºC) and 4 (1110 ºC) was done on samples prepared with an initial film thickness of 10 nm. Selecting a thicker film, allows for more clear secondary electron imaging of the nanoparticles, as well, the wider range of energies that are covered with these heat treatments, better show the orientation development, from earlier stages of dewetting to the formation of complex Au-$MgAl_2O_4$ nanoparticles. Figure 41 shows the self-assembled Au and Au-$MgAl_2O_4$ nanostructures. Their corresponding pole figures are illustrated in Figure 42.

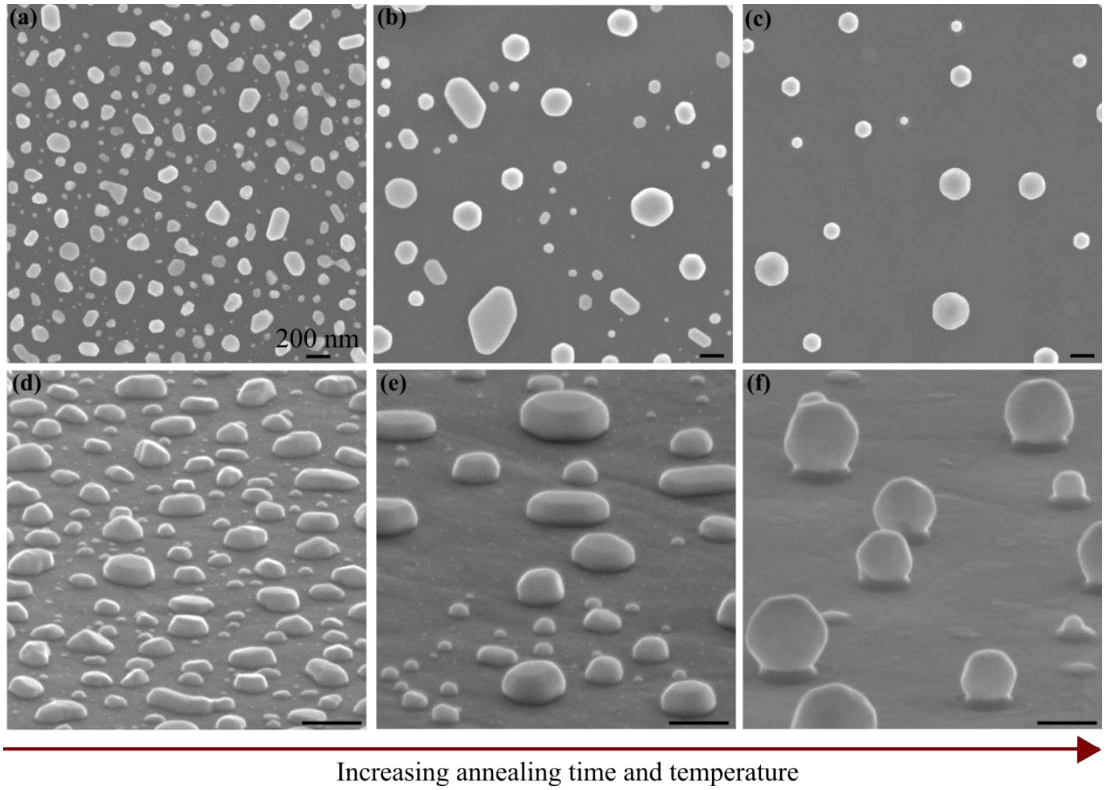

Figure 41: SEM Images of 10 nm gold films annealed following (a) heat treatment 1, 640 ºC, (b) heat treatment 2, 940 ºC, and (c) heat treatment 4, 1110 ºC, in (c). The top row corresponds to top view images, while the bottom row shows images of samples at a 70° tilt. The scale bar is 200 nm.

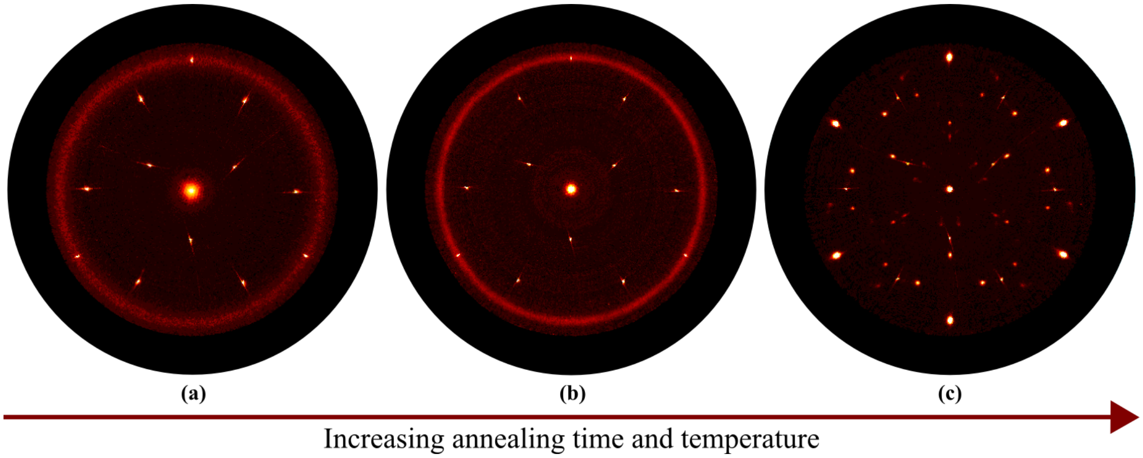

Figure 42: (111) pole figures conducted on 10 nm gold films annealed on magnesium aluminate substrates following (a) heat treatment 1 (640 °C), (b) heat treatment 2 (940 °C), and (c) heat treatment 4 (1110 °C).

2DXRD texture analyses of these samples show dewetted gold particles begin developing a crystallographic alignment with the magnesium aluminate substrate lattice at temperatures as low as 640 °C, when annealed by heat treatment 1. Figure 42 (a) illustrates a <111> Au || <111> $MgAl_2O_4$ preferred orientation with a random in-plane orientation distribution. The presence of <111> Au peaks at lower temperatures show that it requires lesser energy to form and is therefore more favorable. This is not surprising, as the {111} family of planes contribute to the most close-packed and lowest energy planes of gold [22]. By comparing the <111> peaks of gold for this sample, annealed by heat treatment 1, 640 °C, particularly its central peak, with the samples annealed by heat treatments 2, 940 °C, and heat treatment 4, 1110 °C, one can easily observe that the broadening of the peak in the radial direction reduces with increasing temperature. The radial broadening indicates a distribution of orientations that lie close to the <111> orientation but do not perfectly align, creating a mosaic crystal structure. Therefore as temperature increases, the radial broadening will decrease, and the gold nanoparticles will become more uniform in crystallographic orientation. The secondary electron images illustrated in Figure 41 (a) and (d), for this sample, show the dewetted gold particles have a wide range of shapes agreeing with the lesser ordering seen in its corresponding pole figures.

Applying heat treatment 2, 940 °C, the gold nanoparticles have still not developed a preferred in-plane rotational direction as shown in Figure 42 (b). However, there is a noticeable reduction in radial broadening, indicating a higher degree of alignment between the <111> Au and <111> $MgAl_2O_4$ crystallographic planes which is expected with the increased energy provided to the system by heightening the annealing temperature. The improved organization of the gold nanoparticles are also seen in their secondary electron images. Figure 41 (b) and (e) illustrates the corresponding SEM images for this sample. Qualitative comparison of several SEM images obtained from this sample, to those obtained from the sample heated to 640 °C show a reduction in shape variation among the gold nanoparticles. That is, the higher temperature promotes more of the nanoparticles to rearrange and form lower energy structures.

Finally, using heat treatment 4 the system acquires sufficient energy to form equilibrium shaped Au-$MgAl_2O_4$ nanocrystals with a small distribution in size and shape. The relatively high order present in these structures can also be seen in their corresponding pole figures, Figure 42 (c). They present a significant amount of order and epitaxial alignment, which is not present in pole figures of particles annealed at shorter intervals to temperatures below the melting temperature of gold. The detailed preferred orientation analysis of a similar pole figure was presented in section 3.1. Qualitative comparisons of the peaks suggest that epitaxial alignment between the gold nanoparticles and the $MgAl_2O_4$ substrate correspond to the dominant preferred orientation. This includes contributions from both the <111> Au || <111> $MgAl_2O_4$ with <10-1> Au || <10-1> $MgAl_2O_4$ orientation, and a 60° rotation of this orientation. Semi-quantitative analysis presented in section 3.3 agrees with the dominance of these orientations.

Heat treatments play a critical role in promoting the self-assembly of intricate Au-$MgAl_2O_4$ nanostructures. The current experiments suggest annealing temperatures near, and exceeding the melting temperature of gold, held for durations over 0.5 hrs, then cooled below the melting temperature of gold, and soaked for one hour prior to the final cool down stage, result in the creation of the complex nanostructures. In the current study, mostly two stage heating profiles were employed, similar to that suggested by Devenyi et al [1]. However, more experiments could be done to indicate if an actual correlation exists between the two stage temperature profiles, and the creation of the intricate nanoparticles. At the higher end of the experimented annealing spectrum, elevating the temperature to 1310 °C and annealing at higher rates, resulted in the diminishing size of gold nanoparticles with no evidence of the $MgAl_2O_4$ nanostructure self-assemblies. At the lower end of the annealing spectrum, at temperatures near half the melting point of gold, gold nanoparticles start to preferentially organize such that <111> Au || <111> $MgAl_2O_4$. At this point, they do not have sufficient mobility to epitaxially align with the substrate, and therefore have a random in-plane orientation distribution. With increased temperature and annealing time, alignment evolved to more specific orientations with epitaxial alignment between Au and $MgAl_2O_4$ being the dominant preferred orientation.

3.3 Influence of the Gold Film Thickness

In the previous section heat treatments 3, 1060 ºC, and heat treatment 4, 1110 ºC, having higher annealing temperatures and longer soak times, led to the evolution of intricate Au-$MgAl_2O_4$ nanocrystals. These structures were more prominent when annealed by heat treatment 4, 1110 ºC, thus the primary investigation on the role of thickness, will be done using this heat treatment, however, the results from heat treatment 3 are briefly touched upon. The secondary investigation on the role of thickness of the gold overlayer was done for heat treatment 2, 940 ºC. The results show that the thickness of the gold overlayer affects the size, structure, and contribution from various crystallographic preferred orientations, of the Au-$MgAl_2O_4$ nanostructures.

Heat treatment 4, 1110 ºC, was applied to a sample with no gold deposited on it, and others having a gold film with thicknesses of 1.5 nm, 3 nm, 10 nm, and 50 nm. Secondary electron imaging with samples at 0º, and 70º tilt was mainly used to obtain topographic and morphological information from the nanostructures. However, AFM was applied when topographic features were on the order of, or smaller than the resolving power of the microscope. This was the case for $MgAl_2O_4$ substrates that were annealed in the absence of gold. The results are presented in Figure 43.

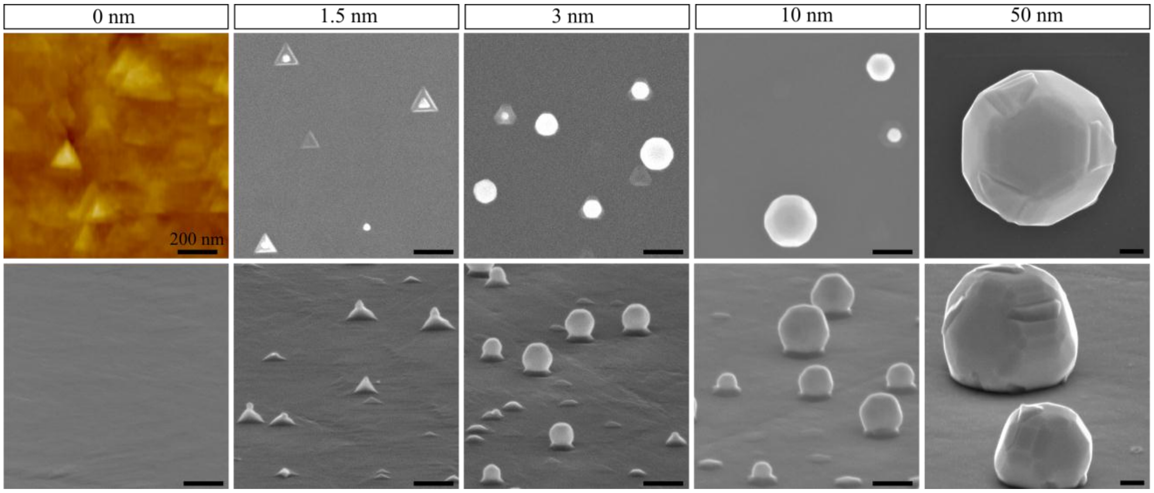

Figure 43: SEM/AFM images of $MgAl_2O_4$ substrates annealed, following heat treatment 4, 1110 ºC, with various starting thickness of gold as indicated in the image. Top row and bottom row images were taken with samples at a 0º, and 70º tilt, respectively. AFM imaging was only used in place of SEM to distinguish main topographical features not prominent by SE imaging. The scale bar is 200 nm.

The bare magnesium aluminate substrates have flat triangular features with the same alignment as those seen when annealing substrates with 1.5 nm of gold deposited on them. As discussed in section 3.1, these features are not present prior to annealing, and thus indicate surface reorganization to lower energy structures. Depositing a 1.5 nm gold film prior to annealing appeared to enhance $MgAl_2O_4$ surface instability and provide a method for larger mass transport in contribution to the self-assembly of single crystal $MgAl_2O_4$ nanocrystals. As the initial film thickness increased, the size of the gold nanoparticles became larger. On average, the base footprint also appeared to become larger, and to a first order approximation the total volume of mass transported from the surface, to form the $MgAl_2O_4$ crystalline nanostructures, also increased with gold thickness. However, there is an apparent upper limit to the enhanced growth of the $MgAl_2O_4$ nanostructures, since when using a 50 nm gold film, the presence of the $MgAl_2O_4$ nanostructures are no longer distinguishable beneath most gold nanoparticles imaged in the SEM. Measurements from gold nanoparticle density and size are in Table 3.

Table 3: Average gold nanoparticle density and size variation with thickness.

Initial gold film Thickness	1.5 nm	3 nm	10 nm	50 nm
Density (#/µm^2)	3[e]	3[f]	2[g]	1E-1[h]
Au particle diameter (nm)[i]	28	129	212	865

When the thickness of the gold film is increased to 50 nm, the presence of the magnesium aluminate nanostructures was significantly suppressed. They were very rarely seen, and were only sighted below smaller gold nanostructures having a diameter between 192 nm to 233 nm, which is much smaller than the average size of these particles, 865 nm. Such a trend was also seen when investigating the role of thickness for samples prepared by heat treatment 3, 1060 ºC. This heat treatment resulted in the self-assembly of magnesium aluminate nanostructures, for samples prepared with a gold film having a thickness of 2 nm or less, but were no longer apparent for thicknesses exceeding 6 nm. Therefore, in applying both heat treatments, there is an apparent upper bound for thickness at which the presence of the $MgAl_2O_4$ nanostructures becomes indistinguishable by SE imaging. However, the upper bound is very different in the two systems. It is higher in heat treatment 4, which includes higher annealing temperature, and longer annealing durations. Another distinguishing factor of the gold nanostructures prepared with a 50 nm thick gold film, is that they exhibited surface protuberance faceting features. The faceted protuberances suggest that creating more surface, reduces the total energy of the gold nanoparticle. This may be attributed to the increased number of defects with larger particle size. It is energetically more probable to grow smaller structures with lesser defects compared to bigger structures.

---

[e] Au density measured from three different regions, covering a total area of 232 µm^2.
[f] Au density and diameter measured from three different regions, covering a total area of 336 µm^2.
[g] Au density and diameter measured from four different regions, covering a total area of 542 µm^2. Density of magnesium aluminate necking structures with no gold particles atop were also taken into account.
[h] Au density and diameter measured from four different regions, covering a total area of 43,453 µm^2.
[i] In most cases this value was measured as the largest distance between two points of the projected particle.

Another important variation witnessed with changing thickness, is the evolution of $MgAl_2O_4$ structure shape. Figure 44 more clearly presents this concept; increasing the initial thickness of gold affects the shape of the interface between the $MgAl_2O_4$ nanostructures and the substrate. A 1.5 nm gold film promotes the self-assembly of $MgAl_2O_4$ nanostructures that mostly have a triangular footprint. As the film thickness increases to 3 nm, the number of facets increase, but the newly formed facets have a lesser contribution to the circumference of the footprint. At 10 nm the contribution from all facets become approximately the same.

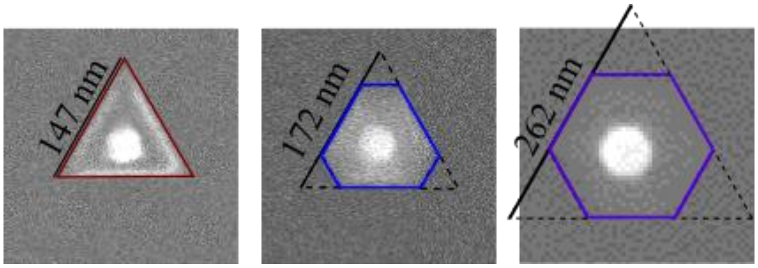

Figure 44: Evolution of $MgAl_2O_4$ nanostructure shapes with increased gold thickness. The footprints evolve from triangular, to faceted triangles, to hexagons. An equilateral triangle, and a measurement of its side length, is fitted to every shape as a means of comparison.

At smaller sizes, the Wulff construction does not always succeed in explaining the minimum surface energy construction of a particle. This is because at smaller scales the energy to form an edge becomes comparable to the energy savings achieved from having a low energy facet [15]. This may explain why fewer facets are present for the smallest $MgAl_2O_4$ nanostructures. In Figure 44 a triangle is fit to all three structures formed by the three different thicknesses of gold, 1.5 nm, 3 nm and 10 nm. As the thickness of gold increases, so does the fitted triangle. The triangles fitted to the structures having five facets are larger than three-facet triangle. This may be indicative that for triangles with a perimeter exceeding some minimum threshold, it becomes more energetically favorable to form a new edge and a lower energy facet.

The error in measurements inherent to measuring the contact angle of the $MgAl_2O_4$ nanostructures from a secondary electron image, make it difficult to identify the corresponding $MgAl_2O_4$ surface planes for every existing facet. However, based on the footprint shape, the {100} and {111} planes of $MgAl_2O_4$, which correspond to low energy surfaces of $MgAl_2O_4$, may best describe the present structures.

Variation in thickness for samples prepared by heat treatment 4, 1110 ºC, was further characterized using 2DXRD textures analysis. The size categories for the gold overlayer thickness remain the same; 1.5 nm, 3 nm, 10 nm and 50 nm. The volume/size of gold nanoparticles self-assembled from 1.5 nm gold films were very small, resulting in minimal, to no X-ray signal collection. Thus, the X-ray data from that sample was omitted. The (111) pole figures of gold, for the remaining thickness categories, 3 nm, 10 nm, and 50 nm thick films of gold, are presented in Figure 45. The preferred orientations identified remain constant regardless of the initial thickness of the gold film, however, the relative contribution of each orientation to the total signal collected from gold varies. Semi-quantitative analysis of the maximum peak intensities was performed following the procedure explained in section 2.4.3.2. The results indicate that epitaxial alignment of the gold nanoparticles with the magnesium aluminate substrate are stronger for samples prepared with thinner films of gold, and become progressively worse with increased thickness. The contributions of the various preferred orientations are indicated in Table 4.

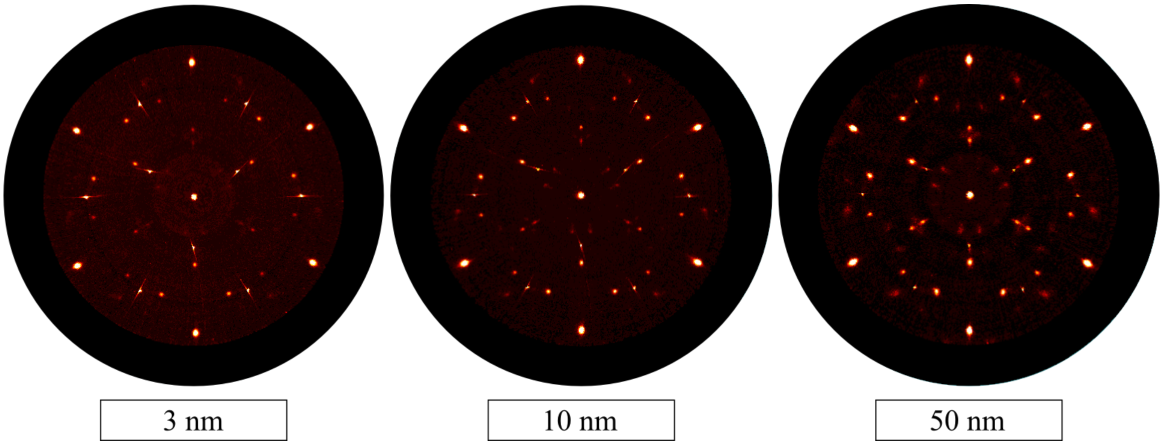

Figure 45: (111) pole figures from gold nanoparticles dewetted following heat treatment 4, 1110 ºC, with various starting film thicknesses of gold as indicated in the image.

Table 4: Semi-quantitative analysis of (111) pole figures of gold nanoparticles dewetted following heat treatment 4, 1110 ºC, with various starting film thicknesses of gold as indicated in the table.

Initial gold film thickness	3 nm	10 nm	50 nm
<111> Au ‖ <111> $MgAl_2O_4$ with <10-1> Au ‖ <10-1> $MgAl_2O_4$: 0º in-plane rotation	67 %	49 %	40 %
<111> Au ‖ <111> $MgAl_2O_4$ for 60º in-plane rotation	18 %	34 %	42 %
<511> Au ‖ <111> $MgAl_2O_4$ for all in-plane rotations	9 %	12 %	10 %
Other	6 %	5 %	8 %
Total Au/$MgAl_2O_4$ signal	6 %	19 %	60 %

The results presented in this section thus far, investigated the role of thickness when preparing samples by heat treatment 4. Studying the texture of dewetted gold films, with different thicknesses, at a lower annealing temperature, 940 ºC, prepared by heat treatment 2, show a rather different trend in their crystallographic organization. The pole figures show different stages of crystallographic organization, depending on film thickness, for the same applied heating profile. Dewetting reports [13] have indicated that dewetting temperature is a function of film thickness; greater film thicknesses require higher temperatures to initiate dewetting. The later development of dewetted particles as a function of temperature seems to also have led to a later evolvement of the crystallographic alignment between the gold particles and the $MgAl_2O_4$ substrate. This was understood by comparing the pole figures of two films, one with an initial thickness of 1.5 nm and the other 10 nm, both annealed to 940 ºC, following heat treatment 2. The results are presented in Figure 46.

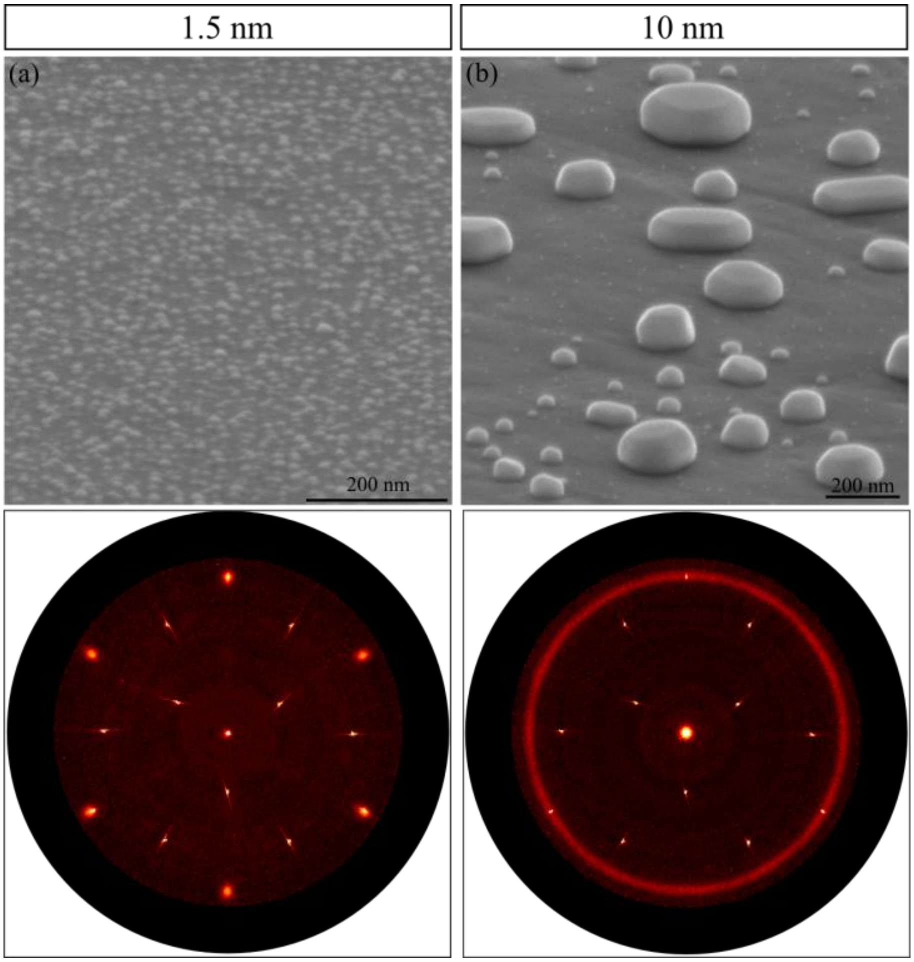

Figure 46: SEM images and (111) pole figures of gold nanoparticles; the nanoparticles were prepared by depositing a gold film of 1.5 nm in (a), and 10 nm in (b), and annealing both following heat treatment 2, 940 ºC. SEM images were taken from substrates at 70º tilt.

Applying heat treatment 2, 940 ºC, to 1.5 nm films allowed for relatively well organized gold nanoparticles to self-assemble with distinct orientations and in-plane rotations; <111> Au || <111> $MgAl_2O_4$ with a 0º and 60º in-plane-rotation as well as a faint signal from the <511> orientations are present. The thicker film, 10 nm, exhibits <111> Au || <111> $MgAl_2O_4$ with random in-plane orientation and greater radial broadening. Secondary electron imaging of the nanoparticles, also present a smaller range of shape variation in particles dewetted from thinner films, agreeing with trends found from XRD measurements. The 1.5 nm film of gold dewets to gold nanoparticles with an average size of 14 nm and a standard deviation of 5 nm measured over ~ 9000 particles. In fact, the excessively small size of the gold nanoparticles may be correlated to their enhanced crystallographic alignment with the substrate. Since most of the gold nanoparticles have a size in the range of 9 nm to 19 nm, they have significantly lower melting temperatures compared to bulk. As it turns out, in this size range, the melting temperature of gold is approximately between 930 ºC - 1020 ºC [24], which encompasses the temperature at which these samples were heated to. This means, when starting with a 1.5 nm film of gold, some portion of the nanoparticles become molten when heated to 940 ºC, because of their sufficiently small size. Perhaps, the molten or near molten gold nanoparticles have sufficient mobility to crystallographically rearrange, to obtain a lower energy structure and epitaxially align with the substrate. STEM-HAADF images shown in Figure 47 (b) may better illustrate the relative uniformity in the shape of these structures. Alternatively, when starting with an initial film thickness of 10 nm, the dewetted gold nanoparticles are much larger and have the same melting temperature as bulk gold. When heated to 940 ºC, they do not have sufficient mobility to form lower energy structures, and therefore exhibit more variation in their crystallographic arrangement.

As indicated earlier, STEM was used to further evaluate the gold nanoparticles self-assembled through annealing 1.5 nm Au by heat treatment 2, 940 ºC. Since the sizes of the gold nanoparticles are small, they overlap within the thickness of the TEM specimen. Figure 47 (a) corresponds to two overlapping nanoparticles. Focusing on the boundary between the Au nanoparticles and the $MgAl_2O_4$ substrate, the presence of an interfacial boundary is not evident.

There may be a correlation between the formation of a distinct interfacial boundary between Au and $MgAl_2O_4$, and the growth of the crystalline $MgAl_2O_4$ nanostructures. It is possible that higher annealing temperatures, and durations, allow for this interface to form, which may significantly reduce the interfacial energy between gold and magnesium aluminate spinel, so that the substrate material diffuses towards this interfacial layer.

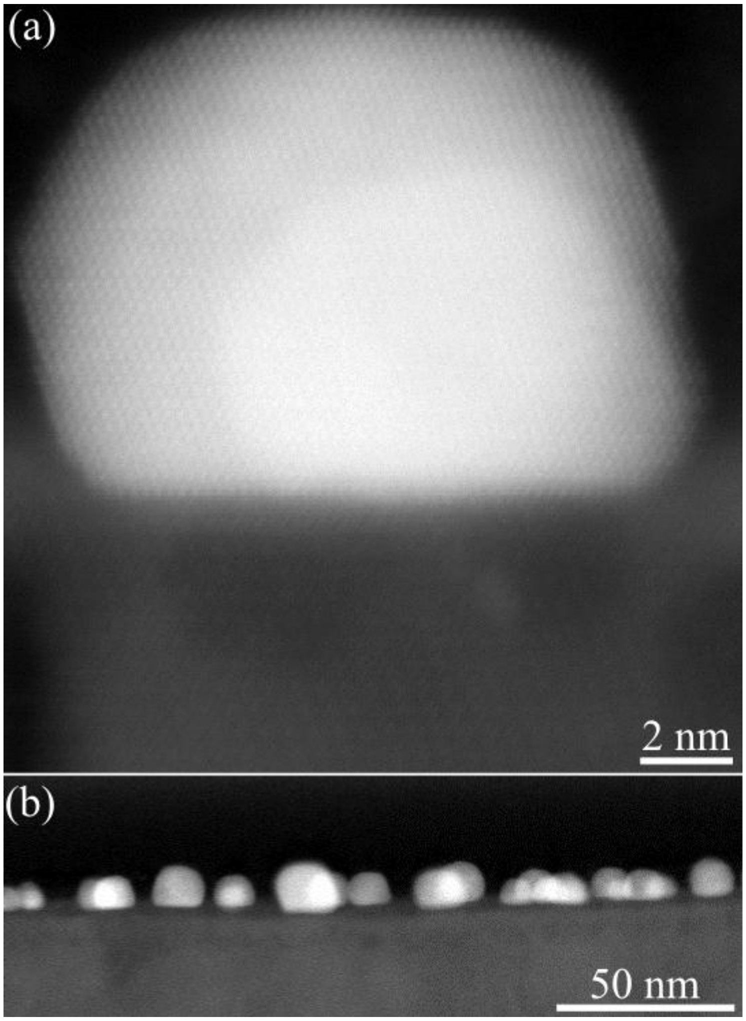

Figure 47: STEM-HAADF images of gold nanoparticles dewetted from a 1.5 nm gold film on (111) $MgAl_2O_4$, annealed to 940 °C, following heat treatment 2. (a) High resolution STEM image corresponding to a single gold nanoparticle. A distinct interfacial boundary layer is not evident. The overlapping signal from a secondary smaller gold nanoparticle is evident within the bigger primary particle. (b) Low magnification STEM image. The gold nanoparticles are relatively uniform in both size and shape.

3.4 Combined Effect of Heating Profile and the Gold Film Thickness

After combining the results related to the influence of annealing profile, and thickness of the gold overlayer, some trends are suggested:

First, preliminary quantitative measurements suggest that for a given heat treatment, thicker films of gold yield larger particles, and larger gold particles correlate to wider base widths and potentially smaller heights of $MgAl_2O_4$ nanostructures. These measurements are presented in Figure 48. Since the rate of growth of base width is higher than the diminishing rate of base height, increasing gold film thickness, to a first order approximation, increases $MgAl_2O_4$ mass transport which contributes to the formation of $MgAl_2O_4$ crystalline nanostructures self-assembled below the dewetted gold nanoparticles. As described in the previous section, this trend does not continue indefinitely and has an upper bound.

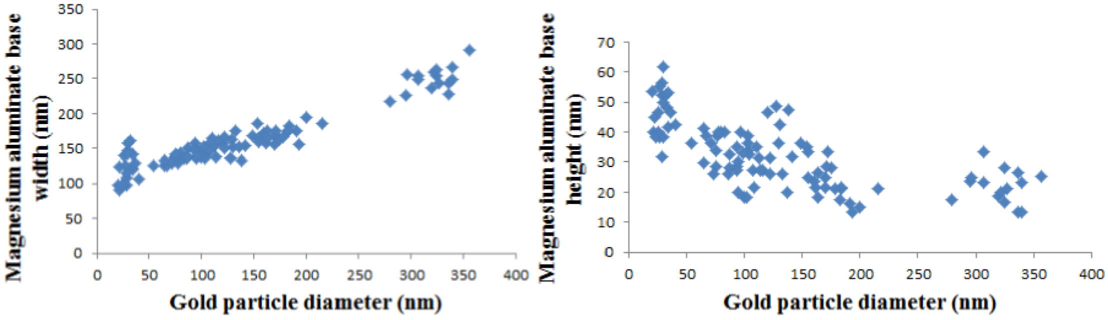

Figure 48: Gold particle size relation to the base width and height of $MgAl_2O_4$ nanostructures self-assembled through heat treatment 4, 1110 °C.[j]

Secondly, with increasing annealing time and temperature, there are increases to $MgAl_2O_4$ mass transport and hence the size of the $MgAl_2O_4$ necking structures. The limiting factor in this case is understood to be from the evaporation of gold nanoparticles at higher temperatures.

Thirdly, the contact angle of the $MgAl_2O_4$ nanostructure with the substrate surface is constant within the error of the measurement. Preliminary measurements made to

---

[j] These measurements were done using SEM images taken from samples at a 70° tilt, and therefore the measured heights required tilt correction. Here, a first order approximation was used to correct for the height of the $MgAl_2O_4$ nanostructures. Their structure was simplified as a one dimensional rod, therefore the corrected height was approximated as: measured height/sin(70°). As well, when the particle is at a 70 degree tilt, the size of the gold nanoparticle on the $MgAl_2O_4$ necking structure, affects the 2D projected image that is captured, as it hides part of the necking structure. Bigger gold nanoparticles, hide a bigger portion of the necking structure. This was not taken into account in the first order approximation.

correlate the $MgAl_2O_4$ base width and height with contact angle, indicated no relationship between them.

Based on these conclusions, one would expect that within the suggested limits for thickness and temperature, combining thicker films with higher annealing temperatures, for longer durations, would result in larger $MgAl_2O_4$ self-assemblies. In fact, this has been observed. Figure 49 compares a 1.5 nm gold film annealed by heat treatment 3, 1060 ºC, to a 10 nm gold film annealed by heat treatment 4, 1110 ºC.

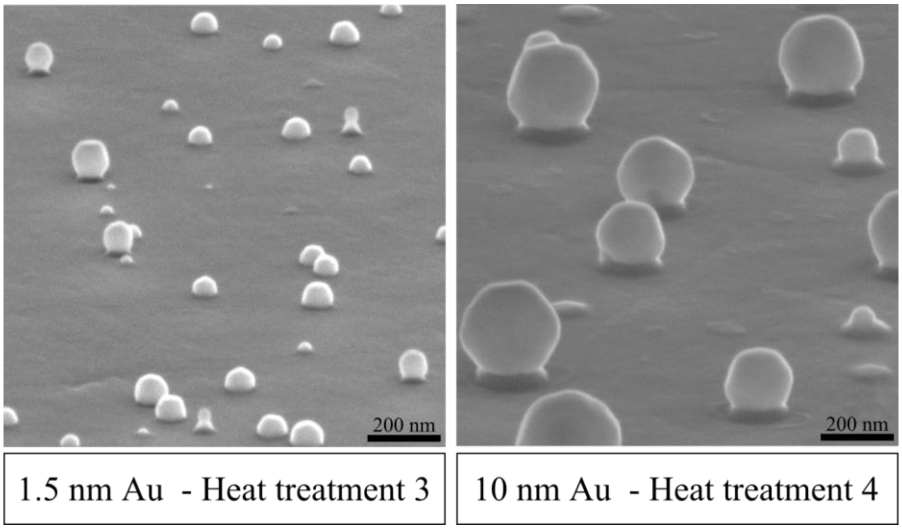

Figure 49: SEM images showing the effect of increasing the gold film thickness, annealing temperature, and soak durations, in the growth of $MgAl_2O_4$ nanostrucutres self-assembled below the gold nanoparticles. Left image: 1.5 nm of gold deposited on (111) $MgAl_2O_4$ substrates and annealed following heat treatment 3; heated to 1060 °C in 80 minutes. Held there for 25 minutes. Cooled to 965 °C in 0.5 hrs and held there for 1 hr. Right image: 10 nm of gold deposited on (111) $MgAl_2O_4$ substrates and annealed by heat treatment 4; heated to 1110 °C in 1.5 hrs. Held there for 1.5 hrs. Cooled to 965 °C in 0.5 hours and held there for 2 hrs. In both cases, samples were cooled to 30 °C over 14 hrs.

Fourthly, the development of in-plane texture of the gold nanoparticles, dominated by the epitaxial alignment between the gold nanoparticles and $MgAl_2O_4$ substrate, may be attributed to gold nanoparticles that are near or above their melting temperature. The results presented in this chapter suggest that all gold nanoparticles that are heated to 1060 ºC, by heat treatment 3, or 1110 ºC, by heat treatment 4, exhibit finite preferred orientations, with epitaxial alignment between the gold nanoparticles and the magnesium aluminate substrate contributing to a significant portion of the measured maximum intensity signal. Gold nanoparticles with sizes averaging at 14 nm, have a corresponding average melting point of 982 ºC. When annealed to 940 ºC, their pole figures exhibit in-plane texture, with the strongest peaks corresponding to the epitaxial alignment between gold and the substrate. However, the same heat treatment applied to nanoparticles that are an order of magnitude larger, and therefore have melting temperatures approaching that of bulk gold, exhibited a <111> preferred orientation with an infinite number of random in-plane orientations, when heated to 940 ºC, by the same heat treatment, 2.

Fifthly, when the $MgAl_2O_4$ necking structures are clearly observed by SEM, the corresponding gold nanoparticles had all developed in-plane texture and share, at minimum, the orientations of <111> Au || <111> $MgAl_2O_4$ and <511> Au || <111> $MgAl_2O_4$. As well, STEM images of these intricate Au-$MgAl_2O_4$ nanostructures suggested the presence of a distinct interfacial boundary separating Au from $MgAl_2O_4$. However, the reverse of this did not hold. If the specific orientations are measured from the gold nanoparticles supported on the substrate, or if the interfacial boundary is evident by STEM, then the $MgAl_2O_4$ nanocrystalline structures may not necessarily be evident.

The fourth and fifth observations may indicate that the crystalline $MgAl_2O_4$ nanostructures become apparent when the gold nanoparticles melt, and develop in-plane texture, with epitaxial alignment between the gold nanoparticles and the $MgAl_2O_4$ substrate being the dominant preferred orientation.

3.5 Discussion on the Au-assisted Self-assembly of $MgAl_2O_4$ Nanostructures

The mechanisms involved in the self-assembly of the $MgAl_2O_4$ nanostructures are not entirely clear. Based on the data presented, some potential methods are suggested and discussed.

One hypothesis is that mass transport of $MgAl_2O_4$ may take place earlier on in the dewetting process, when the gold nanoparticles are smaller. If at that stage the gold particles are roughly 10 nm, then they can exhibit strong catalytic activity. This may initiate mass transport of the $MgAl_2O_4$ substrate surface, either by creating an alloy with Au, or by solid state diffusion to the vicinity of the Au nanoparticles. At this point, the mass transport would not be readily visible through SE imaging. The STEM image presented in Figure 47 (b) may show some sign of such mass transport. The gold nanoparticles in this image are sufficiently small, therefore they can exhibit catalytic activity. Close observation of this image suggests that the interface of the gold nanoparticles with the substrate, are not aligned. The misalignment in the vertical axis may be justified by tilt of the TEM specimen, however, the fine misalignments in the horizontal axis cannot be justified in the same way. Those misalignments may correspond to the substrate material building up beneath the small particles. The SE image corresponding to this sample, Figure 46 (a), does not readily show these features.

Increasing the annealing temperature and duration may lead to both Ostwald ripening and agglomeration of the gold nanoparticles. If the gold nanoparticles agglomerate, then it may be that through this process, they also transport the $MgAl_2O_4$ material that had earlier been associated with them. Therefore, as the temperature increases, and the particles become bigger, more $MgAl_2O_4$ is associated with the gold nanoparticles. If $MgAl_2O_4$ had been associated with a gold nanoparticle by diffusing to its vicinity, then the structure would get larger in the heating processes, as gold nanoparticles agglomerate. However, if it had formed an unstable alloy during the heating process, then in the cool down stage, $MgAl_2O_4$ may phase separate and nucleate at the substrate interface, and form the crystalline necking structures.

This description would provide an explanation for the thickness and temperature dependence of the $MgAl_2O_4$ nanostructures; thicker films correlate to larger gold particles, and therefore may not exhibit strong catalytic activity, which would explain the upper limit observed for the gold film thickness that corresponds to the self-assembly of

$MgAl_2O_4$ necking structures. Since the mass transport of $MgAl_2O_4$ increases with gold particle agglomeration, and therefore with temperature, a certain temperature would be required to make the mass transport significant enough so that it would be distinguishable by SE imaging. However, this hypothesis, does not explain why the upper limit for the gold film thickness varies based on the applied heating profile. Further experiments described in Chapter 5, can be done, to potentially provide more support for this hypothesis. Although, the detailed method by which the Au and $MgAl_2O_4$ interact would continue to remain ambiguous.

A secondary hypothesis relies on solid-state diffusion of the $MgAl_2O_4$ substrate surface. The results presented suggest that as temperature increases, the gold film dewets, and forms nanoparticles. The nanoparticles begin to align in the <111> Au || <111> $MgAl_2O_4$ direction with random in-plane orientation. As temperature increases, the gold nanoparticles gain sufficient mobility to crystallographically restructure to form low energy epitaxially aligned gold nanoparticle, and lock into a favorable low energy state. It is suggested that further energy provided to the nanoparticles, is consumed by creating a low energy interfacial boundary. The low energy boundary may promote solid-state diffusion of the surrounding material, beneath the gold nanoparticles, forming the evident necking structures. This hypothesis is consistent with the fourth and fifth observations described in section 3.4. The proposed method could imply that as the $MgAl_2O_4$ necking structures diffuse towards the gold nanoparticles, they would leave depressions behind, on the substrate surface. In fact, this was observed in SEM images surrounding some gold nanoparticles. It may not necessarily be seen around all gold nanoparticles, because, the surface of $MgAl_2O_4$ was found to restructures under high annealing temperature, which may counteract the depressions, making them indistinguishable by SE imaging.

This method for self-assembly accounts for the temperature dependent formation of the magnesium aluminate nanostructures, and may account for their thickness dependence as well; thicker films dewet to form larger particles, therefore, they would require more energy and more heat to form the interfacial layer and initiate the self-assembly of the

$MgAl_2O_4$ nanocrystals. This is consistent with experimental results; 1 nm of gold annealed by heat treatment 3, 1060 ºC, shows a strong presence of $MgAl_2O_4$ nanocrystals beneath the gold nanoparticles. For the same heat treatment, 10 nm of gold does not show any sign of the $MgAl_2O_4$ necking structures. However, when 10 nm of gold is annealed to a higher temperature and for a longer duration by applying heat treatment 4, 1110 ºC, prominent $MgAl_2O_4$ necking structures become evident. Overall, this suggestion for the self-assembly of the $MgAl_2O_4$ necking structure has more experimental support.

3.6 Transfer of the Gold Nanoparticles to an Epoxy Carrier

Removing the gold nanoparticles that have self-assembled on the (111) $MgAl_2O_4$ substrate is useful, if it can be achieved while the particles remain intact. It allows for unambiguous 2DXRD texture analysis, since the gold particles are transferred from a lattice matched substrate to an amorphous host. Thus, the peaks apparent in every 2D texture scan correspond exclusively to gold, reducing ambiguity in determining the correct integration range required for pole figure configuration. The absence of overlapping $MgAl_2O_4$ peaks in the pole figures, also make semi-quantitative analysis more robust and transparent. For similar reasons indexing EBSD measurements also become more definite by eliminating the substrate diffraction signal which is very similar to that of gold. Removing the gold nanoparticles also provides a means of observing the footprint created at the Au/$MgAl_2O_4$ substrate interface. This shape is particularly unclear when the $MgAl_2O_4$ nanostructures are no longer evident. Other useful applications, include transfer mechanisms of the gold nanoparticles to a secondary substrate. This may be of interest, since the gold is lattice matched to the substrate; it dewets and epitaxially aligns with the substrate. The gold nanoparticles do not form alloys with the substrate material, and therefore pure gold nanoparticles can be extracted with a specific crystallographic orientation. The particles can then be transferred to a secondary substrate for further processing. In this way the $MgAl_2O_4$ substrate can be re-used for further growth of the gold nanoparticles. Re-using the substrate is particularly attractive because of its high cost. Transferring the gold nanoparticles would provide a way to both re-use the $MgAl_2O_4$ substrate, and develop gold nanoparticles with specific crystallographic orientations. Transferring particles from one substrate to another has been reported in literature and is referred to as transfer printing of solid objects [73].

Lift off was experimented with a series of materials including polystyrene, polydimethylsiloxane (PDMS), polysulfone, and epoxy (optical paste). Since epoxy yielded the most successful results, it is the focus of this section. The details for transferring the gold nanostructures from the substrate to a thin layer of epoxy are given in section 2.5. A thin film of gold, 7.5 nm, was deposited on a (111) $MgAl_2O_4$ substrate and annealed following heat treatment 3, 1060 ºC. Figure 50 illustrates the dewetted gold nanostructures. There is no distinct evidence of $MgAl_2O_4$ necking structures. For comparison, see Figure 39 (e) in section 3.2, which shows well defined necking features correlated to 1.5 nm gold films annealed following the same heat treatment, 3.

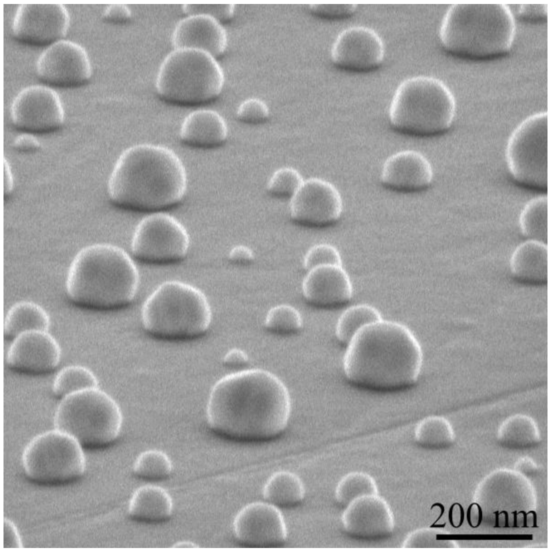

Figure 50: Secondary electron image; 7.5 nm Au deposited on (111) $MgAl_2O_4$ substrate and annealed following heat treatment 3, 1060 °C.

The gold nanoparticles were transferred from the substrate to an epoxy carrier. SE imaging, BSE imaging, and EDS were done on both the $MgAl_2O_4$ substrates, and the epoxy films, post lift off. The results indicated successful transfer of majority of the gold nanoparticles, from the substrate, to the film. In some cases nearly 100% of the particles were removed leaving behind only small footprints on the substrate. The results are shown in Figure 51. The footprints left behind on the bare substrate resembled a hexagonal structure, but this was not always clearly identifiable. These footprints appeared brighter in backscattered electron images, meaning that they have a relatively larger average atomic weight compared to the substrate. This would suggest that the footprints contain gold. However, it is still unclear if any of the topographical difference, at the footprint, corresponds to $MgAl_2O_4$ reconstruction.

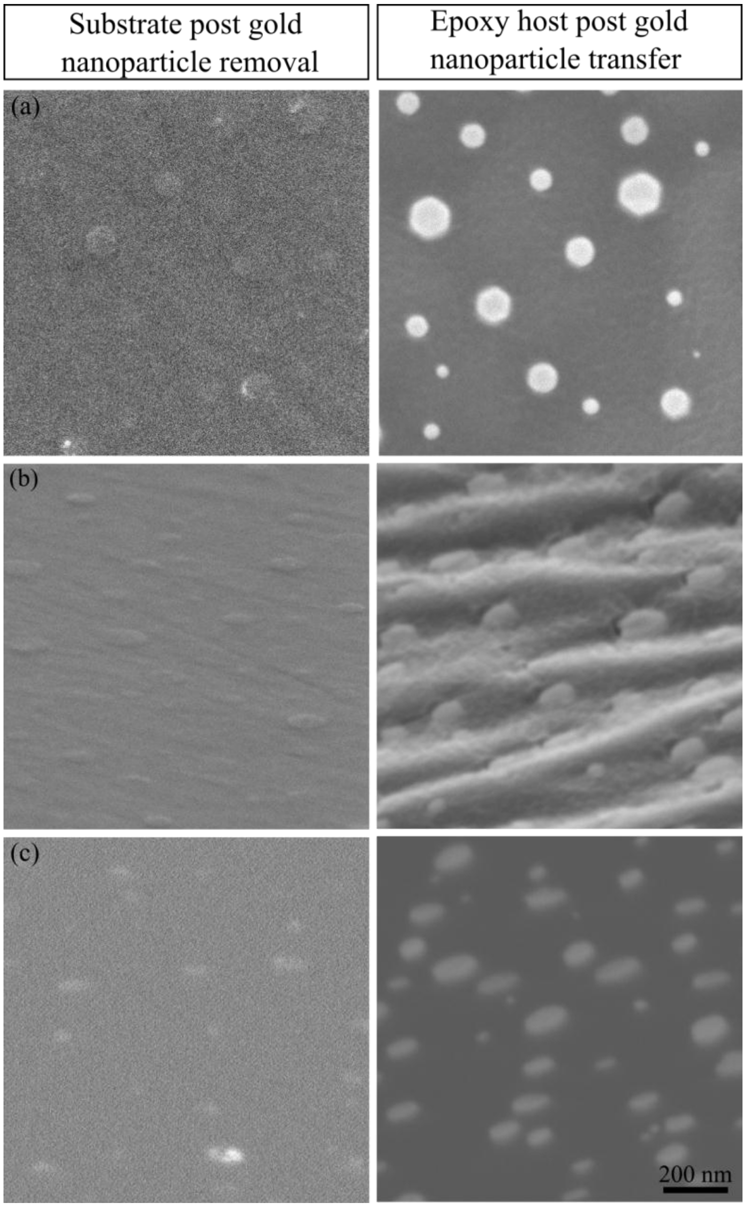

Figure 51: SEM of the substrate and epoxy film post gold nanoparticle transfer. (a) Secondary electron images of samples with 0º, and (b) 70º tilt. (c) Backscattered electron imaging at 70º tilt.

2DXRD texture analysis presented in Figure 52 of the epoxy film with embedded gold nanoparticles, exhibit the same preferred orientations as those measured from a 10 nm gold film, annealed by the same heat treatment to 1060 ºC. The only difference between their peaks is from those of the $MgAl_2O_4$ substrate, which are no longer present after transferring the particles to an epoxy film. However, the contribution from each orientation, indicated in Table 5, differs substantially and in an unexpected manner. In section 3.3, thinner films of gold showed enhanced epitaxial alignment between the gold nanoparticles and the magnesium aluminate spinel substrate. Thus, majority of the signal in thinner films arise from the crystallographic orientation of <111> Au || <111> $MgAl_2O_4$ with <10-1> Au || <10-1> $MgAl_2O_4$. However, the epoxy film having embedded gold nanoparticles, exhibited a much smaller contribution from this orientation. This may be due to an orientation-dependent Au-$MgAl_2O_4$ bond strength, where the current results suggest a stronger bond between the $MgAl_2O_4$ surface and the gold nanoparticles that are epitaxially aligned with it. Thus, most of such particles are left behind in the transfer process. In the meantime, the lifted film shows a broadening in both the rotational and radial direction, which is attributed to small misorientations created in the process of nanoparticle transfer.

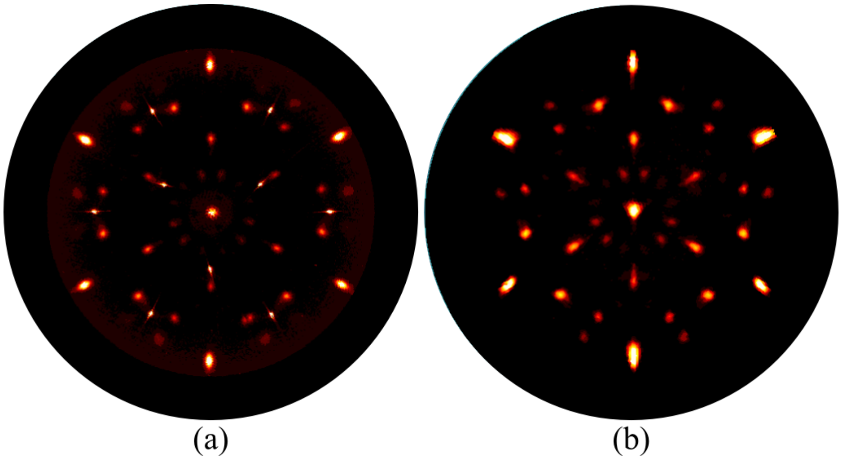

Figure 52: (111) gold pole figure; (a) Au nanoparticles on a $MgAl_2O_4$ substrate, (b) Au nanoparticles transferred to, and embedded in an epoxy film. The gold nanoparticles in (a) and (b) correspond to 10 nm Au, and 7.5 nm films of gold deposited on $MgAl_2O_4$ substrates and annealed by heat treatment 3, accordingly.

Table 5: Semiquantitative analysis of (111) pole figures of gold nanoparticles dewetted following heat treatment 3, prior to and post transfer of the gold nanoparticles to an epoxy host.

Orientation	Prior to liftoff	Post lift off
<111> Au ‖ <111> $MgAl_2O_4$ with <10-1> Au ‖ <10-1> $MgAl_2O_4$: 0º in-plane rotation	47 %	8 %
<111> Au ‖ <111> $MgAl_2O_4$ for 60º in-plane rotation	21 %	16 %
<511> Au ‖ <111> $MgAl_2O_4$ for all in-plane rotations	18 %	41 %
Other	14 %	35 %

In summary, the gold nanoparticles were transferred from the $MgAl_2O_4$ substrate to an epoxy carrier. 2DXRD textures analysis showed the transferred gold nanoparticles maintained their orientations, however, some broadening in both the radial and rotational direction was present. Semi-qualitative analysis of the pole figure's peak intensities suggested that the gold nanoparticles that are epitaxially aligned with the substrate are left behind during the transfer process, which may be because of higher bond strengths. Backscattered electron imaging indicated compositional contrast at the footprints, suggesting the presence of gold, however, it is not clear if there was any contribution from $MgAl_2O_4$ surface reconstructions at the footprint.

Chapter 4 - Conclusions

Solid-state dewetting characteristics of thin gold films on (111) $MgAl_2O_4$ substrates were investigated, where the presence of gold promotes the self-assembly of crystalline $MgAl_2O_4$ nanostructures. These structures were first discovered by Devenyi et al., but their composition had been entirely attributed to gold [1]. In this work, STEM revealed that the intricately shaped structures self-assembled on the $MgAl_2O_4$ substrate are composed of three distinct components: an Au faceted sphere, separated from a $MgAl_2O_4$ truncated triangular or hexagonal pyramid, by an Au-O interfacial layer. EELS maps suggest a chemically sharp boundary across the Au-$MgAl_2O_4$ interface. EBS measurements done below the interfacial boundary detected the presence of only magnesium, aluminum and oxygen elements. As well, HAADF imaging showed that the structure formed below the interfacial layer has the same lattice constant and compositional contrast as the $MgAl_2O_4$ substrate. The composition of the boundary layer was determined by G. Zhu's simulations, which were based on HAADF, MAADF, and LAADF imaging contrast, at the interfacial layer [74]. Both EELS and EDS confirmed that the faceted sphere, above the interfacial boundary, was composed of gold.

Thin films of gold sputtered onto $MgAl_2O_4$ substrates, underwent solid state diffusion, when heated sufficiently, and deweted to form nanoparticles. For a given thickness, increasing the temperature improved the crystallinity of the gold nanoparticles. A 10 nm film of gold developed a preferred orientation of <111> Au || <111> $MgAl_2O_4$ when annealed to 640 ºC. However, it exhibited random in-plane orientation, with large radial broadening. For the same thickness, heating to 940 ºC, reduced the radial broadening, while the texture remained the same. The elevated temperature may have had enhanced the mobility of the gold nanoparticles, allowing them to rearrange to more uniform low energy crystallographic orientations. When the gold nanoparticles were heated to 1060 ºC, or 1110 ºC, and cooled following the two stage annealing profiles described in this work, in-plane texture was developed, having further reduced radial broadening, and was dominated by the epitaxial alignment of the gold nanoparticles with the $MgAl_2O_4$ substrate.

The in-plane texture development of the gold nanoparticles was not only temperature dependent, but also thickness dependent. When a 1.5 nm gold film on a (111) $MgAl_2O_4$ substrate was annealed to 940 ºC, it exhibited a high level of texture, unlike the 10 nm gold film. The comparatively small size of the gold nanoparticles developed by annealing a thinner thickness of gold, 1.5 nm, may describe this phenomenon. These particles had an average diameter of 14 nm, and a standard deviation of 5 nm. Therefore, their melting point lies in the vicinity of the maximum temperature that they were heated to. For this reason, many of the particles were likely in the molten phase, and therefore had higher mobility to organize to lower energy crystallographic structures and shapes. The SE imaging showed that these small particles had attained the shape of a hemispherical cap, while the nanoparticles that self-assembled from a 10 nm film of gold were composed mostly of large-area flat surfaces, much further from their equilibrium structure.

Similar to the gold nanoparticles, the self-assembly of the $MgAl_2O_4$ nanostructures was also found to be sensitive to both the annealing profile and the thickness of the gold film sputtered on the substrate. The $MgAl_2O_4$ nanostructures were only distinctly observed by applying the two stage annealing profiles, having a maximum temperature of 1060 ºC or 1110 ºC; with the higher temperature correlated to more $MgAl_2O_4$ mass transport, leading to bigger $MgAl_2O_4$ nanostructures. By annealing the films to 1310 ºC, with faster annealing rates and for longer durations, the gold nanoparticles diminished in size. The increased temperature enhanced the saturated pressure of gold, which may have stimulated the evaporation of the gold nanoparticles. As the gold nanoparticles evaporated, their radius decreased, and therefore their vapor pressure heightened, which may have further promoted evaporation.

For a given heat treatment, the thickness of the gold overlayer played an important role in the visible presence of the $MgAl_2O_4$ nanostructures. Applying heat treatment 3, 1060 ºC, the $MgAl_2O_4$ nanostructures which are evident for thinner films of gold, are no longer apparent for a 6 nm gold film. Using heat treatment 4, 1110 ºC, which involves longer annealing durations, the $MgAl_2O_4$ necking structures were prominently visible for 10 nm gold films, but become very scarce for 50 nm gold films. This pattern shows that the upper limit in thickness that corresponds to the formation of intricate Au-$MgAl_2O_4$ nanostructures shifts to larger values as annealing temperature and duration increases.

It is not clear if the $MgAl_2O_4$ nanostructures preferentially self-assemble under gold nanoparticles having a specific crystallographic orientation. Using an adhesive and liquid nitrogen, the gold nanoparticles were rapidly cooled, to induce thermal stress, and detach from the substrate. Two dimensional XRD on the detached gold particles showed that gold nanoparticles having a <111> orientation were preferentially left behind on the substrate. This may indicate a stronger bond with the substrate and a potentially favorable nucleation site for $MgAl_2O_4$ to diffuse to, at high temperatures.

Performing comparative experiments, with and without a gold overlayer, showed that the presence of a gold film on the $MgAl_2O_4$ substrate prior to annealing, promotes the self-assembly of the $MgAl_2O_4$ nanostructures. However the method in which the self-assembly occurs is not entirely clear. Gold may be acting as a catalyst by reducing the activation energy for the self-assembly of the $MgAl_2O_4$ nanoparticles. Alternatively, the Au-$MgAl_2O_4$ interface may evolve through the annealing process to form an interfacial boundary that acts as a nucleation site, and promotes solid state diffusion of the $MgAl_2O_4$ surface to the region beneath the interfacial boundary layer. There is not sufficient evidence to fully support either suggested method.

The self-assembly of the $MgAl_2O_4$ nanostructures on a (111) $MgAl_2O_4$ substrate, stimulated by the presence of gold at high temperatures, has not been reported to date. It introduces a new and relatively straightforward method for the growth of crystalline nanostructures. Understanding the phenomenon involved in the growth process may have significant implications, creating new applications for this material system, which may be further extended to other materials as well.

Chapter 5 - Suggestions for Future Work

Investigating the self-assembly of nanostructures created by other substrate surfaces may enhance the applicability of the findings presented in this work. Experimental methods similar to those presented in this thesis may be applied to alternative oxide substrates with high melting temperatures, to investigate the possible self-assembly of nanostructures from their surfaces, similar to the self-assembly $MgAl_2O_4$ nanostructures reported here.

This chapter describes further experiments that can be done to extend both the understanding and potential applicability of the unique self-assembly reported in this work. These experiments can also be done on other material systems in which this phenomenon may be extendable to.

5.1 In-situ X-ray Diffraction Texture Analysis

The McMaster Analytical X-Ray Diffraction facility is equipped with a system that uses a cobalt Bruker D8 Davinci, Vantec 500 area detector, and is accessorised with a high and low temperature stage ranging from -183 ºC to 800 ºC. The heating process can be done within a dome so that the pressure and type of gas, throughout the heating process, can be controlled. This provides an invaluable opportunity to perform in-situ X-ray diffraction experiments.

Preliminary in-situ texture measurements were done using this system in effort to correlate the relation between dewetting phenomenon and crystallographic restructuring of the gold film/substrate surface. This was the first time such an experiment had been done using this system at McMaster University. The results remained ambiguous and inconclusive as phase analysis suggested the presence of materials other than Au and $MgAl_2O_4$ in the measured system. The new phase was not found to be correlated to the sample stage, dome, or the clips, which were mandated for holding the sample in place during data collection. The unidentified phase could be attributed to contamination on the sample holder, or the clips. Further experiments can be done to improve this experiment, and obtain qualitative or semi-quantitative results related to crystallographic organization of the gold nanoparticles with temperature and time. This can be done by running a texture scan while the sample is being heated, causing the pole figure to evolve as a function of temperature. Tuning the heating rate, the dwell time at each X-ray frame, and the thickness of the gold film, one may observe different levels of crystallographic order within a single pole figure. i.e. The pole figure may contain an arc indicating a (111) preferred orientation with random in-plane texture which slowly evolves to a distinct sharp peak within the same polefigure.

Despite the limited range of temperatures available in this system, the system can still be used in application to this work. The dewetting of gold films is thickness dependant, and occurs at relatively low temperatures. Based on the current experimental results, it is understood that when the gold film dewets and forms nanoparticles, it develops texture. For a given film thickness, in-situ X-ray experiments would assist in determining the temperature at which the film dewets, by the sudden change in texture of gold. Once this temperature is determined, SE imaging can be done to determine the size of the particles corresponding to the temperature at which the texture of gold had changed. It is anticipated that the particles will be near their smallest size at this point, and further heat treatments would induce Ostwald ripening or particle agglomeration. Therefore, using in-situ X-ray, the potential correlation between the size of the nanoparticles, when they are smallest at earlier stages of dewetting, to the observation of $MgAl_2O_4$ self-assemblies that are formed by further heat treatments, can be investigated. This would develop an understanding of whether the $MgAl_2O_4$ self-assembly is solely explained by occurrences at high temperatures and in the cool down stage, or if it is also dependent on phenomenon at lower temperatures, related to the size dependent catalytic activity of gold.

5.2 EBSD Measurements on Individual Gold Nanoparticles

Indexing EBSD measurements obtained from gold nanoparticles self-assembled on $MgAl_2O_4$ substrates is not trivial. The minimal lattice mismatch between the two materials makes distinguishing between them challenging. EBSD measurements were experimented on the gold nanoparticles transferred to an epoxy carrier. The results allowed for distinction between the gold nanoparticles and the epoxy carrier, however, the deformation of the epoxy under the high energy of the applied beam, introduced ambiguity in the orientations. As well, when the gold nanoparticles are embedded in the epoxy no correlation can be made between the three dimensional shape of the gold nanoparticle, and the identified crystallographic orientation. If measurements were done on gold nanoparticles supported on the $MgAl_2O_4$ substrate, then such correlation may be made. One important experiment that could be conducted is to use EBSD to find a correlation, if there exists any, between the crystallographic orientation of the gold nanoparticles and the height of the $MgAl_2O_4$ necking structure. Samples prepared using the same thickness, but different temperatures, can also be analysed to understand how the structure of a gold nanoparticle that corresponds to a specific crystallographic orientation evolves by increasing temperature.

5.3 Investigating the Au-$MgAl_2O_4$ Interfacial Layer

The current study suggested the presence of a distinct interfacial layer at the boundary of the of the Au-$MgAl_2O_4$ intricate nanostructures. This boundary may be key to the self-assembly of the $MgAl_2O_4$ nanostructures.

It is suggested that the nature of the boundary of the Au-$MgAl_2O_4$ intricate nanostructures to be further investigated. To do this aqua regia or mercury can be used to dissolve gold, leaving behind the $MgAl_2O_4$ necking structure and potentially, the interfacial boundary layer. The specimens can then be studied in the SEM using secondary electron, and backscattered electron imaging. Subsequently, TEM specimens can be prepared using the FIB, such that the necking structures are selected as the region of interest. TEM may indicate if dissolving the gold affected the interfacial layer. If it had not, then it will also provide more insight on the elements present within this layer. It is suggested to do this experiment with a 10 nm thick gold film, annealed following heat treatment 4, as described in this work. This combination of film thickness and annealing profile has shown to form the most prevalent self-assembly of the $MgAl_2O_4$ nanostructures.

5.4 Patterning the $MgAl_2O_4$ Nanostructures

$MgAl_2O_4$ substrates supporting intricate Au-$MgAl_2O_4$ nanostructures may be re-used for templated growth of gold nanoparticles, growth of nanowires, and/or possibly to control the density of the $MgAl_2O_4$ necking structures. Studies can be done to template the growth of the intricate Au-$MgAl_2O_4$ structures using e-beam lithography. Once templated structures are formed aqua-regia or mercury can be used to dissolve the gold nanoparticles. Then a new layer of gold can be deposited on the surface and annealed. It is not clear if the newly dewetted particles will nucleate on the $MgAl_2O_4$ necking structures, in-between them, or both. This may depend on the nature of the interfacial layer post Au removal. If the newly deposited film of gold nucleates at the top of the necking structures, then, the substrate may be patterned once, and can be reused several times for the templated growth of gold nanoparticles. The gold nanoparticles can be removed by various transfer mechanisms and used for other potential applications. In a similar manner, templated nanowires may be grown on the surface.

Alternatively, if gold prefers to nucleate in-between pre-existing $MgAl_2O_4$ nanostructures, then when annealed again, it will increase the density of these nanostructures. If this process is repeated several times, the surface of the substrate will be patterned with a high density of $MgAl_2O_4$ necking structures[k] so that inverted pyramids are created between them. In this case, the substrate can be used for templated growth of nanowires. GaN nanowires may be best suited for this purpose, as studies have reported that chemically etched and passivated surfaces of $MgAl_2O_4$, provide the most suitable substrate for depositing high quality GaN films [75], [76].

---

[k] As suggested by Dr. Kristoffer Meinander

References

[1] G. A. Devenyi, J. Li, R. A. Hughes, A. C. Shi, P. Mascher and J. S. Preston, "Epitaxially driven formation of intricate supported gold nanostructures on a lattice-matched oxide substrate," *Nano Letters,* vol. 9, no. 12, pp. 4258-4263, 2009.

[2] L. Armelao, D. Barreca, G. Bottaro, G. Alberto, S. Gross, C. Maragno and E. Tondello, "Recent trends on nanocomposites based on Cu, Ag and Au clusters: A closer look," *Coordination Chemistry Reviews,* vol. 250, no. 11-12, pp. 1294-1314, 2006.

[3] C. Louis and O. Pluchery, Gold Nanoparticles for Physics, Chemistry and Biology, London: Imperial College Press, 2012.

[4] V. Jarvis, J. F. Britten and R. R. LaPierre, "Texture analysis of GaAs nanowires," *Semiconductor Science and Technology,* vol. 26, no. 2, p. 025014, 2011.

[5] D. Takagi, Y. Homma, H. Hibino, S. Suzuki and Y. Kobayashi, "Single-walled carbon nanotube growth from highly activated metal nanoparticles," *Nano Letters,* vol. 6, no. 12, pp. 2642-2645, 2006.

[6] R. S. Wagner, W. C. Ellis, K. A. Jackson and S. M. Arnold, "Study of the filamentary growth of silicon crystals from the vapor," *Journal of Applied Physics,* vol. 35, no. 10, pp. 2993-3000, 1964.

[7] G. Cao and Y. Wang, Nanostructures and nanomaterials: synthesis, properties, and applications, 2nd ed., Toh Tuck Link: World Scientific Publishing Co. Pte. Ltd., 2004.

[8] M. Haruta, "Catalysis of gold nanoparticles deposited on metal oxides," *CATTECH ,* vol. 6, no. 3, pp. 102-115, 2002.

[9] R. Sardar, A. M. Funston, P. Mulvaney and R. W. Murray, "Gold nanoparticles: past, present, and future," *Langmuir,* vol. 25, no. 24, pp. 13840-13851, 2009.

[10] P.-G. de Gennes, F. Brochard-Wyart and D. Quere, Capillarity and wetting phenomena: drops, bubbles, pearls, waves, New York: Springer-Verlag New York, Inc., 2004.

[11] K. Jacobs, R. Seemann and S. Herminghaus, "Stability and dewetting of thin liquid films," *arXiv:0805.4336 [soft condensed matter],* 2008.

[12] R. Seemann, S. Herminghaus and K. Jacobs, "Dewetting patterns and molecular forces: a reconciliation," *Physical Review Letters,* vol. 86, no. 24, pp. 5534-5537,

2001.

[13] C. V. Thompson, "Solid-state dewetting of thin films," *Annual Review of Materials Research,* vol. 42, pp. 399-434, 2012.

[14] J. Bischof, D. Scherer, S. Herminghaus and P. Leiderer, "Dewetting modes of thin metallic films: nucleation of holes and spinodal dewetting," *Physical Review Letters,* vol. 77, no. 8, pp. 1536-1539, 1996.

[15] A. Michaelides and M. Scheffler, "An introduction to the theory of metal surfaces," in *Textbook of Surface and Interface Science, Vol. I+II*, Weinheim, Wiley-VCH, 2010.

[16] P. R. Gadkari, A. P. Warren, R. M. Todi, R. V. Petrova and K. Coffey, "Comparison of the agglomeration behavior of thin metallic films on SiO2," *Journal of Vacuum Science & Technology A,* vol. 23, no. 4, pp. 1152-1161, 2005.

[17] Y. Kojima and T. Kato, " Nanoparticle formation in Au thin films by electron-beam-induced dewetting," *Nanotechnology,* vol. 19, p. 255605, 2008.

[18] C. M. Müller, F. C. F. Mornaghini and R. Spolenak, "Ordered arrays of faceted gold nanoparticles obtained by dewetting and nanosphere lithography," *Nanotechnology,* vol. 19, no. 48, p. 485306, 2008.

[19] G. Meng, T. Yanagida, M. Kanai, M. Suzuki, K. Nagashima, B. Xu, F. Zhuge, A. Klamchuen, Y. He, S. Rahong, S. Kai and T. Kawai, "Pressure-induced evaporation dynamics of gold nanoparticles on oxide substrate," *Physical Review E,* vol. 87, no. 1, pp. 012405-012411, 2013.

[20] S. Vasisht and J. Shirokoff, "Preferred orientations in nano-gold/silica/silicon interfaces," *Applied Surface Science,* vol. 256, no. 15, pp. 4915-4923, 2010.

[21] H. E. Swanson and E. Tatge, "Standard X-ray diffraction powder patterns," *National Bureau of Standards (US), Circular,* vol. 539, no. 1, pp. 1-95, 1953.

[22] I. Galanakis, N. Papanikolaou and P. H. Dederichs, "Applicability of the broken-bond rule to the surface energy of the fcc metals," *Surface Science,* vol. 511, no. 1-3, pp. 1-12, 2002.

[23] H. Lange, "Roentgenspektroskopische Untersuchungen einiger Metallegierungen nach Seemann-Bohlin," *Annalen der Physik (Leipzig),* vol. 4, no. 76, pp. 455-475, 1925.

[24] P. Buffat and J.-P. Borel, "Size effect on the melting temperature of gold particles," *Physical Review A,* vol. 13, no. 6, pp. 2287-2298, 1976.

[25] F. Geiger, C. A. Busse and R. I. Loehrke, "The vapor pressure of indium, silver, gallium, copper, tin, and gold between 0.1 and 3.0 bar," *International Journal of Thermophysics,* vol. 8, no. 4, pp. 425-436, 1987.

[26] D. J. Gorin and F. D. Toste, "Relativistic effects in homogeneous gold catalysis," *Nature,* vol. 446, pp. 395-403, 2007.

[27] D. Thompson, "New advances in gold catalysis part I," *Gold Bulletin,* vol. 31, no. 4, pp. 111-118, 1998.

[28] A. Stephen, K. Hashmi, J. Graham and Hutchings, "Gold catalysis," *Angewandte Chemie International Edition,* vol. 45, no. 47, pp. 7896-7936, 2006.

[29] D. Y. Cha and G. Parravano, "Surface reactivity of supported gold: I. Oxygen transfer between CO and CO2," *Journal of Catalysis,* vol. 18, no. 2, pp. 200-211, 1970.

[30] S. Galvagno and G. Parravano, "Chemical reactivity of supported gold: IV. Reduction of NO by H2," *Journal of Catalysis,* vol. 55, no. 2, pp. 178-190, 1978.

[31] M. Haruta, "Gold as a novel catalyst in the 21st century: Preparation, working mechanism and applications," *Gold Bulletin,* vol. 37, no. 1-2, pp. 27-36, 2004.

[32] . M. Okumura, S. Nakamura, S. Tsubota, T. Nakamura, M. Azuma and M. Haruta, "Chemical vapor deposition of gold on Al2O3, SiO2, and TiO2 for the oxidation of CO and of H2," *Catalysis Letters,* vol. 51, no. 1-2, pp. 53-58, 1998.

[33] J. Guo, H. Lou, H. Zhao, D. Chai and X. Zheng, "Dry reforming of methane over nickel catalysts supported on magnesium aluminate spinels," *Applied Catalysis A: General,* vol. 273, no. 1-2, pp. 75-82, 2004.

[34] K. A. Dick, "A review of nanowire growth promoted by alloys and non-alloying elements with emphasis on Au-assisted III-V nanowires," *Progress in Crystal Growth and Characterization of Materials,* vol. 54, no. 3-4, pp. 138-173, 2008.

[35] M. J. Davies, S. C. Parker and G. W. Watson, "Atomistic simulation of the surface structure of spinel," *Journal of Materials Chemistry,* vol. 4, no. 6, pp. 813-816, 1995.

[36] W. H. Bragg, "The structure of magnetite and the spinels," *Nature,* vol. 95, pp. 561-561, 1915.

[37] C. Păcurariua, I. Lazăua, Z. Ecsedi, R. Lazăua, P. Barvinschi and G. Mărginean, "New synthesis methods of MgAl2O4 spinel," *Journal of the European Ceramic Society,* vol. 27, no. 2-3, pp. 707-710, 2007.

[38] C. M. Fang, S. C. Parker and G. de With, "Atomistic simulation of the surface energy of spinel MgAl2O4," *Journal of the American Ceramic Society,* vol. 83, no. 8, pp. 2082-2084, 2004.

[39] M. K. Rasmussen, K. Meinander, F. Besenbacher and J. V. Lauritsen, "Noncontact atomic force microscopy study of the spinel MgAl2O4(111) surface," *Beilstein Journal of Nanotechnology,* vol. 3, pp. 192-197, 2012.

[40] M. Yoshimoto, T. Maeda, T. Ohnishi, H. Koinuma, O. Ishiyama, M. Shinohara, M. Kubo, R. Miura and A. Miyamoto, "Atomic-scale formation of ultrasmooth surfaces

on sapphire substrates for high-quality thin-film fabrication," *Applied Physics Letters,* vol. 67, no. 18, pp. 2615-2617, 1995.

[41] Y. Yu, "Diffusion reactions at metal-oxide interfaces and the effect of an applied electric field," Case Western Reserve University, Cleveland, 2005.

[42] D. Kim, A. L. Giermann and C. V. Thompson, "Solid-state dewetting of patterned thin films," *Applied Physics Letters,* vol. 95, no. 25, pp. 251903-251905, 2009.

[43] P. Farzinpour, A. Sundar, K. D. Gilroy, Z. E. Eskin, R. A. Hughes and S. Neretina, "Altering the dewetting characteristics of ultrathin gold and silver films using a sacrificial antimony layer," *Nanotechnology,* vol. 23, no. 49, p. 495604, 2012.

[44] F. Y. Lee, K. H. Fung, T. L. Tang, W. Y. Tam and C. T. Chan, "Fabrication of gold nano-particle arrays using two-dimensional templates from holographic lithography," *Current Applied Physics,* vol. 9, no. 4, pp. 820-825, 2009.

[45] A. Sundar, C. J. Decker, R. A. Hughes and S. Neretina, "The templated assembly of highly faceted three-dimensional gold microstructures into periodic arrays," *Materials Letters,* vol. 76, pp. 155-158, 2012.

[46] A. Sundar, R. A. Hughes, P. Farzinpour, K. D. Gilroy, G. A. Devenyi, J. S. Preston and S. Neretina, "Manipulating the size distribution of supported gold nanostructures," *Applied Physics Letters,* vol. 100, no. 1, pp. 013111-013114, 2012.

[47] P. Farzinpour, A. Sundar, K. D. Gilroy, Z. E. Eskin, R. A. Hughes and S. Neretina, "Dynamic templating: a large area processing route for the assembly of periodic arrays of sub-micrometer and nanoscale structures," *Nanoscale,* no. 5, pp. 1929-1938, 2013.

[48] C. Favazza, J. Trice, R. Kalyanaraman and R. Sureshkumar, "Self-organized metal nanostructures through laser-interference driven thermocapillary convection," *Applied Physics Letters,* vol. 91, no. 4, pp. 043105-043107, 2007.

[49] H. Krishna, R. Sachan, J. Strader, C. Favazza, M. Khenner and R. Kalyanaraman, "Thickness-dependent spontaneous dewetting morphology of ultrathin Ag films," *Nanotechnology,* vol. 21, no. 15, p. 155601, 2010.

[50] J. Trice, C. Favazza, D. Thomas, H. Garcia, R. Kalyanaraman and R. Sureshkumar, "Novel Self-Organization mechanism in ultrathin liquid films: theory and experiment," *Physical Review Letters,* vol. 101, no. 1, pp. 017802-017805, 2008.

[51] C.-Y. Hsu, J.-W. Huang, S. Gwo and K.-J. Lin, "The facile fabrication of tunable plasmonic gold nanostructure arrays using microwave plasma," *Nanotechnology,* vol. 21, no. 3, p. 035302, 2010.

[52] L. Billot, M. L. de la Chapelle, A. -S. Grimault, A. Vial, D. Barchiesi, J. -L. Bijeon, P. -M. Adam and P. Royer, "Surface enhanced Raman scattering on gold nanowire arrays: Evidence of strong multipolar surface plasmon resonance enhancement,"

Chemical Physics Lettera, vol. 422, no. 4-6, pp. 303-307, 2006.

[53] V. M. Shalaev, W. Cai, U. K. Chettiar, H.-J. Yuan, A. K. Sarychev, V. P. Drachev and A. V. Kildishev, "Negative index of refraction in optical metamaterials," *Optics Letters,* vol. 30, no. 24, pp. 3356-3358, 2005.

[54] Q. Li and G. T. Wang, "Spatial distribution of defect luminescence in GaN nanowires," *Nano Letters,* vol. 10, no. 5, pp. 1554-1558, 2010.

[55] M. Cantoro, S. Hofmann, S. Pisana, V. Scardaci, A. Parvez, C. Ducati, A. C. Ferrari, A. M. Blackburn, K.-Y. Wang and J. Robertson, "Catalytic chemical vapor deposition of single-wall carbon nanotubes at low temperatures," *Nano Letters,* vol. 6, no. 6, pp. 1107-1112, 2006.

[56] "Gatan, Inc. Specimen Preparation Model 682 PECS + RIBE System," Gatan, Inc., 2007. [Online]. Available: http://www.gatan.com/specimenprep/682_pecs.php. [Accessed August 2013].

[57] J. Goldstein, D. Newbury, D. Joy, C. Lyman, P. Echlin, E. Lifshin, L. Sawyer and J. M. Kluwer, Scanning electron microscopy and x-ray microanalysis, 3rd edition, New York: Academic Publishers, 2003.

[58] Tesker Corperation, "SEM scanning electron microscope A To Z: basic knowledge for using the SEM," [Online]. Available: http://www.teksercorp.com/docs/jeol/sem/SEM_A_To_Z_light.pdf. [Accessed August 2013].

[59] H. Seiler, "Secondary electron emission in the scanning electron microscope," *Journal of Applied Physics,* vol. 54, no. 11, p. R1, 1983.

[60] L. Corbari, M. -A. Cambon-Bonavita, G. J. Long, F. Grandjean, M. Zbinden and P. Compère, "Iron oxide deposits associated with the ectosymbiotic bacteria in the hydrothermal vent shrimp Rimicaris exoculata," *Biogeosciences,* no. 5, pp. 1295-1310, 2008.

[61] Muso, Artist, *Principle of EDX.* [Art]. 2007.

[62] Z. Guo-Zhen, "High-resolution characterization of low-dimensional defects in SrTiO3," McMaster University, Hamitlon, 2012.

[63] N. W. Ashcroft and N. D. Mermin, Solid state physics, Philadelphia: Holt Rinehard & Winston, 1976.

[64] S. A. Speakman, "Basics of X-ray powder diffraction: training to cecome an independent user," Massachuesetts Institute of Technology, Boston.

[65] B. B. He, Two-dimensional X-ray diffraction, Hoboken: John Wiley & Sons, Inc., 2009.

[66] Hydrargyrum, Artist, *Bragg diffraction from a cubic crystal lattice.* [Art]. 2011.

[67] Wiso, Artist, *Costruzione della sfera di Edwald.* [Art]. 2009.

[68] Veeco Instruments Inc., "SPMT training notebook," Veeco Instruments Inc., Plainview, 2003.

[69] P. Eaton and P. West, Atomic Force Microscopy, New York: Oxford University Press Inc., 2010.

[70] J. Preston, S. Jovanovic and G. Devenyi, "Arbitrarily thing ultra smooth film with bulit-in seperation ability and method of forming the same". International Patent Cooperation Union Patent 61/683,317, 15 August 2012.

[71] G. Zhu, *Private Communication from Dr. Guozhen Zhu: Department of Materials Science and Engineering, McMaster University,* Hamilton, 2013.

[72] D. P. Wheeler, "Precision measurements of the lattice constants of twelve common metals," *Physical Review,* vol. 25, no. 6, pp. 753-761, 1925.

[73] M. A. Meitl, Z.-T. Zhu, V. Humar, K. J. Lee, X. Feng, Y. Y. Huang, I. Adesida, R. G. Nuzzo and J. A. Rogers, "Transfer printing by kinetic control of adhesion to an elastomeric stamp," *Nature Materials,* vol. 5, pp. 33-38, 2006.

[74] G. Zhu, "Private Communication from Dr. Guozhen Zhu: Department of Materials Science and Engineering, McMaster University," Hamilton, 2013.

[75] G. He, S. F. Chichibu and T. Chikyow, "Microstructure and interface control of GaN/MgAl2O4 grown by metalorganic chemical vapor deposition: Substrate-orientation dependence," *Journal of Applied Physics,* vol. 110, no. 2, pp. 023504-023511, 2011.

[76] G. He, T. Chikyow and S. F. Chichibu, "Interface chemistry and electronic structure of GaN/MgAl2O4 revealed by angle-resolved photoemission spectroscopy," *Applied Physics Letters,* vol. 97, no. 16, pp. 161907-161909, 2010.

[77] S. M. Jovanovic, "Pulsed laser heteroepitaxy of high quality CdTe thin films on sapphire substrates," McMaster University, Hamilton, 2013.

[78] D. B. Williams and C. B. Carter, Transmission electron microscopy: a textbook for materials science, 2nd ed., New York: Springer Science+Business Media, LLC, 2009.

Appendices

Appendix A- Substrate Cleaning Procedure

The cleaning procedure employed was adapted from the “Substrate Degreasing Standard Operating Procedure” described by S. M. Jovanovic in reference [77]. The most important difference between the two methods is in the use of lens paper, and the specific method of applying it, instead of the foam tips. This use of lens tissue was found to be effective in re-producing samples with less contamination visible through the optical microscope. These modifications may not have been necessary if all steps of the recommended procedure from reference [77] were followed; many were removed since it was unclear how those processing steps would affect the substrate surface, and thus the experimental results. Further research can be done, to improve upon the suggested cleaning method described here.

This cleaning procedure involves the use of tweezers, a beaker, lens paper, acetone, methanol, isopropanol, waste disposal containers, scissors, Parafilm, a sonicator, and a purchased custom Teflon made sample holder that is used in the sonication process. This sample holder can hold seven samples and fits inside a 500 mL beaker. Perforations in the holder bottom allow for solvent draining.

1. Rinse the tweezers, sonication basket, and the inside of the beaker that will be used for handling the samples, with isopropanol, methanol and acetone in this order. While avoiding cross contamination, use a lens paper dampened with isopropanol to whip all the surfaces. Make sure to wipe in only one direction and after using the lens tissue to wipe once and one direction, dispose of it and use a fresh one to continue cleaning. This will reduce cross contamination from one part of a surface to another. Rinse all surfaces again with isopropanol, methanol and acetone.

2. If two-side polished samples are being used, use a scribe to create an asymmetric marker on the back side of the surface. If the sample will be used for Ultraviolet-visible spectroscopy, then care should be taken, that this marker does not cover the region of the sample that will be exposed during measurements. Make note of the symbol and location that is created. This symbol should help you distinguish the front surface from the back.

3. Using tweezers lift the sample and rinse both sides with isopropanol.

4. Lay two clean sheets of lens paper on the workbench. Use clean gloves and scissors to cut several sheets of lens paper to smaller sizes. Avoid cross contamination, of any type, to the lens paper.

5. Place the sample on a clean lens paper with its back side facing the upward direction. Use tweezers to firmly grip two adjacent corners of the substrate. Lift a small piece of lens tissue so that the surface which will be in contact with the substrate remains untouched and free from cross contamination. Use the small piece of lens paper to wipe the sample surface in one direction, then dispose of it. Move the sample to a new spot on the lens tissue, such as right beside it. Rotate the sample 90^{o} and repeat the cleaning process. Continue this process until the back side goes through eight rotations. Flip the sample over. Repeat this process for the front side until 12 rotations are completed.

6. Place the sample in the sonication sample holder and place the holder in the cleaned beaker. If you are cleaning more than one sample then cover the beaker with Parafilm until the next sample is ready to be added to the sample holder.

7. After all samples are cleaned, thoroughly rinse the sonication basket, which now contains all the samples. Solvent rinsing should be in the order isopropanol, methanol and acetone, and then repeat in the reverse order.

8. Fill the beaker with isopropanol. Carefully place the sonication substrate holder in the beaker. The solvent level should be about 0.5 cm to 1 cm above the tallest substrate in the holder.

9. Place the beaker in the sonicator. Cover the beaker with Parafilm so that the top of the beaker is covered, but a seal is not created. The solvent vapors should leave the beaker and not condense on the Parafilm and drip back inside. The role of the Parafilm is to reduce the number of particles that may enter the beaker during the sonication process. Set the sonicator for 40 minutes.

10. Remove the Parafilm, rinse the inside of the beaker and sample holder with isopropanol, then with methanol. Repeat step 9 substituting isopropanol with methanol.

11. Repeat step 10, this time with acetone instead of methanol. As well, set sonication time for 90 minutes instead of 40.

12. After 75 minutes remove the Parafilm and remove the samples one by one from the holder, while the sonicator continues to run. The method of removal is quite important in this step. Try to grip the sample by either two corners or by clamping it with the tweezer at one corner, covering as litter surface area, as possible. Try to avoid prematurely releasing the sample back into the beaker during the extraction process. Slowly remove the sample, so that the solvent evaporates at the same rate as the sample is leaving the solvent.

13. Place the samples in a clean sample holder.

14. Use an optical microscope at 5 X, or 10 X magnification to inspect the cleanliness of the samples. To prevent cross contamination between the microscope glass slide and the cleaned sample, place a small piece of flat lens tissue on the glass slide. Then place the sample over the lens paper. If the sample appears dirty across the entire surface, re-clean the sample. If the contamination is localized, make note of the contamination, and its location. Avoid probing these locations in various characterization techniques.